Master's thesis

NTNU
Norwegian University of Science and Technology
Faculty of Information Technology and Electrical Engineering
Department of Electronic Systems

Håvard Katle Fjon

Magnetic Ordering in Artificial Spin Ice: Towards Tailormade Magnetic Metamaterials

Master's thesis in Nanotechnology
Supervisor: Erik Folven
Co-supervisor: Anders Strømberg
June 2021

NTNU
Norwegian University of Science and Technology

Håvard Katle Fjon

Magnetic Ordering in Artificial Spin Ice: Towards Tailormade Magnetic Metamaterials

Master's thesis in Nanotechnology
Supervisor: Erik Folven
Co-supervisor: Anders Strømberg
June 2021

Norwegian University of Science and Technology
Faculty of Information Technology and Electrical Engineering
Department of Electronic Systems

NTNU
Norwegian University of
Science and Technology

Abstract

As CMOS technology reaches the limit of Moore's law, more attention is directed towards possible materials for unconventional computational devices. Recent developments in nanofabrication techniques have paved the way for research on magnetic metamaterials. Artificial spin ice is a magnetic metamaterial consisting of interacting nanomagnets, often arranged on a two-dimensional surface. It demonstrates fascinating phenomena and has shown to be a promising candidate for applications in unconventional computing [1]. This thesis suggests a methodology for generation of tailormade artificial spin ice designs based on evolutionary algorithms and analyses of magnetic ordering.

flatspin [2], a large-scale artificial spin ice simulator, was used to simulate the complex dynamics in artificial spin ices during thermal annealing protocols. The ordering of magnetic moments following these simulations were analyzed using a "polar" correlation function, developed as a part of this work, and tools from statistical mechanics. This "polar" correlation function successfully discriminated between artificial spin ices with and without long-range magnetic ordering.

Artificial spin ices with nanomagnets arranged in periodic structures as well as geometrically disordered systems were analyzed, showing clear variations in correlation lengths across different geometric designs and temperature ranges. The critical temperature and critical exponent, characterizing the supermagnetic phase transition from long-range ordering to magnetic disorder, were estimated. They identified remaining challenges with the simulator calibration and a component of the analysis when compared to similar studies on experimentally realized artificial spin ices [3].

Evolutionary algorithms were used to search the space of artificial spin ice designs. New geometric designs were generated and evolved based on their corresponding critical temperatures. The magnetic ordering and critical temperatures varied across all designs. Potential weaknesses in the analysis were discussed, concluding with a set of suggested next steps towards a more robust methodology.

Sammendrag

CMOS-teknologi nærmer seg grensen av Moore's lov, og stadig mer oppmerksomhet blir rettet mot potensielle materialer til bruk i ukonvensjonelle datamaskiner. Utvikling i nanofabrikkeringsteknikker har gitt økt fokus og mer forskning på magnetiske metamaterialer. Kunstig spinn is ("artificial spin ice", ASI) er et magnetisk metamateriale som består av interagerende nanomagneter, som regel plassert på en 2D-overflate. Det har demonstrert fascinerende fenomen og er hevdet å være en kandidat til bruk i ukonvensjonelle datamaskiner [1]. Denne oppgaven foreslår en metode for å generere skreddersydde ASI design basert på evolusjonære algoritmer og analyse av magnetisk ordning.

flatspin [2], en storskala ASI simulator, ble brukt til å simulere den komplekse dynamikken i ASI gjennom oppvarmings- og nedkjølingsprotokoller. Ordningen av magnetiske momenter etter disse simuleringene ble analysert ved hjelp av en "polar" korrelasjonsfunksjon, utviklet som en del av dette arbeidet, og verktøy fra statistisk mekanikk. Denne "polare" korrelasjonsfunksjonen klarte å diskriminere mellom ASI med og uten magnetisk ordning.

ASI med nanomagneter plassert i periodiske strukturer og med geometrisk uorden ble analysert, med klare variasjoner i korrelasjonslengde mellom ulike geometriske design of temperaturområder. Den kritiske temperaturen og kritiske eksponenten, som karakteriserer den supermagnetiske faseovergangen fra magnetisk ordning til uorden, ble estimert. De avdekket noen gjenstående utfordringer med kalibrering av simulatoren og en del av analysen når de ble sammenlignet med tilsvarende studier gjort på fabrikkerte ASI [3].

Evolusjonære algoritmer ble brukt til å søke gjennom rommet av mulige ASI design. Nye geometrier ble generert og utviklet basert på sin kritiske temperatur. Den magnetiske ordningen og tilhørende kritiske temperatur varierte mellom ulike ASI design. Potensielle svakheter ved analyser ble diskutert, og konklusjonen innebar et sett med forslag til videre arbeid mot en mer robust metode.

Preface

This Master's thesis concludes a 5 year study program in nanotechnology with specialization in nanoelectronics at the Norwegian University of Science and Technology (NTNU). The work was carried out over the spring semester 2021, supervised by Professor Erik Folven and co-supervised by PhD candidate Anders Strømberg at the Department of Electronic Systems.

I would like to thank my supervisors, Erik Folven and Anders Strømberg, for their willingness to help and guide me through this semester. They have challenged me and provided fruitful discussions, suggestions and feedback from day 1. While regulations to contain the spread of Covid-19 have let us meet in the same room only a few times this semester, Erik and Anders have been flexible and agile on digital communication and minimized the impact of these regulations on my work. Anders has been reachable at most hours of the week, helping me with simulator configuration, debugging and discussions and giving feedback on my written work. For this I am grateful!

I would also like to thank PhD candidate Arthur Penty at the Department of Computer Science for sharing his unpublished work on evolutionary algorithms for artificial spin ice generation and spending hours teaching me how to use the tools.

To my parents and sisters, whose interest in nanotechnology has increased significantly the past 5 years; thank you for supporting and helping me—and for always being my amazing family.

Finally, I would like to thank all the friends I have got to know over 5 amazing years at NTNU. I will surely miss the collective struggling, success and failures we have had these years. My good friends and roommates Knut, Martin and Torstein have helped me balance my studies with ski trips, beer brewing and memorable experiences. Thank you!

Trondheim, June 2021

Contents

Chapter 1

Introduction

1.1 Background and Motivation

The brain has fascinated and inspired researchers for centuries and remains the ultimate goal for an unconventional computational device. Despite—or even because of—decades of developing and perfecting CMOS technology, we are far from having a computer that can compete with the human brain. Image recognition and learning are areas where the brain is particularly superior to state of the art digital computers and artificial intelligence. A housefly with a hundred thousand neurons can easily outperform state of the art autonomous vehicles when it comes to navigating obstacles [4]. A rough estimate from 1990 predict that energy-wise, the brain is a factor of 10^6 more efficient than the best digital technology imaginable [5]. Despite leaps in semiconductor manufacturing technology since then, the physical limitations at the atomic scale remain. The authors' point is at least as relevant today: There is something fundamentally different between the way a biological brain and a digital computer works.

Neuromorphic computers use inherent physical phenomena as computational primitives. This is in contrast to the digital computer, where computations are forced to fit into a set of digital gates. Ensembles of interacting nanomagnets have been suggested for such a basis [1, 6]. Artificial spin ices (ASIs), a type of magnetic metamaterial, have demonstrated fascinating phenomena such as frustration and phase transitions [7]. By carefully placing individual nanomagnets to form custom geometric designs, one can potentially tailor the energy landscape and magnetic properties of these metamaterials. Square and Ising are two ASI designs that exhibit different emergent behavior.

The term "artificial spin ice" refers to ensembles of nanomagnets organized such that their magnetic moments are frustrated, analogous to the geometric frustration in common crystalline water ice. In this work, we will use the term for all ensembles of nanomagnets, regardless of the level of frustration and configuration of magnetic moments. Our focus will be on two-dimensional ASIs, although the term can also refer to systems in three dimensions. Three-dimensional ASIs were recently produced and used to study magnetic charge propagation, a phenomena that has captivated scientists [8].

The smallest building blocks in ASI are single domain ferromagnets with sub-micron dimensions, commonly referred to as macrospins. The mesoscopic size makes them large enough to directly observe the magnetic configuration using magnetic microscope techniques while at the same time small enough to mimic the behavior of atomic spin magnetic moments. Recent developments in nanofabrication techniques have sparked reasearch on ASIs and enabled easy fabrication of large two-dimensional ensembles of these nanomagnets with few limitations on geometric design. Skjærvø *et al.* wrote in their review paper that "the only limitation on possible designs is the

imagination of the designer" [7]. The *imagination of the designer* may be a significant barrier towards the realization of exotic ASIs that exhibit complex, yet deterministic, dynamics. There is a fine balance between a complex energy landscape and non-deterministic random behavior.

Modern integrated circuits (IC) are complicated and can typically have more than 1 billion transistors. It would be a cumbersome and near impossible job for engineers to design computer chips by hand, which is why electronic computer-aided design (ECAD) software are essential tools in the IC industry. One can imagine a computational ASI device to have a complex design, perhaps with separated clusters of nanomagnets that can perform different tasks, and channels of more densely placed nanomagnets connecting them with input and output ports. Tools similar to ECAD does not exist for ASI designs, and building just a simple design tool could represent a leap in the research and potential realization of more complex ASIs.

In the SOCRATES project they proposed a strategy for building an ASI design tool based on evolutionary algorithms [9]. Evolutionary algorithms, a machine learning technique, can generate a large number of ASI designs [10]. It has been hypothesized that with a suitable fitness function, one can search the full space of fabricable designs and evolve to the best design based on a set of desired properties. These can either be related to microscopic properties of the ASI, like the number of available microstates, or macroscopic magnetic properties, like the critical temperature of the ASI. Such inverse design would go far beyond the time-consuming brute-force method based on the *imagination of a designer*, and would establish an important tool towards the realization of computational ASI devices.

1.1.1 Project Overview

This master's thesis is a continuation of a specialization project on ASIs that was done over the fall semester 2020. That work included developing a route for fabrication and characterization of ASIs. Several different ASI designs were successfully fabricated at NTNU NanoLab's cleanroom facilities using a fabrication route that will be described in Section 2.3.1. Scanning electron microscope (SEM) and magnetic force microscope (MFM) were used to characterize the fabricated samples and their magnetic configuration. SEM and MFM images for two of these samples can be seen in Figure 1.1.

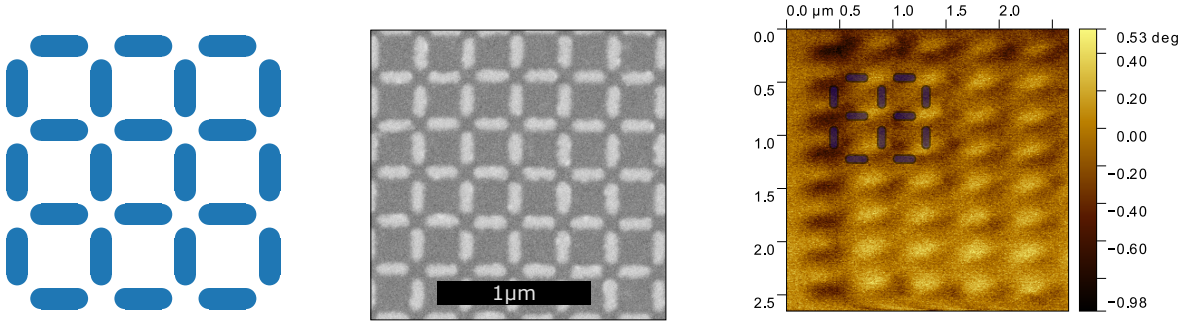

(a) (b) (c)

Figure 1.1: Experimentally realized ASI. (a) shows a schematic of a "square ASI". (b) scanning electron micrograph depicts a subset of the nanomagnets in a "square ASI", and (c) is an MFM image where the contrast represents the phase difference caused by local magnetic fields when scanning a region of the sample. The shaded rectangles in the MFM image are approximate positions of the nanomagnets.

With a robust ASI fabrication route well established, this work will focus on developing a method to find new, exotic ASI designs. The overall goal is to propose a methodology that can be used

to build the abovementioned fitness function for use in evolutionary algorithms.

Saccone *et al.* used tools from statistical mechanics to determine magnetic properties of experimentally realized ASIs [3]. They generated new ASI designs by blindly changing the position and rotation of nanomagnets in an Ising ASI and identified critical temperatures and order parameters for these systems. Here, we will build on a similar approach, but go one step further. The goal is not only to be able to characterize simulated ASIs, but to be able to discriminate within a family of suggested designs based on desired magnetic properties. A key ingredient in such an analysis is the spatial spin-spin correlation function. We will propose a novel correlation function that is more general and can capture order in systems where the nanomagnet positions have no requirement on periodocity and can have independent element-wise rotations.

The experimental work in Chapter 3 consists of five parts. First, we will introduce the ASI models used in simulations and describe how they are generated. We will then proceed by simulating these models using flatspin, a novel ASI simulator. Next, a generalized spatial spin-spin correlation function will be proposed and described. We will go through verification and validation to find a optimal configuration of the correlation function and identify any strengths and weaknesses. Comparison with the correlation function described by Saccone *et al.* will be done for reference and to motivate why a more general function is necessary. The fourth part will analyze magnetic ordering in simulated ASIs using the generalized correlation function and tools from statistical mechanics. The goal is to be able to discriminate between different systems in terms of magnetic phases and order parameters, which again can be used in a fitness function. Finally, we will take steps to generate new, exotic ASI designs using evolutionary algorithms with a fitness function based on the above analysis.

Chapter 2

Theory and Literature

This section provides the theoretical background necessary to follow the work and discussion in this thesis. Relevant literature is included where suitable, especially related to the theory and analysis of artificial spin ice. Parts of this chapter are adapted from the specialization course thesis done on ASI over the fall semester 2020.

Sections 2.1 through 2.3 covers classical magnetism, types of magnetic ordering and the fundamentals of artificial spin ice. Knowledge about these topics are required to follow the work and related discussions in this thesis. Principles of magnetic fields, the dipole model, ferromagnetic materials and magnetic domains are important to understand artificial spin systems. They are the foundation for how neighboring nanomagnets interact with each other and why they can be referred to as "macrospins". Furthermore, knowledge about microscopic magnetic ordering and typical macroscopic properties for various magnetic materials is useful when comparing the magnetic *meta*materials built from thousands of nanomagnets.

In Section 2.4 and 2.5 we discuss the spatial correlation function and relevant statistical mechanics, which is useful in the analysis of ASI simulations. Finally, a brief introduction to evolutionary algorithms and how they can be used to generate ASI designs is given in Section 2.6.

2.1 Classical magnetism

In everyday life, magnetism often refers to the macroscopic properties that allow refrigerator magnets to stick to the refrigerator door or a compass needle to point towards earth's magnetic north pole. The refrigerator magnet and the compass needle, with their north pole and south pole, are often modelled as magnetic dipoles. The magnetic dipole model is a simple, yet powerful model when studying magnetism. Later in this chapter, both interactions in ASI and the magnetic properties of any material, are described in intuitive terms using this model.

Gauss' law for magnetism states that all magnetic fields must be divergence free. With the magnetic field denoted by $\mathbf{H}$ on vector form, this law can be written as $\boldsymbol{\nabla} \cdot \mathbf{H} = 0$, i.e., there are no sources or sinks for magnetic fields [11]. A consequence of Gauss' law for magnetism is that magnetic monopoles, analogous to electric monopoles in electric studies, cannot exist. The magnetic dipole, or dipole moment, is therefore the basic entity in classical magnetic studies.

The magnetic dipole has a magnetic moment, $\mathbf{m}$, with direction pointing from its south to north pole. When an external static magnetic field is present, the dipole has magnetic potential energy, also known as Zeeman energy,

$$E_z = -\mu_0 \mathbf{m} \cdot \mathbf{H}, \tag{2.1}$$

where $\mathbf{H}$ is the external magnetic field and μ_0 is the vacuum permeability. E_z is minimized when the dipole moment and the magnetic field are aligned and point in the same direction ($E_\mathrm{z} < 0$) and maximized when they point in opposite directions ($E_\mathrm{z} > 0$). When the magnetic field is normal to the dipole moment, the dot product in Eq. (2.1) gives $E_\mathrm{z} = 0$.

A dipole moment interacts with the environment through a magnetic field. It can be shown that the magnetic field from a magnetic point dipole with magnetic moment $\mathbf{m}$ at position $\mathbf{r}$ is [12]

$$\mathbf{H}_\mathrm{dip}(\mathbf{r}) = \frac{1}{4\pi}\Big(\frac{3(\mathbf{m}\cdot\mathbf{r})\mathbf{r}}{|\mathbf{r}|^5} - \frac{\mathbf{m}}{|\mathbf{r}|^3}\Big). \tag{2.2}$$

This is a general relation, valid as long as the separation distance, $|\mathbf{r}|$, is much larger than the size of the dipole moment exhibiting the field. The macrospins in an ASI are often modelled as point dipoles, and Eq. (2.2) is an essential expression in the simulator used in this work. A visualization of a typical point dipole field can be seen in Figure 2.1.

If no other magnetic fields are present, Eqs. (2.1) and (2.2) can be combined to describe how two neighboring dipole moments, $\mathbf{m}_i$ and $\mathbf{m}_j$, separated by $\mathbf{r}_{ij}$, will be affected by the dipolar magnetic field set up by its neighbor:

$$E_\mathrm{z,dip} = -\frac{1}{4\pi}\Big(\frac{3(\mathbf{m}_i\cdot\mathbf{r}_{ij})(\mathbf{m}_j\cdot\mathbf{r}_{ij})}{|\mathbf{r}_{ij}|^5} - \frac{\mathbf{m}_i\cdot\mathbf{m}_j}{|\mathbf{r}_{ij}|^3}\Big). \tag{2.3}$$

An important consequence of the above expression is that by flipping the direction of one of the dipoles ($\mathbf{m}_i \to -\mathbf{m}_i$), the sign of the magnetic potential energy, $E_\mathrm{z,dip}$, is also flipped. The dipole interactions and such "flips" are what can create a complex energy landscape when thousands of macrospins are combined in an ASI.

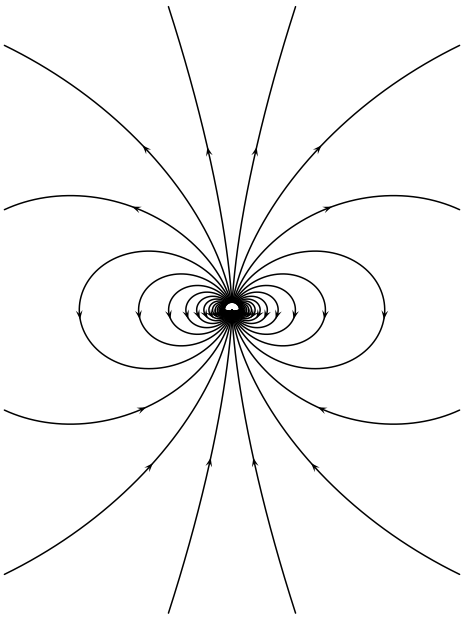

Figure 2.1: THe magnetic field exhibited by a point dipole, according to Eq. (2.2). The magnetic moment of the point dipole is here directed upwards in the plane. All field lines are running in closed loops (not shown for the 6 largest loops).

2.1.1 Origins of magnetism

Today's well established theory of electromagnetism and quantum mechanics describe two different mechanisms giving rise to magnetic moments and magnetic fields; moving electric charges and intrinsic spin magnetic moments. Moving electric charges are well described by classical electrodynamics [13], but is less relevant for this work and will not be discussed.

Intrinsic spin magnetic moments arise from the intrinsic spin of elementary particles, and are the reason why materials can create and respond to magnetic fields. The spin magnetic moment, μ_{S}, is proportional to the spin angular momentum, $\mathbf{S}$. For the electron, a spin-1/2 fermion, the spin magnetic moment is

$$\mu_{\mathrm{S}} \approx \frac{e\hbar}{2m_{\mathrm{e}}}\mathbf{S}, \tag{2.4}$$

where e and m_{e} are the elementary charge and electron mass, respectively, and $\hbar$ is the reduced Planck's constant [14]. The magnitude of μ_{S} is called the Bohr magneton. It is a natural unit of magnetic moment, with value $\mu_{\mathrm{B}} = 9.27 \times 10^{-24}\,\mathrm{J\,T^{-1}}$ [15]. While the magnetic moment of atoms is on the order of μ_{B}, the magnetic moment of the nanomagnets modelled in this work are typically 6 orders of magnitude larger [3].

The magnetic dipole moment of an atom is due almost entirely to the electrons of the atom. Electrons in an atom contribute to a net magnetic moment with their intrinsic magnetic moment given by Eq. (2.4) and an orbital angular momentum caused by the electron's movement about the nucleus. In most materials however, these magnetic moments cancel each other. The Pauli exclusion principle states that two electrons in the same orbital must have spin vectors with opposite directions (up and down). They will thus cancel the overall magnetic moment. Only atoms with unpaired spins can have a nonzero net magnetic moment. Iron, a widely used ferromagnetic material, has electron configuration $[\mathrm{Ar}]3\mathrm{d}^6 4\mathrm{s}^2$ [16]. 4 of the 6 electrons in the 3d orbital are unpaired, explaining the strong magnetic properties of iron. The atomic nucleus also has a magnetic moment, but that is negligible compared to the Bohr magneton and irrelevant for the total magnetic moment in a material.

2.2 Magnetic Materials

Magnetic materials in everyday life typically refers to ferromagnets with permanent magnetization, such as the refrigerator magnet or a compass needle. In the field of physics, this is just one of many types of magnetic materials. While other types of magnetism often are weak or do not produce tangible effects, this does not mean they are not magnetic.

All materials respond to magnetic fields on an atomic level, regardless if the effect can be observed on a macroscopic level or not. Some materials will obtain or reverse a permanent magnetization, others will obtain a magnetization as long as the field is present, and most materials will feel a weak repulsive or attractive force.

The magnetic susceptibility, χ, indicates how responsive a material is to an external magnetic field. If $\mathbf{H}$ is the applied field and $\mathbf{M}$ is the material's magnetization in that field, they are related by:

$$\mathbf{M} = \chi\mathbf{H}. \tag{2.5}$$

Some material have a simple linear relationship between $\mathbf{M}$ and $\mathbf{H}$, whereas others have a characteristic hysteresis curve describing the relationship. The magnetic properties of a material

are often described in terms of its relative permeability, μ_r. The relative permeability is related to the magnetic susceptibility as [17]:

$$\chi = \mu_r - 1. \tag{2.6}$$

Materials are classified according to their magnetic properties and types of ordering of microscopic magnetic moments. Diamagnetism, paramagnetism, ferromagnetism and antiferromagnetism are common types of magnetic ordering. Sections 2.2.1 through 2.2.4 describe some of these types in terms of susceptibility and magnetization. The internal mechanisms giving rise to this variation in magnetic properties are explained using the localized moment theory [18, 19, 20]. This is relevant in order to understand both the building blocks in ASI, and the complex dynamics and temperature dependence when thousands of them are combined.

2.2.1 Diamagnetism

Diamagnetism is characterized by a weak negative susceptibility, sometimes referred to as "negative magnetism". In diamagnetic materials, all the magnetic moments of electrons have been cancelled out, leaving a net zero magnetic moment on each atom and thus the system as a whole [18]. When an external magnetic field is applied, magnetic moments will minimize the magnetic energy by aligning antiparallel to the external field. This corresponds to a negative susceptibility, illustrated in Figure 2.2. In extreme cases, the macroscopic effect can be "visible to the naked eye" as a repulsive force [21]. Diamagnetism appears in all materials, but is usually weak and quickly dominated by other effects.

2.2.2 Paramagnetism

While the nanomagnets commonly used as building blocks in ASIs do not exhibit paramagnetism, paramagnetic theory is relevant to understand the temperature dependence in ASIs. Paramagnetism can be explained from both a classical and quantum mechanical perspective. The classical approach, based on localized magnetic moments, is more relevant for this work and provides useful analogies to the macrospins in ASIs. Here follows an account of classical paramagnetic theory, adapted from Cullity *et al.* [18] and Spaldin *et al.* [22].

Langevin was first to describe this theory in 1905. He assumed that, unlike for diamagnetism, each atom has a magnetic moment $\mathbf{m}_\mathrm{i} \neq \mathbf{0}$, meaning all the spin and orbital magnetic moments of the electrons do not cancel out. Furthermore, he assumed that neighboring $\mathbf{m}_i$ are only weakly coupled. This weak interaction can for instance be a result of atomic bonds or a crystal structure giving sufficient separation between individual atoms (Eq. (2.2), $\mathbf{H}_\mathrm{dip} \sim |\mathbf{r}|^{-3}$). With no external magnetic field, these magnetic moments point in random directions due to thermal agitation. Summing randomly oriented magnetic moment vectors together naturally yield a net zero magnetization, denoted by the vector $\mathbf{M}$:

$$\mathbf{M} = \sum \mathbf{m}_i = \mathbf{0}, \qquad \mathbf{H} = \mathbf{0}. \tag{2.7}$$

When an external magnetic field is applied, the microscopic magnetic moments will try to align parallel with the field, so as to minimize the Zeeman energy in Eq. (2.1). The result is a net magnetization of the material and a positive susceptibility. A comparative illustration of the magnetization curves for a diamagnetic and a paramagnetic material can be seen in Figure 2.2.

The average magnetization of a paramagnetic material in an external magnetic field can be estimated using Boltzmann statistics. The probability $p(\theta)$ that an atomic magnetic moment

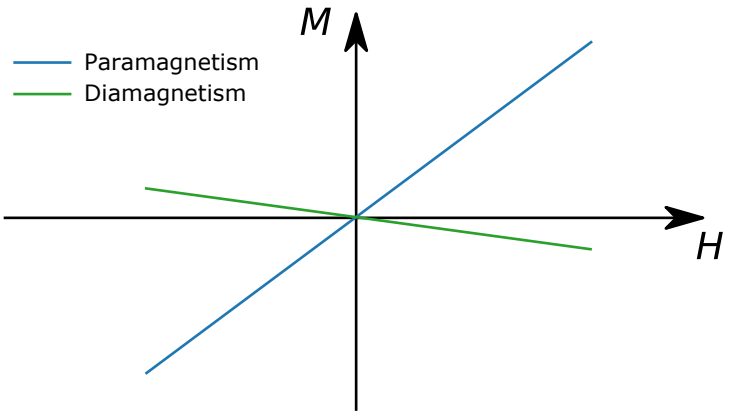

Figure 2.2: The magnetizations, **M**, of diamagnetic and paramagnetic materials are linearly related to the external magnetic field, **H**. Diamagnetism is characterized with a weak negative susceptibility (green line) and paramagnetism have a positive susceptibility (blue line).

with magnitude m has an angle between θ and $\mathrm{d}\theta$ with respect to the magnetic field of magnitude H is:

$$p(\theta) = \frac{e^{\mu_0 m H \cos\theta / k_\mathrm{B} T} \sin\theta \mathrm{d}\theta}{\int_0^\pi e^{\mu_0 m H \cos\theta / k_\mathrm{B} T} \sin\theta \mathrm{d}\theta}, \tag{2.8}$$

where $k_\mathrm{B}T$ is the thermal energy. If the material consists of N magnetic moments, the overall magnetization is

$$M = Nm\langle\cos\theta\rangle = Nm \int_0^\pi p(\theta)\cos\theta \mathrm{d}\theta, \tag{2.9}$$

with direction parallel to the magnetic field. $\langle\cos\theta\rangle$ is the expectation value of $\cos\theta$, given by the integral over $p(\theta)$. The solution can be expressed as

$$M = NmL(\alpha) = Nm\Big[\coth\Big(\frac{\mu_0 m H}{k_\mathrm{B} T}\Big) - \frac{k_\mathrm{B} T}{\mu_0 m H}\Big], \tag{2.10}$$

where $L(\alpha)$ is called the Langevin function and $\alpha = \mu_0 m H / k_\mathrm{B} T$ defines the ratio between the Zeeman energy and thermal energy. For low values of α, random thermal fluctuations dominate, giving a low average net magnetization. A high value for α can be reached at low temperatures with a strong, external magnetic field, thus giving a high net magnetization.

Curie's law can be obtained by Taylor expansion of the Langevin function and states $\chi \sim 1/T$. The law was generalized by Weiss to also account for materials where neighboring atomic magnetic moments interact strongly with each other:

$$\chi = \frac{C_\mathrm{curie}}{T - T_\mathrm{C}}. \tag{2.11}$$

Here, C_curie is the Curie constant for the material, T is the absolute temperature and T_C is the critical temperature. Eq. (2.11) is known as the Curie-Weiss law, and is valid for $T > T_\mathrm{C}$. It predicts a linear relationship between the inverse magnetic susceptibility and temperature. This temperature dependence will be useful when studying the thermal response of ASIs in Chapter 3.

Below the critical temperature, the material undergoes spontaneous ordering and is no longer paramagnetic. Types of magnetic ordering caused by strong interactions between neighboring

magnetic moments will be the topics for the two next sections, describing ferro- and antiferromagnetism.

2.2.3 Ferromagnetism

Ferromagnetism covers the type of spontaneously magnetized materials we commonly know as "magnetic materials" in everyday life. The strong permanent magnetization found for instance in refrigerator magnets is a result of a strong exchange interaction between neighboring atomic magnetic moments. The nanomagnets used as building blocks in ASI are also examples of objects made from ferromagnetic materials.

Ferromagnetic theory is relevant in order to understand how the magnetic properties of the ASI building blocks are determined from their size, shape and temperature. It will also provide useful tools in the magnetic analysis of ASI.

This section gives an account of ferromagnetic theory, primarily adapted from the works by Spaldin *et al.* [23, 24, 25]. Again, we follow the classical approach, which is more relevant. We first use Weiss theory of ferromagnetism to explain how exchange interactions can give rise to a spontaneous magnetization in some materials. Magnetic domains and characteristics of single domain ferromagnets are then described, focusing on the effects that are particularly relevant for this work.

There is a strong internal interaction that favor parallel alignment between the constituent atomic magnetic moments in a ferromagnetic material. Weiss described this neighbor interaction between localized magnetic moments using a "molecular field", or Weiss field, denoted by the vector $\mathbf{H}_{\mathrm{W}}$. In classical terms, the Weiss field can be thought of as a weak magnetic field responsible for the neighbor interactions between adjacent atomic magnetic moments. There is a linear relationship between the Weiss field and the material's net magnetization, $\mathbf{M}$. This relationship is described with the constant, γ, called the molecular field constant:

$$\mathbf{H}_{\mathrm{W}} = \gamma \mathbf{M}. \tag{2.12}$$

The above equation gives another expression for a material's magnetization, in addition to that predicted by Langevin theory in Eq. (2.10). With no external magnetic field, $\alpha = \mu_0 m H_{\mathrm{W}}/k_{\mathrm{B}}T$, where H_{W} is the magnitude of the Weiss field. Spontaneous magnetization can be explained by plotting these two curves together as a function of α, illustrated in Figure 2.3.

For high values of α (low temperature or high molecular field), the material is spontaneously magnetized and exhibit long-range magnetic ordering. The point M_{spont} in Figure 2.3 is where the two magnetization curves intersect. M is the magnitude of the magnetization vector, $\mathbf{M}$, which point in the same direction as the aligned atomic moments. As the temperature is increased, the slope of the linear function increases, until eventually the only intersection between the two curves is at the origin. This occurs at the critical temperature, T_{C}, where the material enters the paramagnetic phase (dashed orange line in Figure 2.3). Using Eqs. (2.10) and (2.12), it can be shown that the critical temperature can be expressed as [23]:

$$T_{\mathrm{C}} = \frac{\gamma N m^2}{3k_{\mathrm{B}}}. \tag{2.13}$$

We will use this expression to discuss the critical temperatures obtained for ASIs in this work and find an effective "molecular field constant" describing the interactions between macrospins in Chapter 4.

Above the critical temperature, thermal effects dominate the internal interactions, giving a net zero magnetization. The magnetic ordering is then described using the theory of paramagnetism from the previous section. The phase transition from ordered to disordered magnetic phases is a second order continous phase transition that will be central in the analysis of magnetic ordering in ASIs in Chapter 3. In the paramagnetic phase, the magnetic susceptibility decreases with increasing temperature as predicted by the Curie-Weiss law from Eq. (2.11).

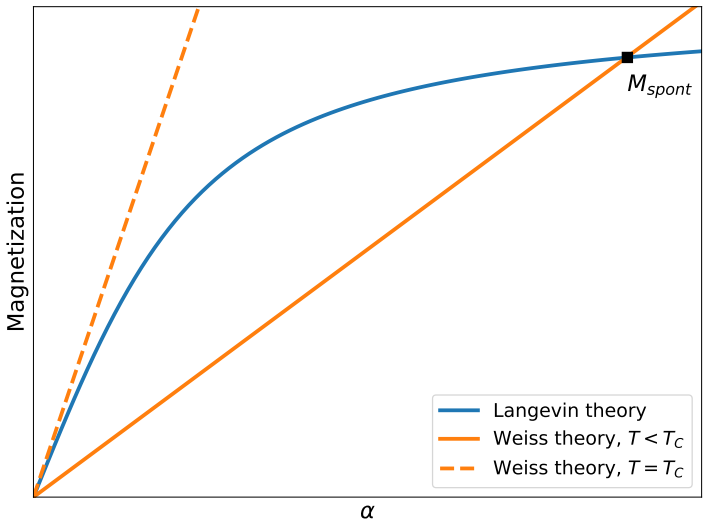

Figure 2.3: Ferromagnets are spontaneously magnetized, as described by Weiss theory. The point M_{spont} is the intersection between Eqs. (2.10) and (2.12). As the temperature is increased to T_{C}, the material is no longer spontaneously magnetized (dashed orange line).

Despite having a microscopic spontaneous magnetization, many bulk ferromagnetic materials do not appear to be magnetized. Simple examples of this are screw drivers made from ferromagnetic materials, with and without a permanent magnetization. A ferromagnetic material can have net zero magnetization due to the formation of magnetic domains. Ferromagnetic domains are small regions where all the atomic magnetic moments are aligned, but neighboring domains can be magnetized in different directions. If the domain magnetizations in a ferromagnetic material point in random directions, the overall bulk magnetization will be zero or close to zero, illustrated in Figure 2.4a. An external magnetic field can be applied to align the direction of the magnetic domains with the field. This new direction will remain even when the external field is gone. As a result, the bulk has a nonzero net magnetization, seen in Figure 2.4b.

The overall magnetization of a bulk ferromagnet depends on the history of applied magnetic fields, defining a a characteristic magnetization hysteresis curve. The magnetization curve for a typical bulk ferromagnetic material is sketched in Figure 2.5. As the external field is increased, the magnetization increases towards its saturation value, M_{sat}, and remains nonzero even when the external field is gone. H_{c}, the coercive field, is a measure of how large magnetic field the material can withstand in the opposite direction without becoming demagnetized.

The formation of magnetic domains is a thermodynamic consequence of the total magnetic energy in a ferromagnet. A single domain ferromagnet exhibits a demagnetizing field at the expense of magnetostatic energy, thus satisfying Gauss' law for magnetism ($\boldsymbol{\nabla} \cdot \mathbf{H} = 0$). The demagnetizing field is what makes it possible to do work on other objects with a magnetic moment, such as lifting them against the force of gravity. By forming magnetic domains, the overall magnetic energy is reduced. This process is illustrated in Figure 2.6. Other factors such as the material's crystal structure also affect the final domain structure.

The boundaries between adjacent domains are called domain walls, typically around 10 µm in

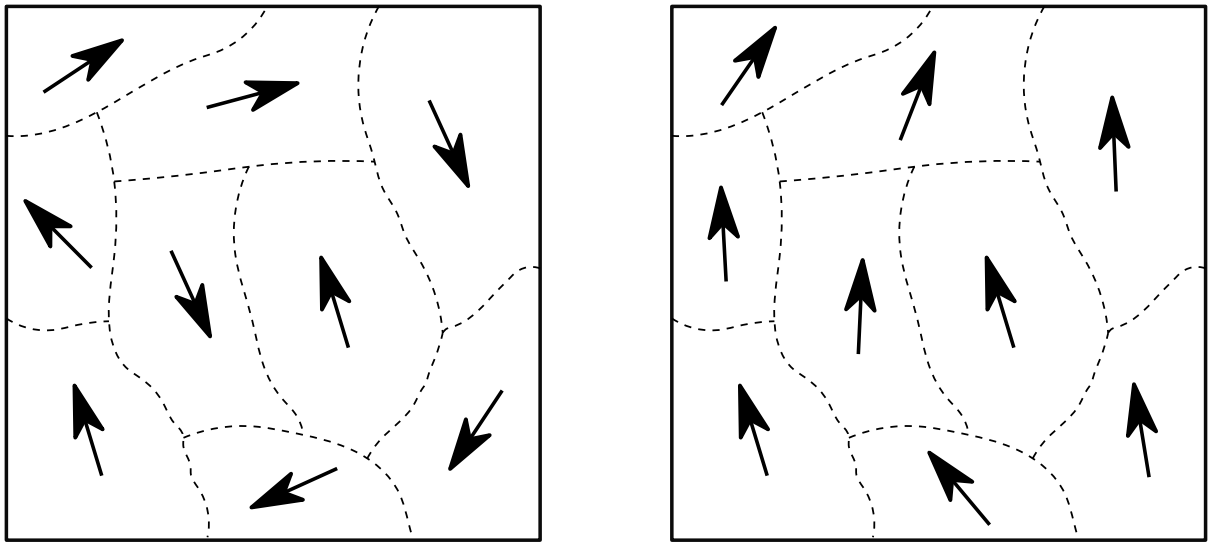

(a) (b)

Figure 2.4: Ferromagnetic domains with magnetic moments (a) randomly oriented give a net zero magnetization, or (b) oriented in almost the same direction using an external magnetic field give a nonzero net magnetization. This magnetization remain after the field has been removed.

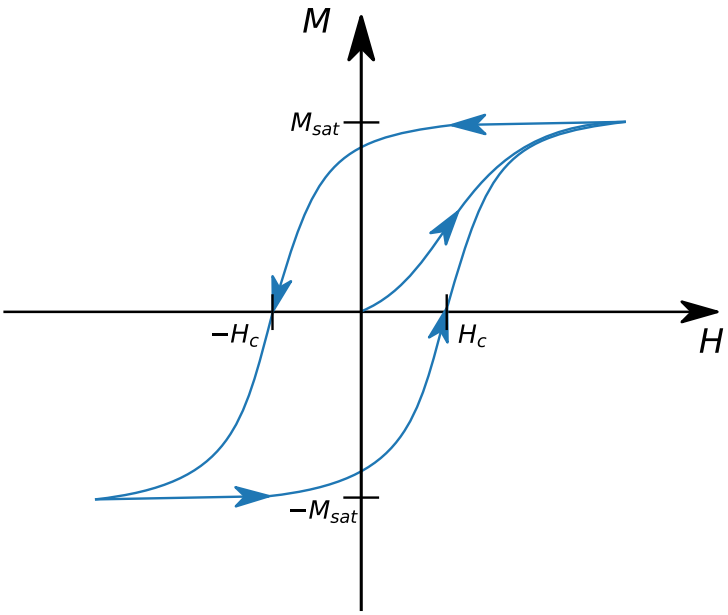

Figure 2.5: The hysteresis magnetization curve for a bulk ferromagnet with several magnetic domains. $H = 0$ can give either a "positive", "negative" or zero magnetization, depending on the history of external magnetic fields.

thickness for bulk ferromagnetic materials. Since the exchange energy favors parallel alignment and the domain wall consists of magnetic moments that are rotated with respect to each other, there is an associated cost in exchange energy when forming a domain wall. As the bulk ferromagnet is scaled down towards nanometer size, the energy cost of creating domain walls exceeds the savings from reducing magnetostatic energy, and it will eventually be advantageous to only have a single domain [26]. The nanomagnets used in ASIs must be single domain, giving strong magnetic moments with corresponding strong demagnetizing fields that are responsible

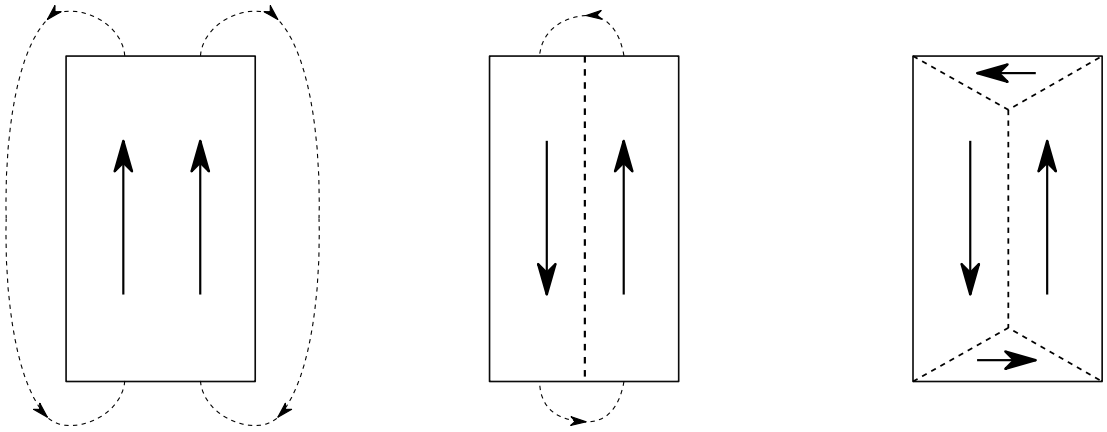

(a) (b) (c)

Figure 2.6: Formation of magnetic domains reduces the magnetistatic energy and demagnetizing field exhibited by a ferromagnet. The dashed line inside the rectangles represent magnetic domain walls, separating regions of aligned magnetic moments. Each domain is represented using only one arrow. The dashed lines outside the rectangles in (a) and (b) are the demagnetizing fields. (a) is called single domain, while the domain setup in (c) is called flux closure and exhibits no demagnetizing fields.

for neighbor interactions. The sizes and shapes that can be used for nanomagnets in ASI are therefore typically restricted to submicron dimensions.

Elongated single domain ferromagnets will prefer to have their magnetic moments pointing along the elongated axis because of shape anisotropy. This preferred direction is also known as the "easy axis". Conversely, the perpendicular "hard axis" is less favorable and is associated with a less stable magnetization. The magnetization of a single domain ferromagnet has a sharp transition when a sufficiently strong external field in the opposite direction is applied. This binary magnetization behavior can be identified from the square-like hysteresis curve seen in Figure 2.7.

Single domain ferromagnets are often referred to as macrospins, analogous to the intrinsic spin magnetic moments in elementary particles. The 180° instantaneous change in magnetization direction is known as a "flip" or "switch" and is an important feature of the building blocks in ASI. The nanomagnet "flips" are caused entirely by reversal of almost all the atomic magnetic moments in the nanomagnet. There are no movements or rotations related to the nanomagnet itself, which typically is fixed on a substrate.

2.2.4 Antiferromagnetism

Antiferromagnetism is another type of magnetic ordering where strong internal interactions dominate thermal fluctuations. The exchange interaction between adjacent atomic magnetic moments in antiferromagnet materials favors antiparallel alignment. It can be modelled as two identical, interpenetrating but oppositely aligned sublattices of magnetic moments. As a result, materials exhibiting antiferromagnetism have no net spontaneous magnetization [20]. Their response to an external magnetic field is similar to that of paramagnetic materials, with a small positive susceptibility.

The ordering of macrospins in Ising ASI show clear analogies to antiferromagnetic ordering. This similarity will be further described when discussing supermagnetism in Section 2.3.2.

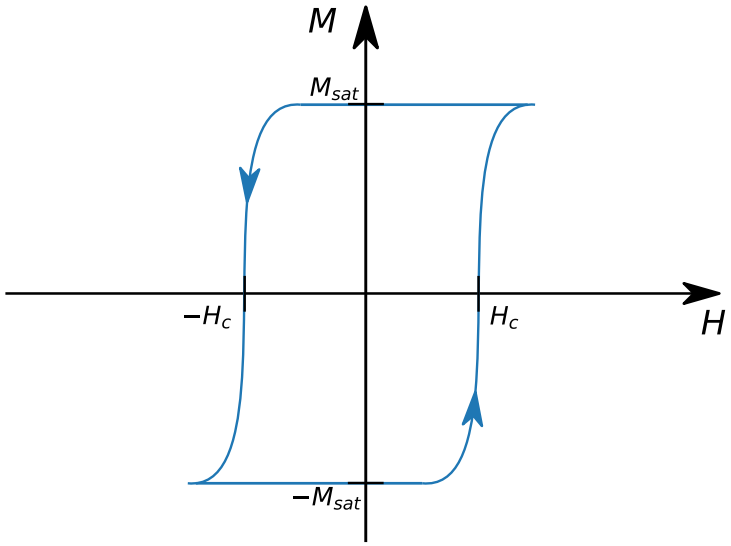

Figure 2.7: Single domain ferromagnets have a square-like hysteresis magnetization curve, giving a sharp transition when the magnetization is flipped.

The Weiss ferromagnetic theory can be extended to also account for antiferromagnetism. Using two sublattices A and B with oppositely directed molecular fields such that

$$\mathbf{H}_{\mathrm{W}}^{\mathrm{A}} = -\mathbf{H}_{\mathrm{W}}^{\mathrm{B}}, \tag{2.14}$$

it can be shown that the susceptibility follow a Curie-Weiss law

$$\chi = \frac{C_{\mathrm{Curie}}}{T + T_{\mathrm{C}}}, \tag{2.15}$$

where the difference from Eq. (2.11) is the sign in the denominator [20].

Materials with antiferromagnetic ordering have recently drawn increasing attention due to the compatibility with CMOS technology and potential applications in high-density storage [27].

2.3 Artificial spin ice

Wang *et al.* introduced the concept of an artificial geometrically frustrated magnetic material based on single domain ferromagnetic islands with sub-micron dimensions (nanomagnets) [28]. Artificial spin ices are metamaterials engineered by arranging nanomagnets on a lattice, introducing frustrations analogous to those in regular water ice. Typical geometries include square, kagome, Ising and pinwheel ASI [7]. Schematic illustrations of these geometric designs can be seen in Figure 2.8. The nanomagnets interacts with each other through their dipolar magnetic fields, referred to as demagnetizing fields in the previous section. External magnetic fields can also be applied to perturb the energy landscape formed by these interacting nanomagnets. The sum of the dipolar and external magnetic fields at every nanomagnet location can flip the magnetization of that nanomagnet if the component in the longitudinal direction is antiparallel to the direction of the nanomagnet's magnetic moment and exceeds its coercive field.

The collective behavior of nanomagnets in ASI can give rise to complex dynamics such as phase transitions [29], long-range order [30] and emergent magnetic monopoles [31]. The large number of possible geometries and microstates, i.e., different macrospin configurations, have potential

applications in computational devices [7, 1]. It has also been suggested to use ASI to control topological properties of light [32].

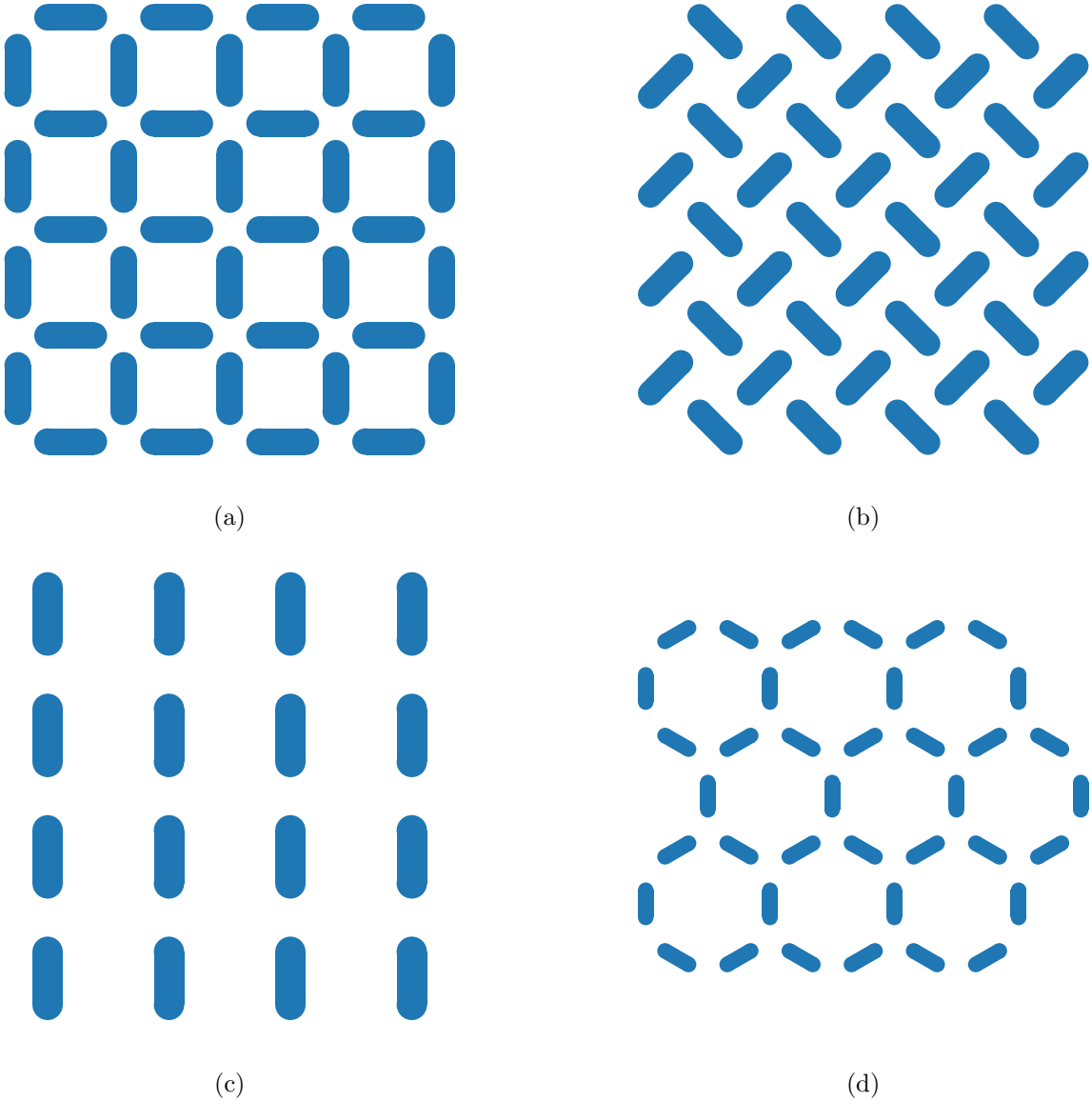

Figure 2.8: Schematic illustration of typical ASI designs. (a) square, (b) pinwheel, (c) Ising and (d) kagome are all well described in the literature. Magnetic ordering in square, Ising and pinwheel ASIs are analyzed in this work.

2.3.1 Fabrication of artificial spin ice

Advances in nanofabrication techniques have enabled easy fabrication of high quality ASIs. Here, in particular, ASIs refer to ensembles of nanomagnets with no requirement on periodicity, beyond the traditional square, pinwheel, Ising and kagome ASIs. The individual nanomagnets can be customized in terms of shape, thickness, material composition, position and orientation, enabling far more exotic systems than those illustrated in Figure 2.8.

The following account of ASI fabrication is based on experimental work that was done in the specialization project leading up to this master's thesis. A brief overview was given in Chapter 1, together with SEM and MFM images of fabricated structures in Figure 1.1.

A typical fabrication route is based on lift-off assisted electron beam lithography (EBL). State-of-the-art EBL systems can produce patterns with feature sizes from digital masks down to a few nm. The single domain nanomagnets used in artificial spin ice have in-plane dimensions ranging from $\sim 50\,\text{nm}$ to a few hundred nm.

Permalloy, a soft ferromagnetic material consisting of about 80% nickel and 20% iron, is commonly used. The thickness is typically somewhere between 2 nm and 20 nm, ensuring mostly in-plane magnetic moments. This can be deposited on top of a patterned electron resist with precise thickness control using electron beam evaporation. The final step is lift-off, leaving only the patterned nanomagnets on the wafer.

The nanomagnets are fabricated as elongated rectangles with rounded corners, as illustrated in Figure 2.8. Increased size or variations in aspect ratio could introduce magnetic domain walls, not desired in ASI building blocks [26].

Arrays of dipolar-coupled magnetic nanodisks have also been fabricated [33]. Circular disk nanomagnets do not show the same shape anisotropy and thus do not exhibit the binary "switching" behavior seen for elongated nanomagnets.

2.3.2 Supermagnetic phases in artificial spin ice

Interactions between the macrospins (or superspins) in ASIs and their analogy to atomic magnetic moments give rise to a phenomena known as supermagnetism. Several types of supermagnetic phases exist, similar to those described for regular materials in Section 2.2. The localized moment theory can also be applied to describe ordering and susceptibility in supermagnetic systems.

Superparamagnetism describes a supermagnetic phase where the magnetic dipolar couplings are weak compared to the thermal energy, giving random spin configurations. For the special case where all the magnetic moments are aligned parallel to an external magnetic field, the Langevin function in Eq. (2.10) is replaced with the Brillouin function with $J = \frac{1}{2}$ [34]:

$$M = Nm \tanh(\alpha). \tag{2.16}$$

The magnetic susceptibility of a superparamagnetic material is orders of magnitude larger than that of regular paramagnetism. From Eq. (2.5) and (2.10), we see that the susceptibility scales with the magnetic moment of the magnetic building blocks. For atomic magnetic moments, that is on the order of a Bohr magneton, whereas it is orders of magnitude larger for the nanomagnets composing an ASI. The magnetic moment of a single domain nanomagnet is

$$M = M_{\text{sat}} V, \tag{2.17}$$

where V is the volume of the nanomagnet. It has been suggested that the swithing, i.e., reversal of magnetization occurs via nucleation and propagation, yielding an effective nucleation volume smaller by more than an order of magnitude [35]. For Permalloy Ising type nanomagnets, the saturation magnetization is around $M_{\text{sat}} = 860\,\text{kA m}^{-1}$, giving a magnetic moment about six orders of magnitude larger than the Bohr magneton [3]. The magnitude of the magnetic moment can to a large extent be tailored as desired by modifying the dimensions and material composition of the nanomagnets. Figure 2.9a is a schematic of an Ising ASI at an elevated temperature in a random spin configuration, a typical superparamagnetic system.

Superferromagnetism can be realized using circular magnetic nanodisks on a triangular lattice. The dipolar interactions will then seek to align all magnetic moments in the same direction, as

seen in Figure 2.9b. Such a system can have a relative large net magnetization, since there are no domains and domain walls.

Ising type nanomagnets placed on a square lattice with their easy axes aligned will prefer super-antiferromagnetic ordering. The dipole fields responsible for this ordering is analogous to the Weiss fields responsible for antiferromagnetic ordering in Eq. (2.14). Ising ASI exhibit super-antiferromagnetism below a critical temperature. The dipolar neighbor interactions will align antiparallely as illustrated in Figure 2.9c. Above the critical temperature on the other hand, thermal fluctuations will dominate and the system will be superparamagnetic. Using Weiss theory for antiferromagnetism, we expect the magnetic susceptibility for Ising ASI to follow a Curie-Weiss law similar to that for antiferromagnetic materials given in Eq. (2.15). The Curie constant and critical temperature is unique for the specific ASI and should not be mixed with the corresponding values for the material used to fabricate the nanomagnets.

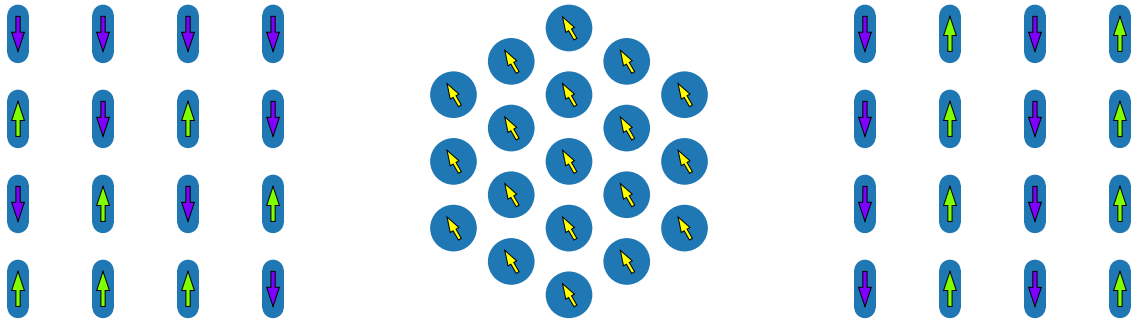

(a) (b) (c)

Figure 2.9: Examples of supermagnetic ordering. (a) Ising ASI above a critical temperature exhibits superparamagnetism, illustrated with a random spin configuration. (b) Circular disks on a triangluar lattice exhibits superferromagnetism, and (c) Ising ASI below a critical temperature prefers superantiferromagnetic ordering.

2.3.3 Artificial spin ice as point dipoles

The dipole model introduced in Section 2.1 is a powerful tool when investigating the dynamics of ASIs using computational tools. By considering each nanomagnet as a point dipole instead of considering individual atomic magnetic moments, computational efficiency can be improved by several orders of magnitude, allowing us to work with larger ASI systems. Another benefit with the dipole model is that it is intuitive and easy to understand. This model can only be employed for single domain ferromagnets with the elongated shape anisotropy, giving a binary magnetic moment and the characteristic square-like hysteresis curve seen in Figure 2.7.

The point dipole model is of course a great simplification of the physics that take place in ASI. Internal magnetic structures within the macrospins and the possible existence of more than two magnetic poles can for instance not be predicted or accounted for using the point dipole model [35]. This is in contrast to micromagnetic modelling, which can predict internal magnetic structure in a nanomagnet at the expense of computational efficiency.

According to the point dipole model, the total magnetic field $\mathbf{H}_i$ affecting magnet i in an ASI is the sum of the dipolar magnetic fields set up by neighboring nanomagnets, as well as any

external magnetic field [2]

$$\mathbf{H}_i = \mathbf{H}_{\text{ext}} + \sum_j \mathbf{H}_j. \tag{2.18}$$

Nearest neighbor and next-nearest neighbor interactions dominate, since the dipolar field strength scales with r^{-3}. If the magnetic field acting on magnet i projected on its easy axis is in the opposite direction and exceeds the coercive field, the magnet will flip its magnetization.

An ASI at $T = 0\,\text{K}$ will be in a frozen state, meaning that the spin configuration will not change without an external magnetic field. At very high temperatures on the other hand, we expect the macrospins to flip completely random due to large thermal fluctuations. Somewhere in between, magnetic fields and thermal energy will be balanced and both affect the spin configuration of the system. Jensen *et al.* incorporated the effect of thermal fluctuations by assigning an effective random "thermal field" to every nanomagnet [2],

$$H_{\text{th}} = \frac{E_{\text{th}}}{M}, \tag{2.19}$$

where $E_{\text{th}} \sim k_{\text{B}}T$ and M is the macrospin magnetic moment. The thermal field is added to the total magnetic field in Eq. (2.18).

Switching of macrospins is the fundamental mechanism that change the spin configuration and dipolar energy landscape in ASI. The Stoner-Wohlfart model describes the magnetization of elliptical single domain ferromagnets which change their macrospin state by coherent rotation instead of domain wall motion [36]. The model defines "switching criteria", i.e., for which external magnetic fields a macrospin will flip its magnetization direction. Jensen *et al.* suggested a modified version of the Stoner-Wohlfart switching criteria to account for non-elliptical nanomagnets [2]:

$$\left(\frac{H_{\parallel}}{bH_c}\right)^{2/\gamma} + \left(\frac{H_{\perp}}{cH_c}\right)^{2/\beta} = 1. \tag{2.20}$$

Here, $H_{\parallel}$ and $H_{\perp}$ are the external magnetic field components parallel and normal to the easy axis, respectively, and H_c is the coercive field. Eq. (2.20) describes a "switching astroid" where a flip in magnetization will occur when the left hand side is greater than 1, corresponding to a point outside the astroid. The parameters b and c define the height and width of the astroid, respectively, while β and γ describe the curvature of the astroid. Jensen *et al.* used micromagnetic simulations to find values for these parameters corresponding to customized nanomagnet shapes. The original Stoner-Wohlfart astroid and the modified version based on Eq. (2.20) is plotted in Figure 2.10.

The point dipole model with the Stoner-Wohlfart switching criteria is employed to simulate ASI dynamics in flatspin, a novel large-scale ASI simulator [2]. This simulator will be used to simulate the dynamics of ASIs in Chapter 3.

Micromagnetic modelling can also be used to numerically investigate dynamics in magnetic materials. It is a much more general and computationally expensive method compared to the point dipole model, and struggle already for ASIs with more than 25 macrospins. Micromagnetic modelling can also be used to complement the point dipole model, such as obtaining values for the parameters in Eq. (2.20) [2]. These types of magnetic simulations are powerful tools in magnetic studies, but are outside of the scope of this work and will not be discussed further.

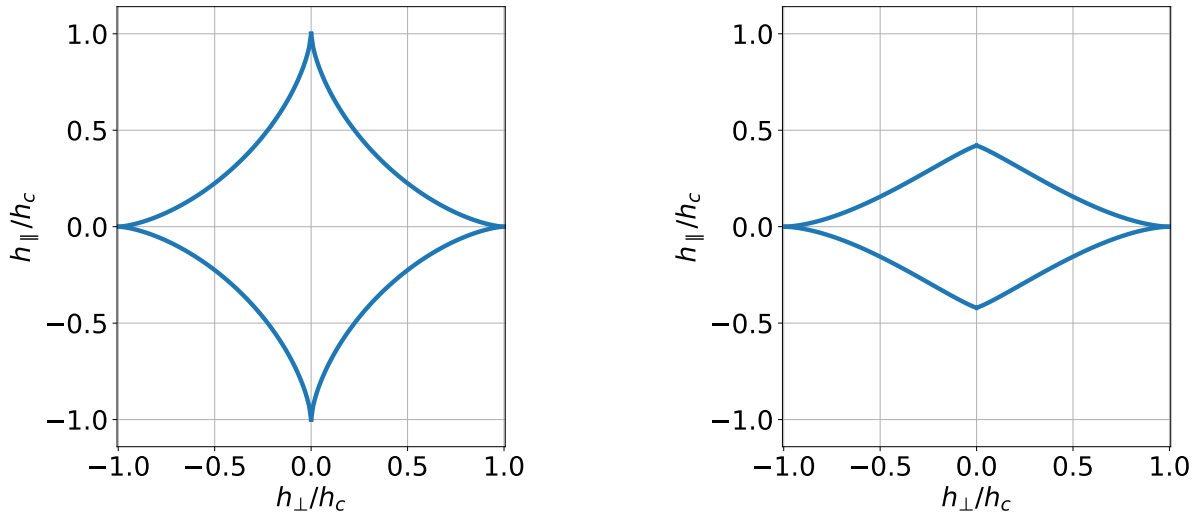

(a) (b)

Figure 2.10: The Stoner-Wohlfart swithing criteria. (a) elliptical nanomagnets and (b) a rectangular nanomagnet with rounded corners. The plots are adapted from Figure 2 in Jensen *et al.* [2], based on switching parameters they had calculated using micromagnetic simulations.

2.4 Spatial correlation function

Space and time coherence in a system are measaures of order and can typically be quantified using correlation functions. The spatial (constant time) correlation function is a measure of spatial order and describes how likely it is that a quantity co-vary over a distance $\mathbf{r}$ in a system. For example, the spin-spin spatial correlation function, $C(\mathbf{r})$, describes how the spin configuration at position $\mathbf{r}_0$ correlates with the spin configuration at position $\mathbf{r}_0 + \mathbf{r}$,

$$C(\mathbf{r}, t) = \langle S(\mathbf{r}_0, t) S(\mathbf{r}_0 + \mathbf{r}, t) \rangle, \tag{2.21}$$

where $S(\mathbf{r}, t) \in \{-1, +1\}$ describes the spin at position $\mathbf{r}$ at time t [37]. The spin-spin correlation value $C_{ij} = S_i S_j$ between two macrospins i and j are defined as $+1$ for the configuration that minimizes the dipole energy and -1 for the configuration that maximizes it:

$$C_{ij} = \begin{cases} +1 & \text{if } E_{\text{z,dip}} < 0, \\ -1 & \text{if } E_{\text{z,dip}} > 0. \end{cases} \tag{2.22}$$

$E_{\text{z,dip}}$ refers to the magnetic potential energy between two magnetic dipoles, defined in Eq. (2.3). The spatial correlation function will be important in the magnetic analysis of simulated ASIs in Chapter 3. Here, we investigate the function with some basic examples.

Consider a two-dimensional Ising model consisting of *ferromagnetic* spins arranged on a square lattice where the spins only can point either up or down. This system differs from an Ising ASI (Figure 2.8c) since the dipolar magnetic field favor antiparallel alignment in the direction perpendicular to the magnetization. The self-correlation, $C(\mathbf{0})$, is always 1. Exchange interactions between neighboring spins will favor parallel alignment, hence we expect it to be more likely that they are correlated ($C = +1$) than anticorrelated ($C = -1$), even at relatively high temperatures. Below a critical temperature, T_{C}, this preference extends to further neighbors, giving what we call long-range magnetic ordering. In a ferromagnetic system exhibiting long-range order, we can expect distant spins to have their magnetic moments aligned, although the two

spins do not interact directly. Above T_C, the correlation function will go from 1 at $\mathbf{r} = \mathbf{0}$ to 0 for large $|\mathbf{r}|$. For some systems, we might only care about the euclidian distance, $r = |\mathbf{r}|$. The two-dimensional correlation function can then be compacted into one dimension by averaging values with equal r,

$$C_{\text{avg}}(r) = \frac{1}{N_{\text{pair}}^{(r)}} \sum_{|\mathbf{r}_{ij}|=r} C(\mathbf{r}_{ij}), \tag{2.23}$$

where $N_{\text{pair}}^{(r)}$ is the number of nanomagnet pairs satisfying $|\mathbf{r}_{ij}| = r$. The correlation length, ζ, is defined to be the length such that

$$C(\zeta) = \frac{1}{\mathrm{e}}. \tag{2.24}$$

Saccone *et al.* used correlation functions in their analysis of Ising ASIs [3]. The Ising ASI exhibits superantiferromagnetism, since the magnetic dipole moments favor antiparallel alignment in the direction normal to the easy axes. The spatial correlation function would therefore oscillate between -1 and $+1$ when moving along $r_\perp$, the direction normal to the easy axis, and remain constantly $+1$ when moving in the longitudinal direction, as illustrated in Figure 2.11. If the one-dimensional correlation function $C_{\text{avg}}(r)$ was created directly like in Eq. (2.23), it would for example yield zero for $r = 1a$ for the *perfectly ordered* Ising ASI. The lattice spacing, a, is here the nearest neighbor distance in the Ising ASI. When measuring order, anticorrelation can be just as "ordered" as correlation. The correlation function for the Ising ASI is therefore found by taking the absolute value $C'(\mathbf{r}) = |C(\mathbf{r})|$ and using $C'(r)$ instead of $C(r)$ in Eq. (2.23).

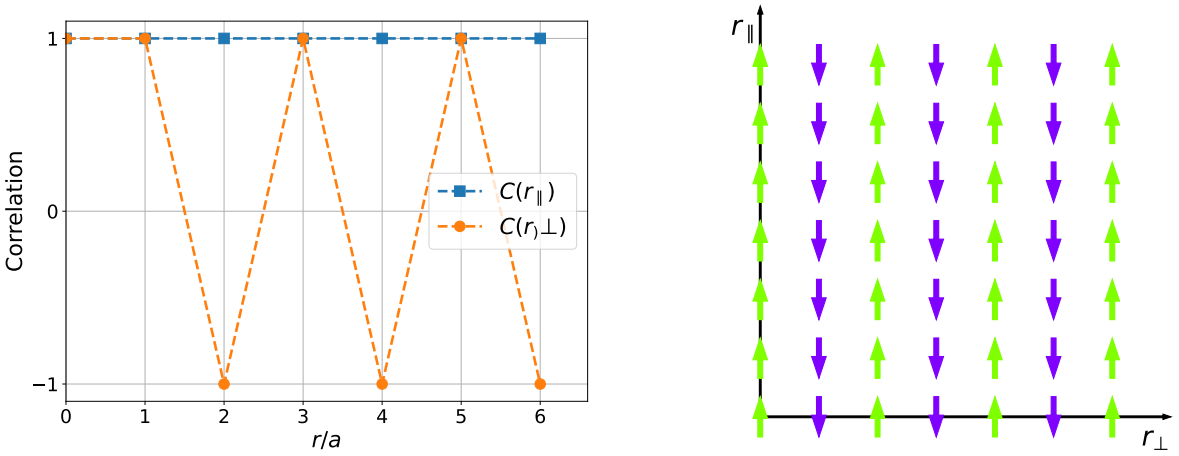

(a) (b)

Figure 2.11: The correlation function for the Ising ASI in its ground state spin configuration. (a) Show how the correlation function oscillate between $+1$ and -1 along $r_\perp$ and remain constant $+1$ along $r_\parallel$. (b) show how these directions are defined. In order to avoid having for example $C(2) = 0$, $C'(r)$ must be used when compacting the correlation function into one dimension.

2.5 Analysis of magnetic ordering in ASI with statistical mechanics

The correlation function contains more information about a system than just a system's spin correlation length. Saccone *et al.* characterized magnetic phases in different ASIs based on the spatial spin-spin correlation function. The fundamental ingredients in this approach are the Curie-Weiss law, the fluctuation-dissipation theorem (FDT) and a power law describing the correlation length near phase transitions.

Curie-Weiss law was introduced in Section 2.2.2, whereas the FDT and the correlation length power law are described next. They are all important building blocks in the magnetic analysis of ASIs in Chapter 3.

2.5.1 Fluctuation-dissipation theorem

The generalized Hamiltonian for an artificial spin system can be split into two parts,

$$\mathcal{H} = \mathcal{H}_0 - \sum_i \mathbf{H}_{\text{ext}} \cdot \mathbf{m}_i, \tag{2.25}$$

where $\mathcal{H}_0$ covers spin-spin interactions in the system and is independent of any external magnetic field, $\mathbf{H}_{\text{ext}}$. The sum goes over all spins in the system. Using thermodynamic analysis and Boltzmann statistics, it can be shown that the magnetic susceptibility can be expressed in terms of temperature and the correlation function as [38]

$$\chi(T) = \frac{m^2}{k_{\text{B}}T} \sum_{ij} C(\mathbf{r}_{ij}). \tag{2.26}$$

The sum on the right hand side vanishes for large $\mathbf{r}_{ij}$, since distant spins are less likely to be correlated and will average to zero. The above result is a consequence of the fluctuation-dissipation theorem [37].

Eq. (2.26) and the Curie-Weiss law in Eq. (2.11) give two expressions for the magnetic susceptibility in a system of interacting, localized magnetic moments. The inverse relation between susceptibility and temperature is present in both of them, and will be used to estimate the critical temperature for simulated ASIs.

2.5.2 Correlation lengths near phase transitions

Below the critical temperature, T_{C}, we expect a system with strong nearest neighbor interactions to establish long-range order, such as superantiferromagnetism for the Ising ASI. Above T_{C} on the other hand we expect superparamagnetic behavior, where the correlation function quickly goes to zero for $r > 0$. A second order continous phase transition takes place around T_{C}, where the correlation length diverges, following a power law decay as the temperature increases above T_{C} [3]

$$\zeta(T) = A\Big(\Big|\frac{T - T_{\text{C}}}{T_{\text{C}}}\Big|\Big)^{-\nu}. \tag{2.27}$$

Here, A is a prefactor and ν is known as a critical exponent. Numerical values exist in the literature for most known phase transitions. For the two-dimentional Ising model, the transition

between the ordered and disordered phase is characterized by $\nu_{\text{Ising,2D}} = 1$ (exact analytical solution). The critical exponent for a spin glass system is $\nu_{\text{SG}} = 3.559 \pm 0.025$ [3].

Saccone *et al.* calculated the critical exponent of experimentally realized ASIs and compared them with theoretical values from the literature to evaluate if they had found candidate systems exhibiting spin glass phase. The critical exponents they found for these ASIs were $\nu = 1.38 \pm 0.62$ and $\nu = 1.82 \pm 0.99$. These values are significantly lower than the calculated value, thus concluding they had not fabricated ASIs with spin glass behavior.

2.6 Evolutionary algorithms for ASI generation

One of the main challenges towards the realization of exotic ASIs is to come up with ASI geometries that are not limited by our imagination. Penty *et al.* present a novel way of representing ASIs and use evolutionary algorithms to search for ASI designs that exhibit a desired computational or meta-material property [10].

Evolutionary algorithms are based on the idea that we can simulate certain characteristics of evolution in nature. They can be effective in the search for new ASI designs in the large space of possible designs, in particular because the relations between a design and the computational or supermagnetic properties are complex and mostly unknown. Concepts analogous to genes, generations, mutations and crossover are used to search for a global maximum of a given fitness parameter [39]. Analogous to how living cells evolve in nature, the tunable parameters in a search space are called "genes" and the desired parameter we are optimizing are referred to as "fitness". Mutations and crossover ensure diversity among the individuals in a population.

Representation can be at least as important as the algorithm when solving optimization problems. Penty *et al.* represented ASIs using a set of tiles, each consisting of exactly two magnets [10]. The tiles were used to generate large ASIs by starting with one "origin magnet" and iteratively applying the tiles such that one of the magnets in a tile overlap with an existing magnet, and a new magnet was placed where the other magnet in the tile ended up. A more thorough explanation of the algorithm can be found in the original paper. Each tile in the set of tiles that represent one ASI can be thought of as a "gene" of this particular ASI. The genes can be mutated smoothly by for example changing the rotation or position of one of the magnets in a tile. Crossover can for example be the process of combining tiles from two "parent" ASIs into a set of tiles representing a new ASI individual.

The fitness function is a key ingredient in evolutionary algorithms. Analogous to the principle of "survival of the fittest" in nature, the fitness function discriminates between individuals in a population based on a desired property. Combined with the flatspin simulator, we can define the fitness function for ASIs based on computational or supermagnetic properties. Penty *et al.* demonstrated their method using a minimum flips fitness function that seeks to minimize the flipping of magnetic moments under the influence of an oscillating external magnetic field. In this work, we will try to establish a fitness function based on supermagnetic properties such as the critical temperature, T_{C}, or the critical exponent, ν.

Chapter 3

Experimental

This chapter describes the steps of simulating ASIs and analyzing magnetic ordering in systems following those simulations. The steps are divided into 5 different parts.

First, the method of generating ASI models is described in Section 3.1. This is straight forward for conventional ASIs based on a fixed lattice, such as the square and Ising ASIs. For ASI designs with geometric disorder, we describe the rules followed when generating the designs, as well as the notation that is used to refer to them.

The annealing protocols and simulation parameters used to run simulations are presented in Section 3.2. We also describe the procedure of running the simulations and practical considerations that must be taken.

A generalized correlation function is suggested in Section 3.3 together with the intuition behind it. The steps carried out for calibration of a set of discretization parameters and subsequent testing are also described.

The complete analysis of simulated ASI models is conducted in Section 3.4. Based on the suggested correlation function and tools from thermodynamics and statistical mechanics, we characterize ASI models in terms of critical temperatures, order parameters and magnetic phases.

Finally, in Section 3.5 we use the analysis for calculating the critical temperature as a fitness function in evolutionary algorithms and try to generate exotic ASI designs far beyond the "imagination of the designer".

3.1 ASI test designs

Six different types of ASIs are used in simulations and development of characterization methods in this work. Square, pinwheel and Ising ASIs are well described in literature from both an experimental and theoretical perspective [7]. The high degree of order and symmetry found in these "textbook systems" are broken in three modified systems: diluted square (DS), disordered Ising (DI) and rotated disordered Ising (RDI). See Figure 3.1 for an overview of all 6 designs. The colors of the macrospin arrows correspond to their element-wise rotation and are used to better visualize magnetic ordering. A HSV (hue, saturation, value) colormap is used to map the macrospin rotation to a color, illustrated for 8 different rotations in Figure 3.2.

The Ising model was already described in Chapter 2, and is illustrated in Figure 3.1c in its "ground state", i.e., the spin configuration that minimizes the total magnetic energy in the system. Ising ASI favors antiparallel alignment, exhibiting superantiferromagnetic order.

The square ASI can be thought of as two interpenetrating Ising models, rotated 90° with respect

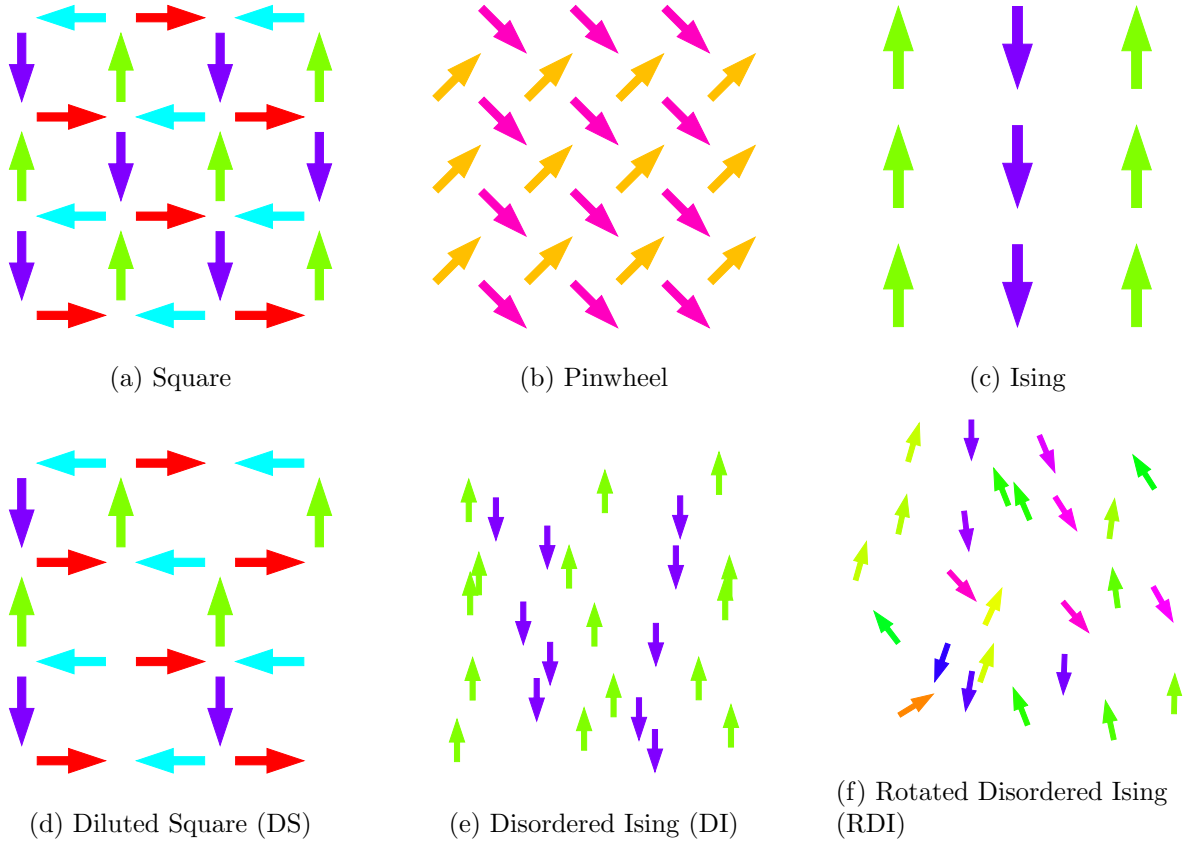

(a) Square (b) Pinwheel (c) Ising

(d) Diluted Square (DS) (e) Disordered Ising (DI) (f) Rotated Disordered Ising (RDI)

Figure 3.1: The six ASI designs that are used to test the analysis of magnetic ordering in Section 3.4. (a) Square, (b) pinwheel and (c) Ising are illustrated in their ground state spin configurations. The systems with less order and periodicity do not have the same well defined ground state. They are (d) diluted square (DS), (e) disordered Ising (DI) and (f) rotated disordered Ising (RDI). The color of the arrows correspond to the direction of the macrospin as defined in Figure 3.2.

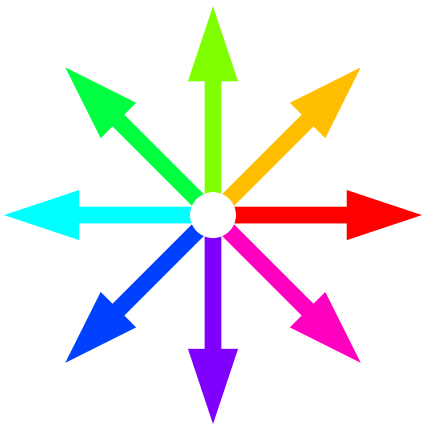

Figure 3.2: The direction of a macrospin is visualized using the HSV colormap, here illustrated for 8 different directions.

to each other, as seen in Figure 3.1a. The spin configuration that minimizes its dipole energy is when every square cell on the lattice enclosed by 4 macrospins exhibit flux closure with

alternating directions, as they do in Figure 3.1a.

The DS system is created from a square ASI by picking at random a fraction *df* of the islands and removing them. The removal of macrospins introduces "defects" in the system and changes the dipolar energy landscape. The dilution fraction is kept at $df = 0.20$ throughout this work, which is high enough so that we expect significantly different results compared to the square ASI. The ground states for a diluted square ASI can be deduced from the "parent" square ASI, and dilution often lead to degenerate states. That can be when a vertex consists only of 3 macrospins, and the total dipole energy is the same regardless of the direction of one or more of the macrospins at that vertex.

The DI and RDI systems are generated from Ising ASIs by introducing separate Gaussian disorder on the x- and y-coordinates with mean zero and standard deviation σ_x and σ_y, respectively. The standard deviation is given as a fraction of the lattice constant, a. The disorder is drawn separately for every nanomagnet. Similarly, the RDI systems has element-wise rotation introduced by independently picking angles from a Gaussian distribution with mean zero and standard deviation σ_ϕ.

The disordered systems are referred to on the form $\mathrm{DI}_{\sigma_x,\sigma_y}$ and $\mathrm{RDI}^{\sigma_\phi}_{\sigma_x,\sigma_y}$. For example, $\mathrm{RDI}^{45}_{0.1,0.0}$ refers to a system which has introduced Gaussian disorder with standard deviation $\sigma_x = 0.1a$ on the x-coordinate and $\sigma_\phi = 45°$ on the element-wise rotation. The y-coordinates have not been changed from those in the Ising ASI. This way of introducing geometric disorder from Ising ASIs resembles the method described by Saccone *et al.* [3]. It allows us to start from the familiar Ising ASI and gradually introduce geometric disorder to discover any trends or abrupt transitions caused by the geometric disorder.

The ASI fabrication process was described briefly in Section 2.3.1. We want to keep the simulated systems physically realizable, thus restricting how close two islands can be placed without introducing defects during the fabrication process. When introducing the spatial disorder, no islands are allowed to be placed such that the shortest distance between neighboring islands is less than 5% of the lattice spacing. This corresponds to approximately 20 nm for typical lattice spacings. If the suggested disorder on magnet i, $\Delta_{x,i}$, $\Delta_{y,i}$ and $\Delta_{\phi,i}$, found by drawing values from the Gaussian distributions described above, leads to a violation of the shortest distance restriction, the disorder is discarded and new values are picked at random.

It is not trivial to identify the ground states for the disordered systems. With low degrees of geometric disorder, we can expect behavior similar to that of the Ising ASI. As disorder is increased, especially on the element-wise rotation, it is not intuitive to identify the ground states—if they exist.

3.2 ASI simulations in flatspin

All ASI simulations are carried out using flatspin, a novel large-scale ASI simulator developed at NTNU by Jensen *et al.* [2]. This section gives a brief overview of how flatspin works, before proceeding to describe how the simulator is configured in our simulations.

3.2.1 flatspin working principles

More in-depth explanations as well as validation of the simulator can be found in the original paper by Jensen *et al.* [2].

flatspin is based on the magnetic point dipole model with the Stoner-Wohlfart switching criteria described in Section 2.3.3. For every simulation step, flatspin calculates the total magnetic field

at every macrospin location as

$$\mathbf{H}_{\mathrm{tot},i} = \mathbf{H}_{\mathrm{ext}} + \sum_j \mathbf{H}_{ij} + \mathbf{H}_{\mathrm{th},i}, \tag{3.1}$$

where $\mathbf{H}_{\mathrm{ext}}$ is an external magnetic field (always zero in this work), $\mathbf{H}_{ij}$ is the dipolar magnetic field from macrospin j at the location of macrospin i and $\mathbf{H}_{\mathrm{th},i}$ is the "thermal field" on macrospin i with magnitude calculated using Eq. (2.19).

The macrospin where $\mathbf{H}_{\mathrm{tot},i}$ is the furthest outside the Stoner-Wohlfart switching astroid in Figure 2.10 and the projection onto the easy axis is oppositely directed, is flipped. This process is repeated until there are no more flippable spins. The thermal fields are then updated by drawing a new set from the same distribution, before running a new relaxation process. One relaxation process corresponds to one timestep.

The thermal fields in flatspin are drawn from a Gaussian distribution with mean zero and standard deviation σ_{th}. The standard deviation can either be set directly, or by using the following expression:

$$\sigma_{\mathrm{th}} = \sqrt{\frac{2}{\pi}} \frac{k_{\mathrm{B}}T}{M_{\mathrm{sat}}V} \ln\left(f_0 \Delta t\right). \tag{3.2}$$

Here, f_0 is known as the attempt frequency and Δt the experimental time scale. Eq. (3.2) will be used to set σ_{th} throughout this work.

The traditional approach of simulating ASIs is based on micromagnetic simulations [2]. This approach is computationally expensive compared to flatspin, and can quickly become unpractical for ASIs larger than 5×5 macrospins. Through GPU acceleration, ASI systems of millions of magnets can be simulated in flatspin.

flatspin has proven to be a powerful tool, able to reproduce several types of behavior seen in experimentally realized ASIs, such as superparamagnetism and superferromagnetism [2]. A remaining challenge is however correct modelling of temperature and thermal energy.

In the current implementation, it is not expected that the temperature used in flatspin is directly transferable to the laboratory. Throughout this work, we will nevertheless keep referring to all temperatures in the unit of Kelvin. It is therefore *not* expected that exact temperature values found for example for critical temperature will be the true critical temperatures in a laboratory system. Trends and dynamics as the temperature is increased or lowered, on the other hand, are expected to reflect physical behavior.

3.2.2 Simulation runs

Simulations are run using flatspin's command line interface with computational resources provided by the NTNU IDUN/EPIC computing cluster [40]. Distributed runs on GPU nodes allow larger system sizes compared to running the simulations on a regular computer. The `IsingSpinIce`, `SquareSpinIceClosed` and `PinwheelSpinIceDiamond` models provided by flatspin are used for the Ising, square and pinwheel ASIs, respectively. The DI, RDI and DS designs are created by specifying the position and element rotation of each individual nanomagnet using the `CustomSpinIce` model in flatspin. These flatspin models contain information about the ASI geometric design and simulation parameters such as nanomagnet properties and simulator settings.

The Ising, DI and RDI ASIs are simulated using a system size of 50×50, corresponding to 2500 macrospins. The system size of the square and pinwheel ASIs, which have a higher macrospin

density, is 35×35, corresponding to $2 \cdot 35 \cdot 36 = 2520$ macrospins. The DS ASI, constructed from the square ASI by removing 20 % of the magnets, has 2016 macrospins. These system sizes provide convenient tradeoffs between computational complexity and boundary effects which are not desired in this work.

flatspin offers a wide range of tunable simulation parameters, such as the switching parameters in Eq. (2.20) and the thermal field parameters in Eq. (3.2). Finding good values for all simulator parameters is an important and often challenging part of running any simulation. The flatspin parameters are set with the goal of simulating systems that can be physically realized in a laboratory. A summary of all flatspin simulation parameters is given in Table 3.1, with a comment on how it was calculated or a reference to literature from where it was obtained in the rightmost column.

All flatspin simulations are carried out with no external magnetic field. Thermal energy and magnetic dipole interactions are thus the only driving forces behind ASI dynamics. Every macrospin is randomly initialized, giving an initial spin configuration similar to what we would expect for an ASI annealed at a temperature far above the critical temperature. For every simulation run, the system is annealed to an elevated temperature, T_{start}, and gradually cooled to a final temperature, T_{end}. It is then kept constant at T_{end} for the final 25 % of the simulated timesteps. The temperature profile is given by

$$T = \begin{cases} T_{\text{start}} \left(\frac{T_{\text{end}}}{T_{\text{start}}} \right)^{\left(\frac{t}{0.75 \cdot t_{\max}} \right)^{\tau}} & \text{if } 0.00 \leq t/t_{\max} < 0.75, \\ T_{\text{end}} & \text{if } 0.75 \leq t/t_{\max} < 1.00, \end{cases} \tag{3.3}$$

where t is the time such that $t/t_{\max}$ goes from 0 to 1. τ is an exponent that defines how fast the system is cooled. Low values of τ give a temperature profile that quickly decreases towards T_{end}, while high values for τ leave the temperature high for a longer period before dropping.

The temperature profile for 3 different values of τ can be seen in Figure 3.3. $\tau = 1.5$ (orange line) is used for all simulations in this work since it gives a temperature profile where the system never gets cooled too quickly. This allows the system to relax throughout the full simulation and not suddenly freeze because of abrupt temperature changes. The annealing temperatures were chosen such that thermally induced random flips dominate the spin configuration at that temperature (superparamagnetism), and gradual cooling allow the systems to relax towards a low energy state as thermal energy become less dominant.

All simulations are carried out over 10 000 timesteps, allowing sufficient time to relax the systems as the temperature is lowered. If the temperature is lowered too quickly, the system will freeze in a higher energy configuration. The total dipole energy of the system is monitored for every run to verify that no sudden freezing occur. As the system is relaxed, the total dipole energy of the system will fluctuate and gradually decrease. A sudden stop in fluctuations indicates a system that has frozen abruptly.

Simulation runs used to calculate magnetic ordering are repeated 10 times with the same configuration, but a new random seed, in order to produce a thermal average.

Table 3.1: Overview of flatspin simulator configuration parameters.

Parameter	Value	Comment
Time related		
`spp`	100	Number of sampled timesteps per period.
`periods`	1	Not relevant without external magnetic fields.
`timesteps`	10 000	Sufficiently many to allow time for relaxation over most temperature profiles.
Temperature related		
`temp-func`	`'exp-decay'`	The temperature profile is calculated according to Eq. (3.3).
`set_temp_method`	`'set_temp'`	The standard deviation of the thermal fields is set using Eq. (3.2).
Switching astroid		
`sw_b`	0.41	Used by Jensen *et al.*, calculated using micromagnetic simulations [2].
`sw_c`	1.00	Jensen *et al.* [2].
`sw_beta`	2.0	Jensen *et al.* [2].
`sw_gamma`	4.0	Jensen *et al.* [2].
Magnetic properties		
`hc`	0.20	Jensen *et al.* [2].
`disorder`	0.05	Jensen *et al.* [2].
`msat`	860×10^3	Jensen *et al.* [2].
`volume`	5.87×10^{-24}	Nucleation volume, 3.3 % of a cube with dimensions 10 nm × 80 nm × 220 nm. See Section 2.3.2.
`alpha`	0.0187	$\alpha = \frac{\mu_0 M_{\text{sat}} V}{4\pi a^3}$ [2]. Using $a = 30$ nm. Set after trial-and-error. The lattice spacing a used to calculate α is lower than for a typical system that can be fabricated. Lower values of α gave negligible dipolar interactions, and the value was set such that dipole energies were same order of magnitude as thermal energies.
Simulator settings		
`neighbor_distance`	10	Nearest neighbor interactions are most important. Reduced from `inf` to 10 did not affect the simulator performance.
`init`	`'random'`	Random initial spin configuration.
Geometry		
`lattice_spacing`	1	Already incorporated into the coupling constant, `alpha`.

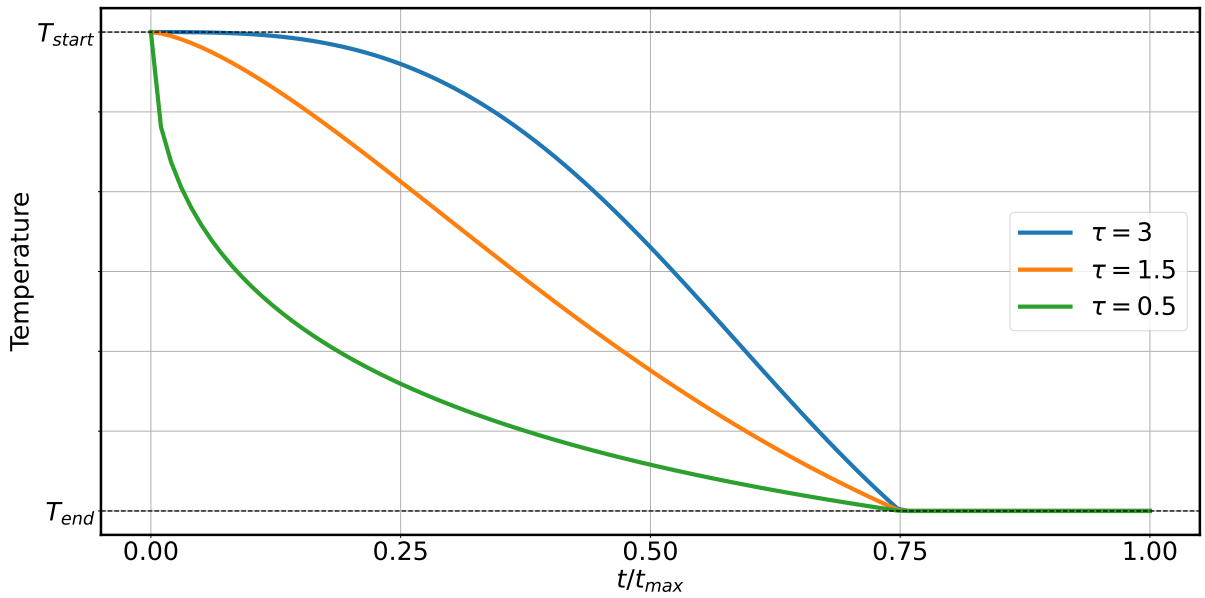

Figure 3.3: Temperature profile used for thermal annealing protocols in flatspin, as defined by Eq. (3.3). The system is exponentially cooled down from T_{start} to T_{end} during the first 75% of the time (7500 timesteps), and kept constant at T_{end} over the final 2500 timesteps. Plotted for three different decay constants. $\tau = 1.5$ was used in all simulations.

3.3 Spatial spin-spin correlation function

The spatial spin-spin correlation function is an essential building block in the analysis of magnetic ordering in Section 3.4. This section describes and compares two different spatial spin-spin correlation functions. First, we highlight why the cartesian correlation function used by Saccone *et al.* is not able to generalize to all ASI geometries. We proceed by suggesting a "polar" correlation function and go through steps to show how it performs on ASIs in different spin configurations.

3.3.1 Cartesian correlation function

Saccone *et al.* quantified magnetic ordering in their fabricated ASIs as a function of relative cartesian separation [3]. The correlation value for two nanomagnets i and j separated by a distance $\mathbf{r}_{ij} = x\hat{\mathbf{x}} + y\hat{\mathbf{y}}$ formed the spatial correlation function

$$C(\mathbf{r}_{ij}) = \langle S_i S_j \rangle_T. \tag{3.4}$$

Since we want to have $C(\mathbf{r}_{ij}) = C(\mathbf{r}_{ji})$, the separation vectors $\mathbf{r}_{ij}$ and $-\mathbf{r}_{ij}$ are considered equivalent when constructing the correlation function. The neighborhood space, i.e., the space around magnet i containing its neighbors, is discretized into bins, illustrated in Figure 3.4 for a small 3×3 Ising ASI. The bins that have equal colors correspond to equivalent separation vectors with respect to the center magnet, i. The one-dimensional correlation function is formed according to Eq. (2.23) by averaging all $C(\mathbf{r}_{ij})$ where $r - \Delta r/2 < |\mathbf{r}_{ij}| < r - \Delta r/2$ and Δr is the resolution of the correlation function.

The nanomagnet neighborhood space discretization and corresponding correlation function used by Saccone *et al.* works well for the Ising ASI. The 3×3 Ising ASI in Figure 3.4a is in its ground state, and for equivalent bins, all spins are either correlated ($C_{ij} = +1$) or anticorrelated

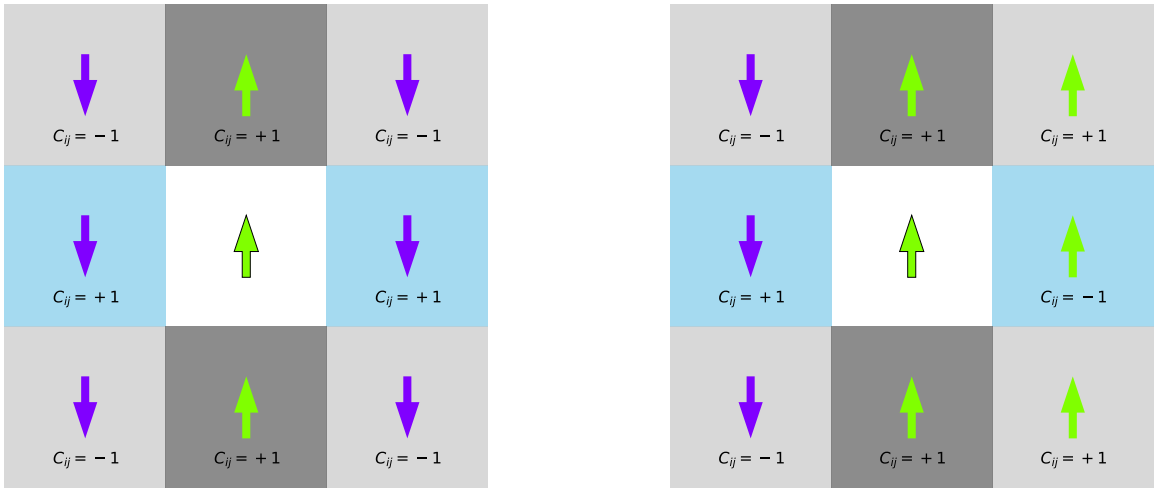

(a) (b)

Figure 3.4: The cartiesian correlation function for a 3×3 Ising ASI in (a) the ground state and (b) in a spin configuration where the macrospins in the rightmost column are flipped. Equally colored bins correspond to equivalent $\mathbf{r}_{ij}$, whose correlation values are averaged when computing the correlation function. In the ground state, $C(\mathbf{r}) = 1$ for all $\mathbf{r}$. In the excited state, the three flipped macrospins to the right give zero correlation for $\mathbf{r} = \hat{\mathbf{x}}$ and $\mathbf{r} = \hat{\mathbf{x}} + \hat{\mathbf{y}}$, found by averaging the values in the blue bins and the light gray bins.

($C_{ij} = -1$) with the center spin. Since anticorrelation can be just as ordered as correlation, we use the absolute value of $C(\mathbf{r})$ when compacting it into one dimension, as described in Section 2.4.

The rightmost column of macrospins are flipped in Figure 3.4b and the system is no longer in its ground state spin configuration. When computing the average correlation value per bin, one can see from the correlation values given in the figure that the blue and light gray bins will sum to zero, thus giving zero correlation for $\mathbf{r} = \hat{\mathbf{x}}$ and $\mathbf{r} = \hat{\mathbf{x}} + \hat{\mathbf{y}}$.

The one-dimensional correlation function for a larger Ising ASI in its ground state is plotted in Figure 3.5. We see how the ground state is characterized by perfect correlation, as expected for a correlation function that is able to capture this type of ordering.

Figure 3.5 also includes the one-dimensional correlation function applied to a square ASI in its ground state. The low correlation values highlight a challenge with the method: it does not generalize well for designs where the nanomagnets are not parallel.

The origin of the challenge with the square ASI comes from the fact that different neighbor pairs separated by the same vector $\mathbf{r}_{ij}$, can have a correlation value of both $+1$ and -1 in the ground state. The green and red pairs in Figure 3.6 are both separated by $\mathbf{r}_{ij} = 1\hat{\mathbf{x}}$, but have correlation values $+1$ and -1 respectively. These cancel each other out when averaging, as seen for $C(r = 1)$ in Figure 3.5, resulting in a presumebly uncorrelated system.

We need a different correlation function than the one used by Saccone *et al.* if we want to capture order in ASIs with less restrictive designs than the Ising ASI.

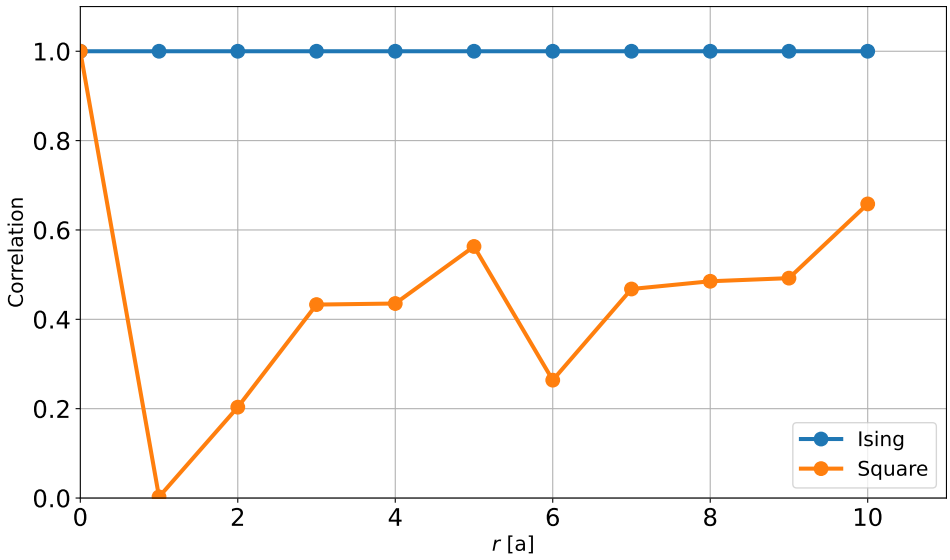

Figure 3.5: The one-dimensional correlation functions for the Ising and square ASIs in their respective ground states using the cartesian correlation function suggested by Saccone *et al.* It captures perfect correlation for the Ising ASI, but fails to do the same for the square ASI.

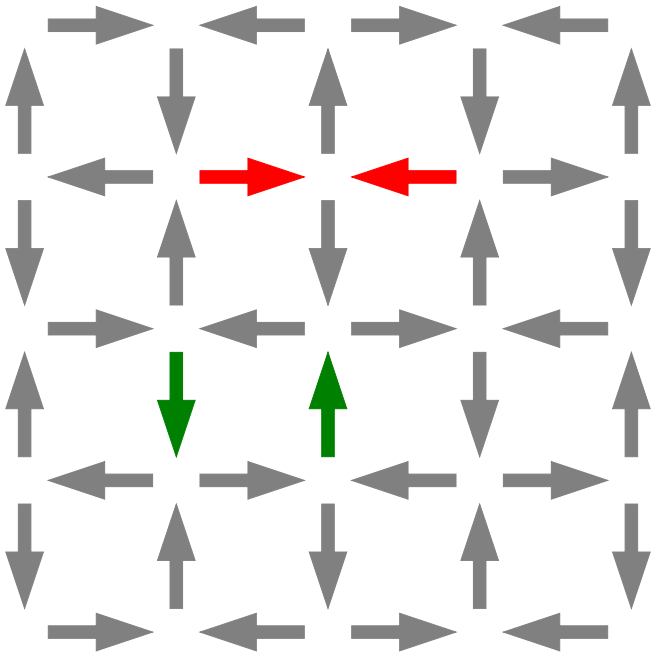

Figure 3.6: The green and red macrospins pairs have $C_{ij} = +1$ and $C_{ij} = -1$, respectively. They cancel each other out when averaging the correlation function, since both have a relative separation of $\mathbf{r}_{ij} = 1\hat{\mathbf{x}}$. The correlation function predicts zero correlation for $\mathbf{r}_{ij} = 1\hat{\mathbf{x}}$, despite the square ASI being in its perfectly ordered ground state.

3.3.2 Polar correlation function

Here, we propose a modified version of the spatial spin-spin correlation function. The fundamental idea is generalization and independence from any lattice geometry. Intuitively, the two most

decisive parameters affecting the interaction between the magnetic moments in a nanomagnet pair are the euclidian separation distance, r, and their position with respect to each others' easy axes. By parameterizing the space around every magnet using r and the polar angle with respect to the easy axis, θ, we can construct a polar correlation function (PCF).

Figure 3.7a illustrates how the two parameters, r and θ, are defined for a nanomagnet pair with arbitrary position and rotation. Note that the neighbor magnet (dark blue in the figure) can have any rotation around its center, without affecting the values of r or θ. This is potentially a weakness, and a possible extension of the PCF could include a third parameter to describe the relative orientation between the two magnets.

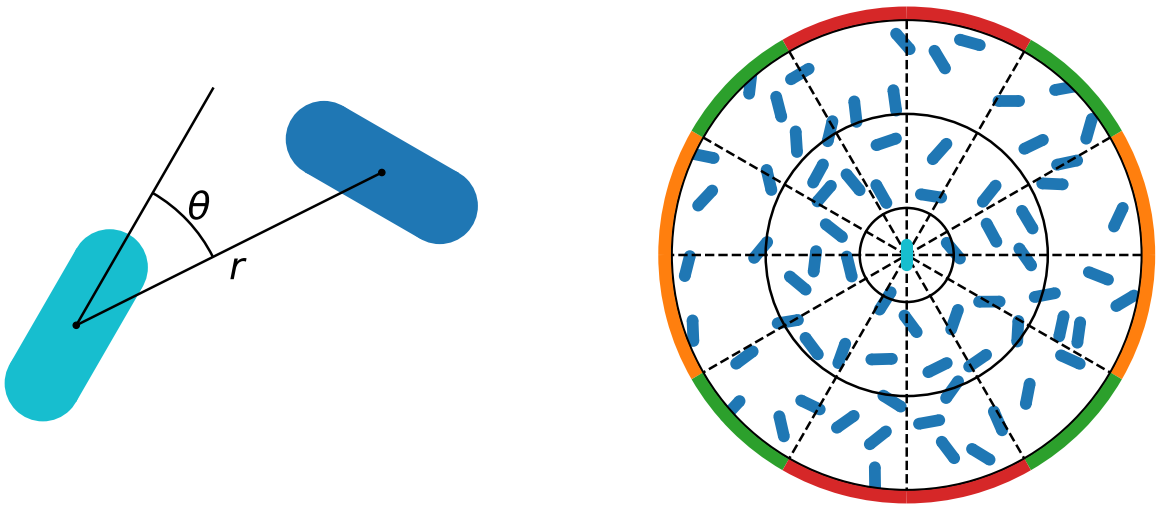

(a) (b)

Figure 3.7: The neighborhood space surrounding a nanomagnet is divided into bins based on euclidian distance, r, and orientation, θ. (a) θ is the polar angle with respect to the easy axis, defined mod(90°). (b) The size of the bins used to discretize the neighborhood space depend on the two discretization parameters Δr and $\Delta\theta$. Illustrated for $\Delta\theta = 30°$ Equal sector color correspond to equivalent angular bins. Red: $\theta \in (0°, 30°)$, green: $\theta \in (30°, 60°)$, orange: $\theta \in (60°, 90°)$.

The angle θ is taken mod(90°), as it does not make sense to have a different angle when a spin magnetic moment flips. That would require us to recalculate the neighborhood space every time a magnet flips. Using this parameterization, $\theta = 0°$ and $\theta = 90°$ correspond to a neighbor magnet placed along the easy axis and hard axis of the center magnet, respectively.

Using the two colored pairs in the ground state square ASI in Figure 3.6 as an example, they are both separated by $r = 1a$, but the green and red pairs are associated with $\theta = 90°$ and $\theta = 0°$, respectively. The difference in θ will prevent the correlation values from averaging to zero. This method can thus capture the order found in the square ASI in its ground state, which the cartesian correlation function failed to do.

Figure 3.8 illustrates how the PCF discretizes the neighborhood space in an Ising ASI using the parameters r and θ. The ground state captures perfect correlation (red squares), whereas the random spin configuration have correlation values close to 0 for all combinations of r and θ except from the self-correlation, $C(\mathbf{0})$. Empty squares in the heat maps represent combinations of r and θ that do not correspond to any magnet pairs in the ASI.

The one-dimensional correlation function is calculated by compacting the PCF, similar to the

method used by Saccone *et al.* in Eq. (2.23):

$$C_{\text{avg}}(r) = \frac{1}{N_{\text{bins}}^{(r)}} \sum_i C(r, \theta_i). \tag{3.5}$$

$N_{\text{bins}}^{(r)}$ is the number of non-empty bins with euclidian distance r. Effectively, this collapses the grid in Figure 3.8 to a one-dimensional array by averaging all non-empty bins with the same r to just one value.

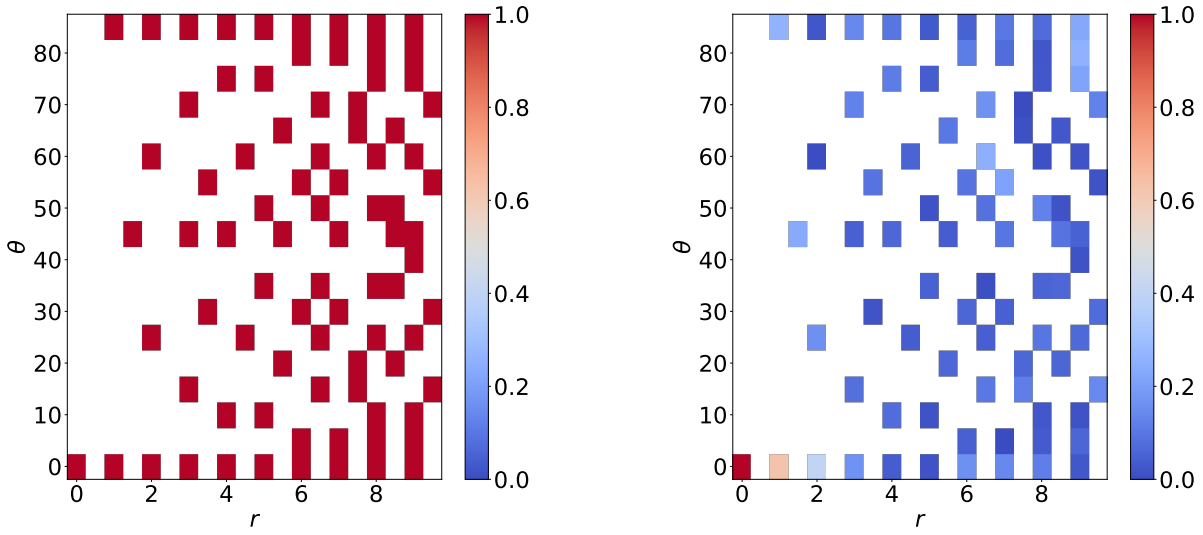

(a) (b)

Figure 3.8: The polar correlation function discretizes the nanomagnet neighborhood space into cells based on the separation distance, r and the polar angle, θ. (a) Ising ASI in the ground state spin configuration. Perfect correlation (red color) is found for combinations of r and θ where all corresponding nanomagnet pairs are either correlated or anticorrelated. (b) The same ASI is prepared in a random spin configuration, showing how the correlation function now is closer to 0 for all combinations of r and θ, except the self-correlation, **0**. Empty cells are combinations of r and θ where there are no corresponding nanomagnet pairs.

Figure 3.7b illustrates how the neighborhood space is discretized into bins of radial size Δr and sectors of size $\Delta\theta$. Since θ is defined mod(90°), every angular bin is repeated four times. Equally colored angular bins (red, green and orange) in the figure correspond to equivalent θ.

The number of bins is determined from the parameters Δr and $\Delta\theta$. It is not a trivial problem to find the "correct" discretization of the neighborhood space. We will first see what happens in the limits of very coarse discretization (large Δr and $\Delta\theta$) and very fine discretization (small Δr and $\Delta\theta$).

As $\Delta r \to \infty$ and $\Delta\theta = 90°$, all magnets will be placed in the same bin. For a well known design such as the square and Ising ASIs, that would give an average correlation function of zero. The effect is illustrated for an Ising ASI in Figure 3.9a using $\Delta r = 2.5a$ and $\Delta\theta = 30°$. The ASI is in its ground state spin configuration, and we would thus expect to capture perfect correlation. However, the large cell sizes result in 3 neighbor magnets being placed into the same bin (those labeled by $+1$ and -1). The effect is an average correlation value for that bin of 0.33, despite being in the ground state.

In the opposite limit, too fine discretization can give two different results. For an ASI based on a lattice geometry, such as the Ising ASI, there will be a parameter set Δr_{min} and $\Delta\theta_{\text{min}}$ such that

only a small fraction of the bins are occupied by magnet-magnet pairs, and reducing Δr and $\Delta\theta$ further will only create empty bins. For an ASI without a periodic geometry, such as the DI model with sufficiently high σ_x and σ_y, we can expect every non-empty bin to contain only *one* magnet pair. After taking the absolute value, that would give presumebly perfect correlation, regardless of the system's spin configuration. Such unwanted, artificially high correlation is illustrated in Figure 3.9b. This system will produce perfect correlation, regardless of the spin configuration.

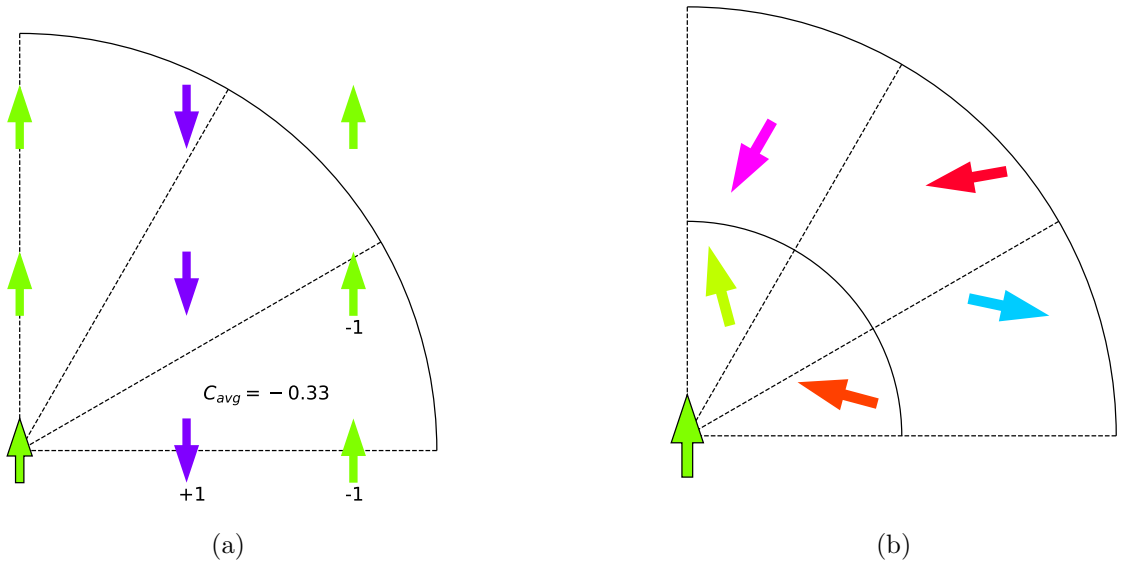

(a) (b)

Figure 3.9: Illustration of the limits with too coarse and too fine discretization of the nanomagnet neighborhood space. (a) predicts a correlation of 0.33 for the perfectly ordered Ising ASI, and (b) predicts perfect correlation regardless of the spin configuration.

Values for Δr and $\Delta\theta$ must be set to avoid any of the above limits. By sweeping the discretization parameters and calculating the correlation lengths for every combination in the Ising and square ASIs, we expect to find values such that the PCF captures magnetic ordering in these systems.

The PCF discretization parameters are swept from $\Delta r = 0.1a$ to $\Delta r = 1.9a$ with stepsize $0.2a$, and from $\Delta\theta = 1°$ to $\Delta\theta = 21°$ with stepsize 2°. The correlation length is calculated for every combination of Δr and $\Delta\theta$ for Ising and square ASIs in 3 different spin configurations. First, the ASI ground states are used in order to identify the discretization parameters that give "diverging" correlation lengths. Next, the correlation lengths are calculated for the ASIs in random spin configurations. If we know the direction of one macrospin, we still have no information about the direction of its neighboring macrospins in a system with random spin configuration. We therefore identify the discretization parameters that give correlation lengths $\zeta < 1a$. Finally, the correlation lengths are calculated in spin configurations obtained after annealing and gradual cooling to 500 K (Ising) and 2500 K (square). These configurations are close to the ASIs respective ground states, but do not match exactly. The "true" correlation lengths are assumed to be those produced by a "lattice correlation function" (LCF).

The LCF is calculated based on the fixed lattice points in periodic ASIs, such as the Ising and square. It is not necessary to create bins like those illustrated for the PCF in Figure 3.7b, since the separation between any two magnets can be expressed in terms of the lattice vectors. Furthermore, there are several magnet pairs separated by the exact same vector, $\mathbf{r}_{ij}$, which cannot be guaranteed in a system without periodicity.

The 4-fold rotational symmetry in a square ASI is preserved in the lattice correlation function, $C_{\mathrm{L}}(\mathbf{r})$, by expressing the position vector $\mathbf{r}_{ij}$ between macrospins i and j in the reference frame

of macrospin i. The x-component of $\mathbf{r}_{ij}$ is in the direction along i's *hard* axis (perpendicular to the spin direction), and the y-component is along *easy* axis.

For example, consider again the colored macrospin pairs in Figure 3.6. The macrospins in the green pair are separated by a vector $\mathbf{r}_{ij} = a\hat{\mathbf{x}}$ (perpendicular to the spin direction), while those in the red pair are separated by $\mathbf{r}_{ij} = a\hat{\mathbf{y}}$ (along the spin direction).

The correlation lengths calculated using the LCF are compared with the domain sizes in the Ising and square ASIs in the random spin configurations and after annealing and gradual cooling to 500 K and 2500 K, respectively. There is no 1 : 1 relation between the correlation length and the radius of a magnetic domain, but we do expect them to be within the same order of magnitude. A visual comparison is done to verify this.

The magnetic domains can be plotted in flatspin by stepwise moving a window through the ASI. For every step, the sum of the magnetic moments are plotted with a color corresponding to the direction of that sum, using the same color coding as illustrated in Figure 3.2.

For the Ising ASI, a window of size $2a \times 2a$ is moved in steps of $1a$ through the entire system. At every step, exactly 4 macrospins are enclosed by the window. In the ground state spin configuration (see Figure 3.1c), the sum of these will always be zero (2 up and 2 down). If on the other hand for example all 4 macrospins in the window point up, the sum of macrospins in that window will point in the same direction.

The magnetic domains for the square ASI are plotted similarly, using a window of size $3a \times 3a$ moved in steps of $2a$ and cropped by $1a$. The exact flatspin commands that are used can be found in Appendix A.

3.3.3 Testing the polar correlation function

A series of tests are performed to investigate the polar correlation function's ability to capture magnetic ordering. The discretization parameters are set to $\Delta r = 0.3a$ and $\Delta\theta = 3°$, which gave reasonable correlation lengths following the procedure from the previous section.

First, the PCF is used to compute the one-dimensional correlation functions for Ising and square ASIs in 5 different spin configurations. These systems are useful because of their well known ground states, providing a baseline for "perfect correlation". The ground state and random spin configurations are used as references where we expect to capture the most and least order, respectively. The correlation function is also calculated for spin configurations following annealing and gradual cooling according to the temperature profile in Eq. (3.3). The annealing temperatures used are $T_{\text{start}} = 2000\,\text{K}$ and $T_{\text{start}} = 3000\,\text{K}$ for the Ising and square ASIs, respectively, both with a decay constant of $\tau = 1.5$. As discussed in Section 3.2.1, these temperatures are not directly transferable to a laboratory.

For the ground state configurations, we expect to find perfect correlation for both systems, and not only the Ising ASI as was the case for the correlation function used in Figure 3.5. As the temperature T_{end} is increased, we expect the correlation function to drop, approaching that for the random spin configuration with correlation length $\zeta < 1$.

The next test is done to see how the PCF captures order in ASIs with geometric disorder and to make sure it does not "find order" where it should not. The correlation length, ζ, is again used as a metric to characterize magnetic ordering. 3 variations of the DI and RDI ASIs (6 in total) are used for this test, both in a random spin configuration and in a spin configuration following thermal annealing to $T_{\text{start}} = 2000\,\text{K}$ and gradual cooling to $T_{\text{end}} = 500\,\text{K}$. The Ising ASI is also included as a reference. The same temperature protocol is used across all systems, allowing us to observe only the effect of increasing geometric disorder.

The correlation lengths are calculated for each of the ASIs in both spin configurations. In the random spin configuration, we expect $\zeta < 1$ for all ASIs, regardless of the geometric design. In the annealed spin configurations, we expect the Ising ASI to exhibit the longest correlation length, and that the effect of geometric disorder in the DI and RDI ASIs reduces long-range ordering.

3.4 Analysis of magnetic order in ASI

This section combines the building blocks established in Chapters 2 and 3 into a methodology that can be used to analyze magnetic phases and types of magnetic ordering in simulated ASIs.

Section 3.4.1 describes simulation runs in flatspin done over a range of different T_{end}, referred to as a temperature sweep. In Section 3.4.2 we go through the steps of computing the correlation functions and magnetic susceptibilities at each of the temperatures in a sweep. Finally, in Section 3.4.3, the Curie-Weiss law is used to estimate the ASIs' critical temperatures and calculate the order parameter, ν.

The methodology in this section is general and does not depend on the exact ASI design. For this reason, we do not refer to the individual ASI models while describing the steps. The ASI models that are analyzed and have results presented in Chapter 4 are Ising, square, DS, pinwheel, $\text{DI}_{0.1,0.0}$, $\text{DI}_{0.0,0.1}$, $\text{DI}_{0.1,0.1}$ and RDI with σ_ϕ ranging from 30° to 90°.

3.4.1 Temperature sweeps

A coarse temperature sweep is first conducted for all ASI models. The ASIs are annealed to T_{start} and gradually cooled down to 25 different end temperatures, T_{end}, between 1 K and T_{start}. An example command used with flatspin for these sweeps can be found in Appendix A.

The correlation lengths are computed for each temperature step by doing a least squares curve fit (trust region reflective method, implemented in Scipy [41]) of the correlation function with an exponentially decreasing function such that

$$C_{\text{avg}}(r) \sim e^{-r/\zeta}. \tag{3.6}$$

The low and high estimation bounds in the least squares algorithm are set to $0a$ and $1000a$, respectively, with an initial guess of $5a$.

Temperature ranges where the correlation lengths decrease with increasing temperatures are chosen for fine temperature sweeps. This typically happens over one temperature range per ASI, and is where we expect to see a phase transition and breaking of long-range ordering.

Fine temperature sweeps are conducted for each model over the phase transition temperature ranges that was identified from the coarse sweeps. 10 identical and independent fine temperature sweeps are run for each model, each with 25 different values for T_{end}. This give a total of 250 flatspin runs per ASI model.

3.4.2 Calculating correlation functions and magnetic susceptibility

The polar correlation function $C(r, \theta)$ is computed for every flatspin run using the spin configuration at the final timestep. The discretization parameters described in Section 3.3.2 are set to $\Delta r = 0.3a$ and $\Delta\theta = 3°$. Since we expect the correlation function to go to zero for very distant macrospins, only magnet pairs closer than $10a$ are considered. This reduces the time spent on

computations significantly compared to a scenario where every possible magnet pair in an ASI has to be considered. Again, a refers to the lattice constant in the Ising and square ASI, which is also the average nearest neighbor distance in the DI and RDI models.

The temperature dependent magnetic susceptibility is computed at every temperature step using Eq. (2.26). The sum over $C(r,\theta)$ is taken as the average value from all 10 correlation functions produced at that temperature:

$$\chi(T) = \frac{m^2}{k_{\mathrm{B}}T}\frac{1}{10}\sum_{i=1}^{10}\Big(\sum_{r,\theta} C_{T,i}(r,\theta)\Big). \tag{3.7}$$

The subscripts in C refer to the correlation function for flatspin run number i at temperature T. The uncertainty related to the *inverse* magnetic susceptibility is:

$$\sigma_{\chi^{-1}} = \frac{\sigma_{C_{\mathrm{sum}}}}{\chi \cdot C_{\mathrm{sum}}}, \tag{3.8}$$

where the sum over the correlation function is denoted by $C_{\mathrm{sum}} = \frac{1}{10}\sum_{i=1}^{10}\Big(\sum_{r,\theta} C_{T,i}(r,\theta)\Big)$ and $\sigma_{C_{\mathrm{sum}}}$ is the corresponding standard deviation. We calculate the uncertainty of the *inverse* susceptibility as it will be numerically easier to work with.

The average one-dimensional correlation functions are also computed using a thermal average from the 10 runs,

$$C_{\mathrm{avg},T}(r) = \frac{1}{10}\sum_{i=1}^{10} C_{\mathrm{avg},i}(r), \tag{3.9}$$

where $C_{\mathrm{avg},i}(r)$ is the average one-dimensional correlation function for *one* run, computed with Eq. (3.5). For every temperature, the correlation length $\zeta(T)$ is obtained by performing a least squares curve fit of $C_{\mathrm{avg},T}(r)$ with the exponential function in Eq. (3.6). This give a list of 25 values for $\zeta(T)$ within the temperature range used in the fine sweep. The correlation length as a function of temperature is used to compute the critical exponent in the next section.

3.4.3 Estimating ASI critical temperature and critical exponent

Curie-Weiss law, Eq. (2.11), gives an analytical expression for $\chi(T)$. This law is only valid for the superparamagnetic phase, i.e., temperatures above the critical temperature. Increasing the temperature above the critical temperature increases the disorder in a system. The superparamagnetic temperature range is therefore defined as the range where $\zeta(T)$ is decreasing with increasing temperature. Only data from the superparamagnetic phase are used when calculating the criticial temperature and exponent. In order to avoid exclusion of data based on randomness in the simulations, we do not require $\zeta(T)$ to be strictly decreasing with increasing temperature. Instead, a naive condition is set as:

$$\zeta(T_i) > 0.8 \cdot \zeta(T_{i+1}),$$
$$\zeta(T_i) > \zeta(T_{i+2}).$$

Here, T_i and T_{i+1} are subsequent temperature steps, and $T_i < T_{i+1}$. This condition allows us to account for some noise in the correlation length data.

The critical temperature is estimated by comparing the two expressions for magnetic susceptibility, Eqs. (2.11) and (3.7). We use the inverse magnetic susceptibility to avoid a singularity in the Curie-Weiss law close to the critical temperature. The Curie constant, C_{Curie} and the critical temperature, T_{C}, in Eq. (2.11) are estimated by doing a least squares linear polynomial fit of the inverse Curie-Weiss law with the inverse susceptibilities calculated in the previous section.

The final step in the magnetic analysis is to estimate a value for the critical exponent, ν. A least squares curve fit is performed to fit the power law in Eq. (2.27) to the temperature dependent correlation lengths, $\zeta(T)$. The low and high estimation bounds for ν are set to 0.0 and 10.0, respectively, with an initial guess of 0.5. Again, only the temperature range in the superparamagnetic phase is considered. The curve fit produces best-fit values for A, a prefactor, and the critical exponent, ν.

The analogy between the macrospins in ASIs and atomic magnetic moments in a magnetic material motivates us to combine estimated critical temperatures with the Weiss localized moment theory, which was introduced in Chapter 2. Weiss theory provides an analytical expression for the critical temperature of a magnetic material with strong interactions between adjacent magnetic moments. The critical temperature is given in Eq. (2.13) and depends on the density of magnetic moments, N, and the Weiss molecular field constant, γ. Using Eq. (2.13) with the critical temperatures estimated in this section, we calculated the "super"-molecular field constant for the Ising, square and pinwheel ASIs.

3.5 Generating new ASI designs with evolutionary algorithms

We combine the methodology described in the previous section to construct a fitness function for generation of new ASIs using evolutionary algorithms. The ASIs are generated and evolved using a tool created by Penty *et al.*, based on the principles that were briefly described in Section 2.6.

Running these evolutions with large populations can be computationally demanding. We use a maximum of 10 individual ASI designs per generation, each consisting of 1000 nanomagnets. The "genes" are restricted to 4 tiles, also to reduce computational complexity.

The fitness function we use is based on the analysis of magnetic ordering described in the previous section. The "fitness" of individual ASIs are set to favor systems with critical temperature closer to 1000 K. More specifically, the evolutionary algorithms try to minimize the value of Δ, defined as

$$\Delta = |T_{\text{C}} - 1000\,\text{K}|. \tag{3.10}$$

The methodology from the previous section used to estimate T_{C} has only been tested on a few different ASIs. It is naive to believe this method will give excellent results, but we hope it will give insights into how the fitness function can be developed further.

The flatspin simulator parameters given in Table 3.1 are set such that all nanomagnet coordinates has to be given in the unit of the lattice spacing, a. The ASI generation tool on the other hand give all coordinates in the unit of nm, and the average nearest neighbor distance between adjacent nanomagnets are on the order of 200 nm. The dipolar interactions between neighboring nanomagnets would thus be negligible if we do not scale the dipolar coupling coefficient, α, accordingly. After consulting the developers of flatspin and the ASI generation tool, the dipolar coupling coefficient is set to `alpha=68437`. This value corresponds to a magnetic volume of $1\,\text{nm}^3$, according to the definition of α given in the rightmost column of Table 3.1. That volume is about 6 orders of magnitude lower than the volume of a nanomagnet in a fabricated ASI. Instead of reconfiguring the simulator to obtain values closer to the analytical predictions, we

chose to move forward with this setup as it suffices for a demonstration of the methodology.

The flatspin parameter `neighbor_distance` is also adjusted to account for the scaling of coordinates. For simplicity, we set this value to `inf`, thus considering all nanomagnets in the system as each others neighbors.

When calculating the polar correlation function in generated ASIs, Δr is scaled with the minimum neighbor distance between adjacent macrospins. In Section 3.3.2 we defined the PCF discretization parameter Δr in terms of the lattice spacing, a. $\Delta r = 0.3a$ and $\Delta\theta = 3°$ gave reasonable correlation lengths for the Ising and square ASIs following the parameter sweeps in that section. For the generated ASIs, Δr is scaled with $r_{\min}$, the shortest distance between any two magnets in the ASI:

$$\Delta r = 0.3 \cdot r_{\min}. \tag{3.11}$$

If the minimum nearest neighbor distance in one ASI design is 150 nm, we set $\Delta r = 45$ nm. Furthermore, the PCF neighborhood size is extended from 10 a, given in Section 3.4.2, to $0.25 \cdot r_{\max}$, where $r_{\max}$ is the longest distance between any two magnets in the ASI.

The exact command that was used and all parameters related to flatspin and the evolutionary algorithms tool can be found in Appendix A.

Chapter 4

Results and Discussion

In this chapter we present and discuss the results from simulations and analyses of magnetic ordering. The results from the experimental parts depend on each other such that it is more convenient and easier to follow when discussed as they are presented. We will therfore not follow the IMRaD structure and instead combine the results and discussions into one chapter.

A similar structure as the one used to describe the steps carried out in Chapter 3 is followed. Sections 3.1 and 3.2 do not have any direct results that is presented in this chapter, but they were necessary building blocks for the last three sections of Chapter 3.

In Section 4.1 we present results from the PCF discretization parameter sweeps and discuss how they affect the analysis of magnetic ordering. We also present and discuss results from the PCF testing done on ASI models with well known ground states and how the PCF performs on ASIs with geometric disorder.

The results from the analysis of magnetic ordering is presented in Section 4.2. We compare and discuss the results from the different ASIs, trying to identify any trends in magnetic order and order parameters when the geometric design of a system changes. Relevant work found in the literature, primarily the analysis on fabricated ASIs done by Saccone *et al.*, is used to discuss the reliability of the results. We also comment on the results using Langevin and Weiss theory described in Chapter 2.

Finally, in Section 4.3 we present some of the exotic ASIs that are generated using evolutionary algorithms with a fitness function based on critical temperature.

4.1 Configuration and testing of the polar correlation function

The results from the configuration and testing of the polar correlation function are presented and discussed in this section. We use the results to define a set of optimal discretization parameters, Δr and $\Delta\theta$.

4.1.1 Discretizing the nanomagnet neighborhood space

The parameter sweeps for the PCF discretization parameters can be seen plotted in heat maps in Figure 4.1. The cell colors and annotated values correspond to the correlation length produced using that combination of Δr and $\Delta\theta$.

The top row in Figure 4.1 ((a) and (b)) show the correlation lengths produced for the Ising and square ASIs, respectively, in their ground state spin configurations. Here, we expect the corre-

lation function to capture the long-range ordering apparent for these systems, thus producing a large value for the correlation length. For the finest grid, with $\Delta r = 0.1a$ and $\Delta\theta = 1°$, we observe this long-range order for both ASIs (bottom left corner of the heat maps). $\zeta = 1000a$ is the maximum allowed value of ζ in the least squares curve fit and exceeds the size of the system. As Δr and $\Delta\theta$ are increased, we eventually see the correlation lengths dropping below $\zeta = 5a$ for the exact same geometry and spin configuration. This is an expected effect of too coarse discretization of the macrospin neighborhood space. Despite perfect magnetic order, correlated and anticorrelated macrospin pairs that are placed in the same bin give a net correlation close to zero when averaging. This is the effect that was illustrated in Figure 3.9a. Based on the results from the parameter sweeps for the Ising and square ASIs in their ground states, we narrow the solution space for the discretization parameters down to $\Delta r \leq 0.9a$ and $\Delta\theta \leq 3°$. All those configurations give the maximum allowed correlation lengths, $\zeta = 1000a$. The PCF is thus able to capture the magnetic ordering as expected for these perfectly ordered ASIs.

Figures 4.1 (c) and (d) show the same parameter sweeps for the Ising and square ASIs after annealing and exponentially cooling down to flatspin's 500 K and 2500 K, respectively. The largest values for ζ can again be found for the finest discretization in the bottom left corners of the heat maps. Conversely, the smallest values are in the upper right corners, an effect of too coarse discretization. The "true correlation length" for these systems are assumed to be those found by applying the lattice correlation function (LCF), that was described in Section 3.3.2. The correlation lengths produced by the LCF were $13.2a$ and $67.7a$ for the Ising and square ASIs, respectively. The solution space for the discretization parameters that give correlation lengths within $\pm 2a$ of these values are $\Delta r \leq 0.7a$ and $\Delta\theta \leq 3°$. For these combinations of Δr and $\Delta\theta$, the PCF captures the magnetic ordering in the Ising and square ASIs with correlation lengths close to those calculated using the LCF.

For both the ground state and annealed spin configurations, the square ASI requires a finer discretization of the macrospin neighborhood space in order to produce the correlation lengths we expect. In particular, the parameter $\Delta\theta$ is restricted to lower values for the square ASI compared to the Ising ASI. This is because the square ASI has more than twice as high macrospin density as the Ising ASI. A region of size $50a \times 50a$ can fit 2500 macrospins when they are placed on the Ising model's lattice points. The same region on a square ASI can fit $2 \cdot 50 \cdot 51 = 5100$ macrospins. This observation highlights a drawback with the current implementation of the PCF as a generalized correlation function. We want the PCF to perform equally well for any ASI geometry, and the optimal discretization parameters should thus not depend on the specific ASI. One possible solution to overcome this challenge can be to express the parameters in terms of the macrospin density or nearest neighbor distance, as was described in Section 3.5 for the ASIs that were generated using evolutionary algorithms.

The final two heat maps in Figure 4.1 were produced on the same ASI models, but this time in random spin configurations. No macrospins were allowed to flip before calculating the correlation functions. Here, we expect the correlation lengths to be less than $1a$, since knowledge about the direction of one macrospin does not give any information about its neighbor. As expected, we observe $\zeta < 1a$ for both ASI models, regardless of the values of Δr and $\Delta\theta$.

Based on the results from these six discretization parameter sweeps and comparison with the lattice correlation function, we decide to move forward with

$$\Delta r = 0.3a,$$
$$\Delta\theta = 3°.$$

With these values, the correlation lengths computed by the PCF and the LCF have discrepancies less than 2.5 %. A summary of the correlation lengths produced by the PCF and LCF using the specified configuration is given in Table 4.1.

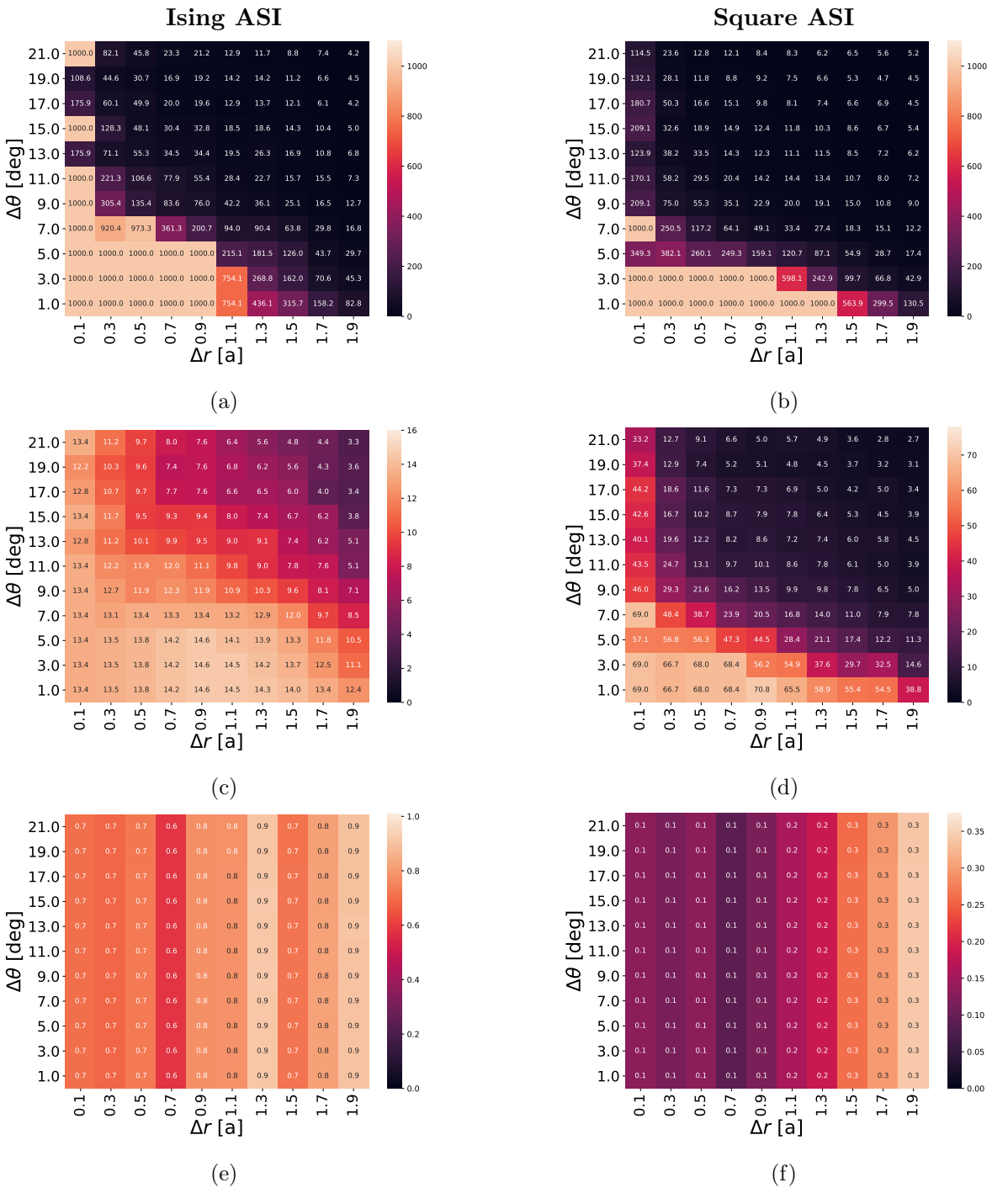

Figure 4.1: PCF discretization parameter sweeps done on Ising ASI (left) and square ASI (right). The colors and annotated values are the calculated correlation lengths using the PCF and that combination of Δr and $\Delta\theta$. (a), (b) in the ground states, (c), (d) annealed and gradually cooled, and (e), (f) random spin configuration.

It is important to note that capturing macrospin order in these systems does not mean that we have succeeded in building a generalized correlation function. One of the requirements for a generalized correlation function is however also to be able to capture magnetic ordering in these periodic systems, as they form a subset of "all ASIs". The results are therefore useful.

The correlation lengths in Table 4.1 are measures of the maximum distance between two macrospins where, if we know the state of one of the macrospins, we can expect to predict the other one

Table 4.1: Correlation lengths calculated using the lattice correlation function (LCF) and the polar correlation function (PCF) with $\Delta r = 0.3a$ and $\Delta\theta = 3°$ for Ising and square ASIs in three different spin configurations. The rightmost column gives the discrepancies between the calculated values.

ASI model	Spin configuration	ζ/a (LCF)	ζ/a (PCF)	Discrepancy
Ising	Ground state	1000	1000	0 %
	$T_{\text{end}} = 500\,\text{K}$	13.2	13.5	2.3 %
	Random	0.7	0.7	0 %
Square	Ground state	1000	1000	0 %
	$T_{\text{end}} = 2500\,\text{K}$	67.7	67.2	0.74 %
	Random	0.1	0.1	0 %

correctly. Such spin coherence gives rise to magnetic domains. A visualization of the magnetic domains of the same ASIs can be seen in Figure 4.2. The first row are for the Ising and square ASIs in spin configurations obtained after thermal annealing and gradual cooling. The second row is for the same ASIs, but in a random spin configuration where every macrospin state is set randomly and independent from any other. White color in the plots in Figure 4.2 correspond to a net zero magnetization, whereas colored areas represent areas with nonzero net magnetic moments according to the color map in Figure 3.2. "Magnetic domains" refers here to coherent areas with equal color. There is no direct 1 : 1 relationship between the correlation length and domain size, but we do expect them to be of similar orders of magnitude.

For the annealed and gradually cooled Ising ASI, we see that there are primarily 3 magnetic domains. The largest domain, in the middle of the plot limited by the two vertical lines, is roughly $25a$ wide and $50a$ tall (the size of the system). These dimensions are larger than the calculated correlation length of $\zeta = 13.5a$, but within the same order of magnitude.

In Figure 4.2b, for the square ASI, we observe no clear domain walls, only small regions where macrospins disagree with the overall domain configuration. This observation agrees with the fact that the correlation length we found for this system, $\zeta = 67.2a$, is almost twice the size of the system.

For the random spin configurations in the bottom row of Figure 4.2 we see no large domains for any of the ASIs. This observation agrees with the expected correlation lengths of $\zeta < 1$, since no macrospin contains any information about the state of its neighbors.

While the observations from comparing the correlation lengths with magnetic domains do not represent a general validation of the PCF, it is a good test and once again confirms the PCF's ability to capture order in these lattice based ASIs.

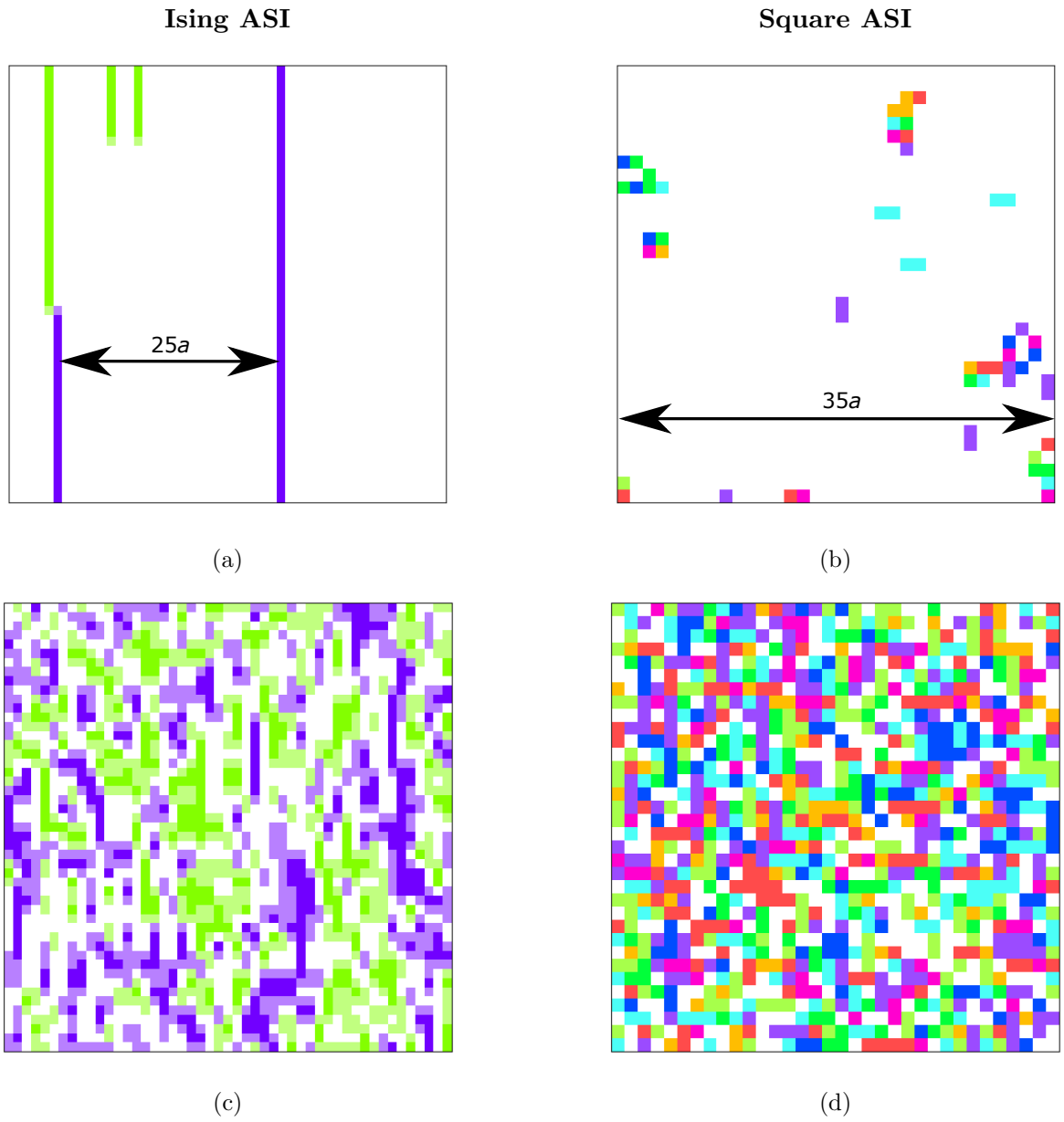

Figure 4.2: Magnetic domains for the Ising ASI (left column) and square ASI (right column). The colors correspond to the direction of the magnetic moment according to the color map in Figure 3.2. (a), (b) Spin configurations after annealing and gradual cooling give large magnetic domains for both ASIs. (c), (d) No magnetic domains are dominating in the random spin configurations.

4.1.2 One-dimensional PCF for ASIs with known ground states

Figures 4.3 and 4.4 show the one-dimensional PCF for the Ising and square ASIs in 5 different spin configurations. The ground states and random spin configuration represent the two limits between perfect magnetic ordering and complete disorder. They are plotted with corresponding exponential curve fits with $\zeta = 1000a$ for the ground states (upper estimation bound in curve fitting algorithm) and $\zeta = 0.7a$ and $\zeta = 0.1a$ for the random spin configurations in the Ising and square ASI, respectively. The final three correlation functions were calculated on systems after they had been annealed and gradually cooled down to three different end temperatures, T_{end}.

In Figure 3.5, we saw how the cartesian correlation function failed to capture order for the square

ASI in its ground state. The blue circles and dashed blue line in Figure 4.4 show how we have worked around this issue, capturing perfect correlation for the square ASI as well. This result suggest that we are one step closer to having a generalized correlation function.

Both of the ASIs exhibit perfect correlation in their ground state spin configurations. For spin configurations following the thermal annealing and exponential cooling protocol, we observe that as the temperature is increased, the correlation function decreases more rapidly for $r > 0$. This reflects how random thermal fluctuations become more important at elevated temperatures. At the highest temperatures, the thermal fluctuations dominate and the dipolar interactions are almost negligible. The correlation functions for the random spin configurations fall below $1/e$ for $r < 1$ for both ASI models, as expected in a random spin configuration.

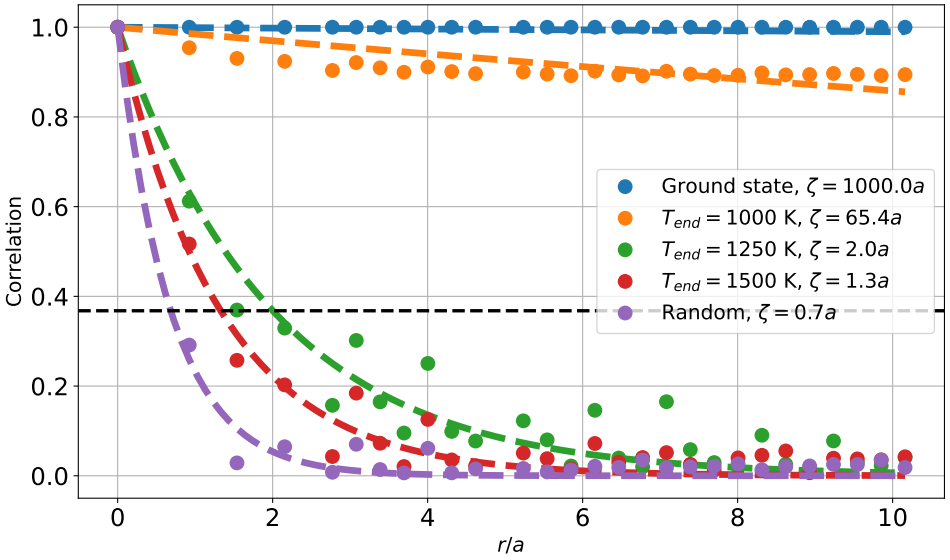

Figure 4.3: The one-dimensional correlation function for Ising ASI calculated using the PCF. Perfect correlation (capped at $1000a$) for the ground state spin configuration, and decreasing correlation lengths with increasing temperatures. The black dashed line is at $1/e$.

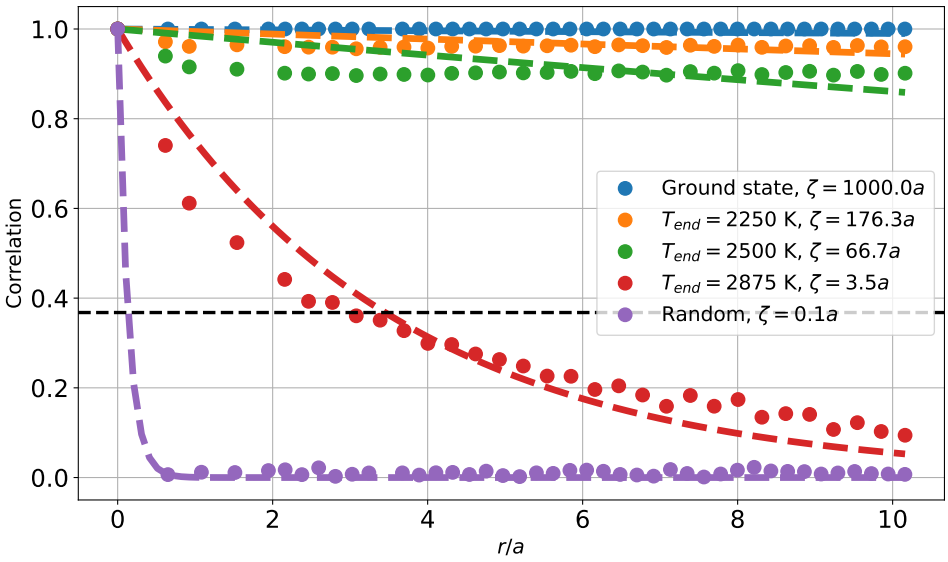

Figure 4.4: The one-dimensional correlation function for square ASI calculated using the PCF. In contrast to a similar plot using the cartesian correlation function in Figure 3.5, we now observe perfect correlation (capped at $1000a$) for the ground state spin configuration. Decreasing correlation lengths with increasing temperatures as expected. The black dashed line is at $1/e$.

4.1.3 Magnetic ordering in ASIs with geometric disorder

The DI and RDI ASIs were introduced in Section 3.1 as Ising ASIs with separate Gaussian disorder on their x- and y- coordinates and element-wise rotation, ϕ. They are referred to using the notation $\mathrm{DI}_{\sigma_x,\sigma_y}$ and $\mathrm{RDI}^{\sigma_\phi}_{\sigma_x,\sigma_y}$, where the subscripts and superscripts are the standard deviations in the Gaussian distributions from where the disorder is drawn.

Geometric disorder introduces changes in the dipolar energy landscape, and we do not know the spin configuration corresponding to a ground state for these systems—or if they exist. In the previous section, we compared the PCF and the LCF, using the latter as a reference and proxy for the "true values". For the DI and RDI systems, there is no LCF to compare the results with. It is nevertheless useful to compute the correlation functions for these systems and compare them with each other as a method of verification.

Table 4.2 presents the correlation lengths obtained from the PCF for the DI and RDI ASIs with varying disorder in two different spin configurations. The Ising ASI, included for reference, has the longest correlation length among all the systems. Comparing the correlation lengths for the annealed spin configurations, we observe that the introduction of geometric disorder, as expected, reduces long-range magnetic ordering.

Interestingly, the introduction of geometric disorder on the y-coordinate has a larger impact on the magnetic ordering compared to the same disorder on the x-coordinate. The systems are set up according to the illustration in Figure 3.1e, so geometric disorder on the y-coordinate corresponds to position shifts parallel to the magnets' easy axes. Comparing the correlation lengths for $\mathrm{DI}_{0,0.1}$ and $\mathrm{DI}_{0.1,0}$ with the Ising ASI, we see that the correlation lengths have been reduced by 68 % and 19 %, respectively.

The vast difference in magnetic order between the $\mathrm{DI}_{0,0.1}$ and $\mathrm{DI}_{0.1,0}$ ASIs can be explained by considering the dipolar magnetic fields exhibited by nearest neighbor macrospins in an Ising ASI. An example of such a dipolar field was plotted in Figure 2.1. The dipolar field to the left or right

Table 4.2: Correlation lengths calculated using the PCF for Ising, DI and RDI ASIs in two different spin configurations. The subscripts and superscripts in the DI and RDI model names are the standard deviations in the Gaussian distributions from where the disorder is drawn, as described in Section 3.1.

ASI model	Spin configuration	Correlation length, ζ
Ising	500 K	$13.54a$
$DI_{0,0.1}$	500 K	$4.32a$
$DI_{0.1,0}$	500 K	$11.02a$
$DI_{0.1,0.1}$	500 K	$3.91a$
$RDI^{30}_{0,0}$	500 K	$1.65a$
$RDI^{60}_{0,0}$	500 K	$1.14a$
$RDI^{90}_{0,0}$	500 K	$1.17a$
Ising	random	$0.24a$
$DI_{0,0.1}$	random	$0.26a$
$DI_{0.1,0}$	random	$0.35a$
$DI_{0.1,0.1}$	random	$1.05a$
$RDI^{30}_{0,0}$	random	$0.29a$
$RDI^{60}_{0,0}$	random	$0.32a$
$RDI^{90}_{0,0}$	random	$0.32a$

(i.e., along the hard axis) of the macrospin exhibiting it, is directed in the opposite direction of that macrospin. When a neighbor macrospin is placed at this location, it prefers to align with the magnetic field, thus antiparallel to its neighbor. By moving the macrospin's position sufficiently up or down (i.e., along its easy axis), the preferred spin direction will suddenly change because of the curvature of the dipolar field lines. If the macrospin is instead moved horizontallay, either closer to or further away from its neighbor, the preferred macrospin direction will still remain the same. The magnetic ordering in the $DI_{0,0.1}$ ASI is therefore not preserved as well as that in the $DI_{0.1,0}$.

Introducing Gaussian disorder on the element-wise rotation decreases a system's correlation length drastically. The three RDI systems in Table 4.2, with σ_ϕ ranging from 30° to 90°, all have $\zeta < 2a$.

The correlation lengths produced in the random spin configurations are primarily included as a baseline case to see if the PCF can discriminate between systems where we expect to find signs of magnetic ordering and systems with random spin configurations. In Table 4.2 we see that all systems have the longest correlation length in their annealed spin configuration and the shortest in random spin configurations. The PCF is thus able to capture order in all the tested ASIs, including those with geometric disorder and short correlation lengths. This is an important finding for the PCF as a generalized correlation function.

One of the ASI models in Table 4.2 have $\zeta > 1a$ in the random spin configuration, in contrast to our expectation for a system where the state of one macrospin contains no information about

neighboring macrospins. This observation suggests that the macrospin neighborhood space has been discretized into too small bins. The $DI_{0.1,0.1}$ has introduced disorder on both the coordinates, meaning the individual macrospins are less restricted to the Ising ASI lattice points compared to any of the other models. The macrospin pairs will therefore have an increased chance of occupying more bins in the neighborhood space, with fewer pairs per bin. With a too fine discretization of the neighborhood space, the PCF will produce an artificially high correlation for such a system. This effect was described in Section 3.3.2 and illustrated in Figure 3.9b.

The effect of too fine discretization was confirmed by running a discretization parameter sweep on the $DI_{0.1,0.1}$ ASI in the random spin configuration. Figure 4.5 shows the calculated correlation lengths. For the finest discretization, using $\Delta r = 0.1a$ and $\Delta\theta = 1°$, the PCF produces a correlation length of $\zeta = 4.63a$. This is clearly an artificially high number, once again showing the importance of the values of Δr and $\Delta\theta$.

We repeated the calculation of the correlation length using $\Delta r = 0.1a$ and $\Delta\theta = 1°$ to verify it was not an accidentally ordered configurations. After analyzing 60 different, random spin configurations, the correlation length was calculated to be $4.68a \pm 0.05a$. We conclude that the PCF does predict an artificially high correlation length for this ASI, because of a too fine discretization of the neighborhood space.

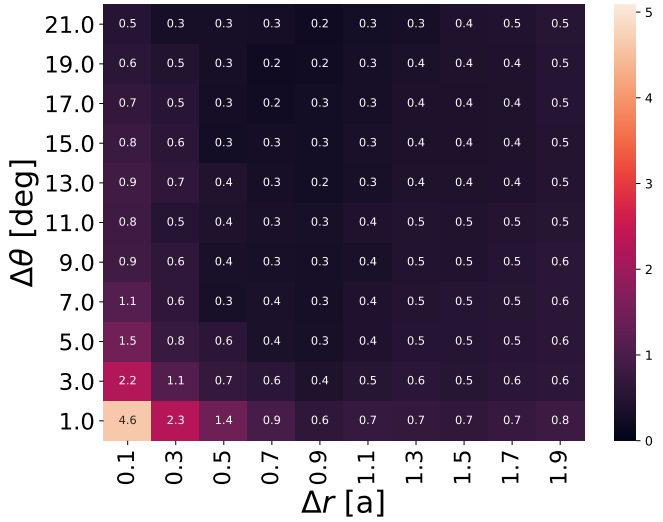

Figure 4.5: Discretization parameter sweep for the $DI_{0.1,0.1}$ ASI in a random spin configuration. The color and annotated values correspond to correlation lengths calculated using that combination of Δr and $\Delta\theta$. Values of more than $1a$ are artificially high correlation lengths because of a too fine discretization of the neighborhood space.

We have highlighted areas where the PCF will give artificially high or low correlation as a result of the discretization of the macrospin neighborhood space. The above results and discussions have also shown that the PCF is able to capture order and discriminate between systems of varying order.

The next section will present results from the analysis of magnetic ordering and estimation of critical parameters. When discussing those results, we will keep in mind the errors related to artificially high or low correlation demonstrated in this section.

4.2 Analysis of magnetic ordering

Results from the analysis of magnetic ordering and estimation of critical parameters are presented in this section. First, Section 4.2.1 describes the simulation sweeps that were carried out and which temperature ranges that were used in the subsequent analyses. Results from the Ising ASI will be used as an example to illustrate how we defined these temperature ranges. In Section 4.2.2 we present the magnetic susceptibilities and correlation lengths that were calculated. We compare the results with theoretical predictions from the Curie-Weiss law and the power law in Eqs. (2.11) and (2.27). In Section 4.2.3 we will evaluate the results by comparing them with similar work from the literature, done on experimentally realized ASIs.

The values found for the discretization parameters in Section 4.1.1, $\Delta r = 0.3a$ and $\Delta\theta = 3°$, is used for the PCF throughout this section.

4.2.1 Temperature sweeps and superparamagnetic phases

The temperature sweeps are summarized in Table 4.3 with the identified temperature ranges for the superparamagnetic phase. The RDI systems with standard deviation on the element-wise rotation, σ_ϕ, greater than 30° are not included in these analyses due to the short correlation lengths found in the previous section.

Table 4.3: Temperature sweeps and identified temperature ranges for the superparamagnetic phases.

ASI model	T_{start}	T_{end} (coarse)	T_{end} (fine)	Superparamagnetic phase
Ising	2000 K	1 K - 2000 K	750 K - 1500 K	$T_{\text{end}} > 930$ K
Square	3000 K	1 K - 2000 K	1500 K - 3000 K	$T_{\text{end}} > 2500$ K
DS	2500 K	1 K - 2000 K	1500 K - 2500 K	$T_{\text{end}} > 1500$ K
Pinwheel	1500 K	1 K - 2000 K	500 K - 1500 K	$T_{\text{end}} > 700$ K
$\text{DI}_{0.1,0}$	2000 K	1 K - 2000 K	750 K - 1500 K	$T_{\text{end}} > 1000$ K
$\text{DI}_{0,0.1}$	2000 K	1 K - 2000 K	750 K - 1500 K	$T_{\text{end}} > 1000$ K
$\text{DI}_{0.1,0.1}$	2000 K	1 K - 2000 K	500 K - 1500 K	$T_{\text{end}} > 930$ K
$\text{RDI}^{30}_{0,0}$	2000 K	1 K - 2000 K	500 K - 1500 K	$T_{\text{end}} > 750$ K

The third column in Table 4.3 gives the temperature ranges that were used for the coarse temperature sweeps. The next column gives the temperature ranges for the fine temperature sweeps, determined based on the calculated correlation lengths from the coarse temperature sweeps.

Identification of the temperature range for the fine temperature sweep is illustrated in Figure 4.6 for the Ising ASI. The low correlation lengths for low temperatures are a result of quenching, i.e., rapid cooling such that the system does not have time to relax. The correlation lengths for frozen systems are plotted as squares, whereas those for the thermally active systems are plotted with circles. Around $T_{\text{end}} = 90$ K, the ASI managed to relax towards a ground state after all, giving a high correlation value. The quenching effect was confirmed by plotting the macrospins of subsequent timesteps, revealing a sudden freezing of the spin configuration. Instead of gradually slower dynamics as the temperature was lowered, i.e., gradually fewer macrospin flips for every

timestep, the flips suddenly stopped, giving a frozen spin configuration.

The large variations in correlation lengths in Figure 4.6 around 900 K indicate that a phase transition might take place here. The correlation length decreases quickly with increasing temperature from 900 K. Above 1500 K, all magnetic ordering has been broken by random thermal fluctuations, resulting in correlation lengths below $1a$. The temperature range $750\,\mathrm{K} < T_{\mathrm{end}} < 1500\,\mathrm{K}$ is therefore chosen for the fine temperature sweep, indicated by the shaded region in Figure 4.6.

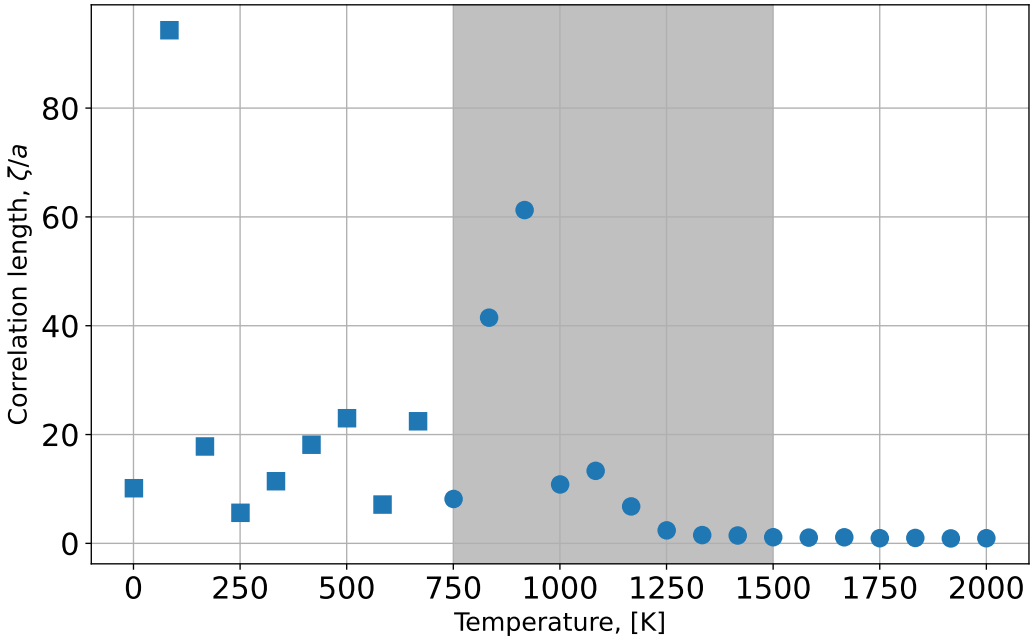

Figure 4.6: Correlation lengths for the Ising ASI calculated from the coarse temperature sweep. The shaded temperature range is used in the fine temperature sweep. The squares to the left of the shaded is a frozen spin configuration. The region to the right is dominated by thermal fluctuations and is excluded from the fine temperature sweep because it gives no more information about the system.

The temperature ranges identified for the superparamagnetic phases are given in the final column in Table 4.3. This is the temperature range where random thermal fluctuations starts to dominate dipolar interactions and break long-range magnetic ordering, indicated by decreasing correlation lengths with increasing temperatures.

The temperatures for the superparamagnetic phase for the Ising ASI was identified as $T_{\mathrm{end}} > 930\,\mathrm{K}$ based on the plot of correlation lengths from the fine temperature sweep in Figure 4.7.

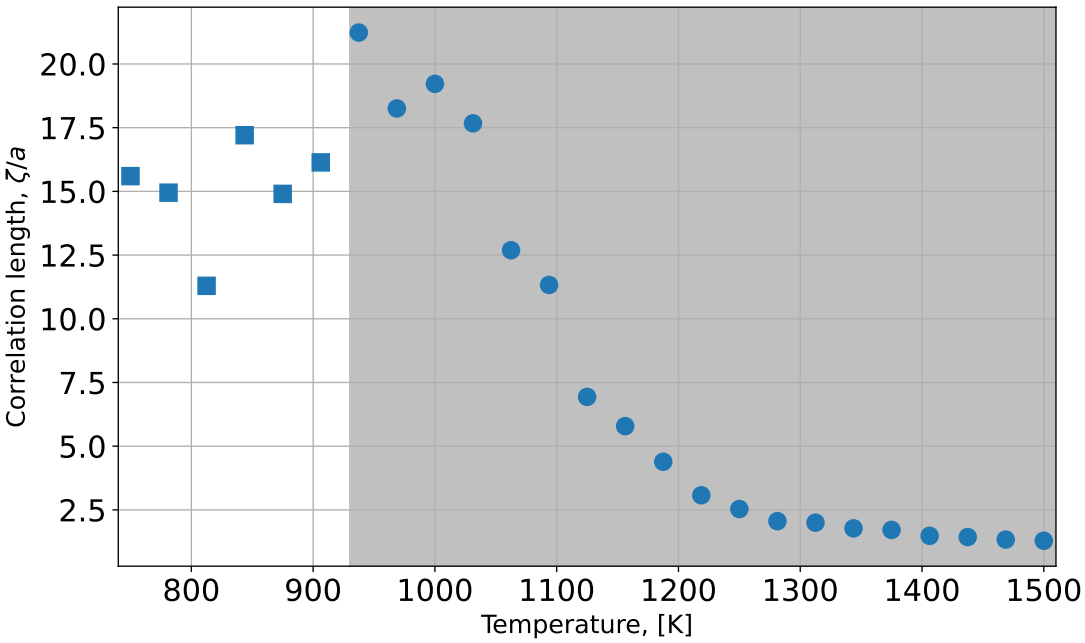

Figure 4.7: Correlation lengths for the Ising ASI calculated from the fine temperature sweep. The shaded temperature range is the identified superparamagnetic phase, used in the analysis of magnetic ordering in the next section. The squares to the left of the shaded region are systems in a frozen spin configuration.

4.2.2 Critical parameters

Figures 4.8 and 4.9 show the inverse magnetic susceptibilities and correlation lengths as a function of temperature for all the ASIs in their respective superparamagnetic temperature ranges. Estimated critical parameters and curve fitting coefficients are summarized in Table 4.4.

For the Ising ASI in Figure 4.8a, we see a clear linear relationship between the inverse susceptibility and temperature, as predicted by Curie-Weiss law. The critical temperature and Curie constant obtained from the least squares curve fit were $T_C = 821\,\mathrm{K}$ and $C_{\mathrm{Curie}} = 2.33 \times 10^{-12}\,\mathrm{K}$.

The correlation lengths for the same Ising ASI, seen in Figure 4.8b, decay exponentially as the temperature increases from $T = 1000\,\mathrm{K}$. This is in good agreement with the behavior predicted by the power law in Eq. (2.27), however with a critical temperature approximately 200 K higher than the value found in our analysis. The best-fit critical exponent when fitting the data to Eq. (2.27) was $\nu = 1.3$, 30 % larger than the "true value" calculated analytically for the two-dimensional Ising model (see Section 2.5.2). Similar analyses were also done using only data from $T = 1000\,\mathrm{K}$ and above, giving a critical exponent of $\nu = 1.8$.

Considering the calculation of the polar correlation function, we do not expect to meet the analytical solution for the Ising model exactly. Discretizing the macrospin neighborhood space and averaging the correlation values for many magnet pairs within the same bin will likely introduce small errors in our analysis.

The temperature implementation in flatspin, which was described in Section 3.2, can also have caused the discrepancy between the calculated and analytical critical exponents for the Ising ASI. If the "laboratory" temperature is not linearly related to the temperature used in this work, the critical exponents found here will not be correct.

Table 4.4: Summary of critical parameters and curve fitting coefficients.

ASI model	T_C [K]	C_{Curie} [K]	A	ν
Ising	820.61	2.33×10^{-12}	2.0	1.3
Square	1742.35	8.00×10^{-13}	0.7	5.11
DS	436.41	1.63×10^{-12}	66.33	2.29
$\text{DI}_{0,0.1}$	724.38	2.22×10^{-12}	1.79	1.32
$\text{DI}_{0.1,0}$	1308.25	9.48×10^{-14}	4.61	0.0
$\text{DI}_{0.1,0.1}$	−670.12	9.48×10^{-12}	50.76	2.56
$\text{RDI}^{30}_{0,0}$	541.88	2.40×10^{-12}	1.01	0.5
Pinwheel	859.76	2.67×10^{-14}	1.24	0.22

The square and DS ASIs show a similar temperature dependence as the Ising ASI. There is a linear trend between temperature and the inverse susceptibilities, and the correlation lengths decay exponentially with increasing temperature. The Curie-Weiss fits (dashed lines) produce critical temperatures of 1742 K and 436 K for the square and DS ASIs, respectively. The high value for the square ASI can be understood from the strong tip-tip interactions and higher density of macrospins. More thermal energy is thus required to break long-range magnetic ordering in the square ASI compared to both the Ising and DS ASIs.

The strong dipolar interactions in the square ASI are also responsible for the long-range magnetic ordering giving rise to the high values for ζ in Figure 4.8d. Interestingly, removing 20 % of the macrospins reduces the correlation lengths by an order of magnitude, as can be seen by comparing the correlation lengths for the square ASI with those for the DS ASI in Figure 4.8f.

The critical temperature found for the DS ASI was not included in the fine temperature sweep for this system. Based on the correlation lengths plotted in Figure 4.8f, we would however expect a higher value than 436 K for T_C, since temperatures below 1500 K gave frozen spin configurations for this ASI.

The inverse magnetic susceptibilities for the DI and pinwheel ASIs highlight a challenge with the magnetic susceptibility calculations. In particular for the $\text{DI}_{0.1,0}$ and pinwheel ASIs, Figures 4.8g and 4.9a, there are large and presumebly random variations in inverse susceptibility. The linear relationship we observed for the Ising, square and DS ASIs is not present for $\text{DI}_{0.1,0}$ and pinwheel. If we chose to use just a subset of the data in Figure 4.9a, the estimated values for T_C would be different depending on what subset we chose. Using the temperature ranges in the figures, we obtained critical temperatures of 1308 K for the $\text{DI}_{0.1,0}$ and 860 K for the pinwheel ASI.

Numerically, the large uncertainties in the susceptibility calculations arise from the sum over the correlation function in Eq. (2.26). We did not characterize or study how this sum changed for different ASIs or as a function of the discretization parameters, Δr and $\Delta\theta$. We did however verify that $\sum_{ij} C(\mathbf{r}_{ij})$ followed our general predictions for random spin configurations, corresponding to high temperatures. For entirely random spin configurations, we expect the sum over the correlation function to be close to 1, since only the self-correlation, $C(\mathbf{0})$, will have a nonzero average. The sum was computed for 100 different spin configurations for the Ising and square ASIs, yielding averages of 1.02 ± 0.16 and 1.01 ± 0.22, respectively.

For spin configurations following annealing and gradual cooling, the sum over $C(\mathbf{r})$ will increase if

the neighborhood space is dominated by correlated ($C_{ij} = +1$) magnet pairs, and decrease if they are anticorrelated ($C_{ij} = -1$). The sum can become less than zero for spin configurations where anticorrelated magnet pairs dominate, resulting in an estimated negative magnetic susceptibility. This was the case for the $\mathrm{DI}_{0.1,0}$ ASI at $T = 1031\,\mathrm{K}$.

Despite the poor linear relation between the inverse susceptibilities and temperature for the $\mathrm{DI}_{0.1,0}$ ASI, the correlation lengths as a function of temperature show a clear exponential decay with increasing temperature. The power law curve fit in Figure 4.9b (horizontal, dashed line) does clearly not capture $\zeta(T)$ when we fix $T_\mathrm{C} = 1308\,\mathrm{K}$. The filled circles instead suggest a critical temperature around 1050 K. A power law curve fit using $T_\mathrm{C} = 1050\,\mathrm{K}$ gave a good fit and critical exponent $\nu = 0.56$ (not shown).

The correlation lengths seen in Figure 4.8h for the pinwheel ASI also appear to follow an exponential decay, especially above 850 K. For these temperatures, the power law fits the filled circles well. It should be pointed out that this fit is based on T_C obtained using the Curie-Weiss law in Figure 4.9a. Although the correlation lengths decay exponentially above this temperature, T_C is likely an accidental hit and does not increase confidence in the calculation of the inverse susceptibilities. If we for example only use the data for $T > 800\,\mathrm{K}$, the estimated critical temperature increases by 67 K, to 927 K.

The results from the final three ASIs are presented in Figures 4.9c through 4.9h. Again, the correlation lengths follow a power law decay with increasing temperature. The inverse magnetic susceptibilities have no values that differ by orders of magnitude, as we saw for the two abovementioned systems. The associated standard deviations for $\mathrm{DI}_{0.1,0}$ and $\mathrm{DI}_{0.1,0.1}$, given by the error bars, are large compared to those for the Ising, square, DS and $\mathrm{RDI}^{30}_{0,0}$. The critical parameters for these systems are summarized in Table 4.4. However, they do not provide any new insights, and are therefore not discussed in detail.

The "super"-molecular field constants for the Ising, square and pinwheel ASIs were calculated using Eq. (2.13) and the critical temperatures from Table 4.4. The Ising ASI has $N = 1$ macrospins per area while square and pinwheel has $N = 2$. Using these values, we obtained $\gamma = 1.65 \times 10^{13}$, $\gamma = 1.75 \times 10^{13}$ and $\gamma = 8.64 \times 10^{12}$ for the Ising, square and pinwheel ASIs, respectively. This might be a useful parameter for further work. The values for γ will however not be discussed any further because of the uncertainty related to the calculations of T_C.

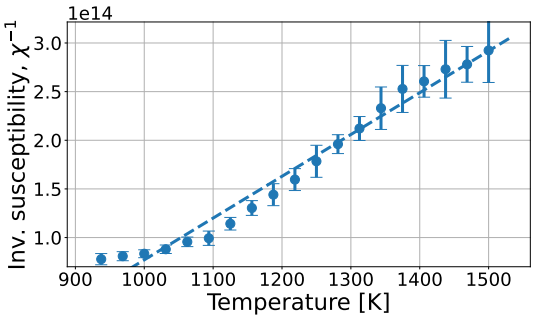

(a) Ising

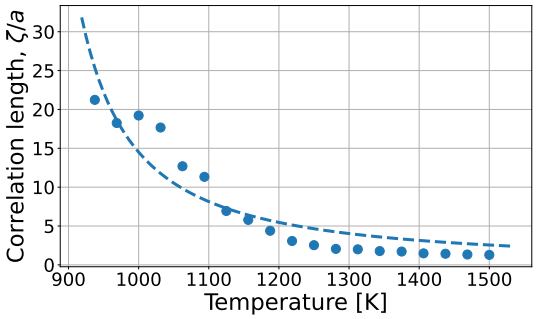

(b) Ising

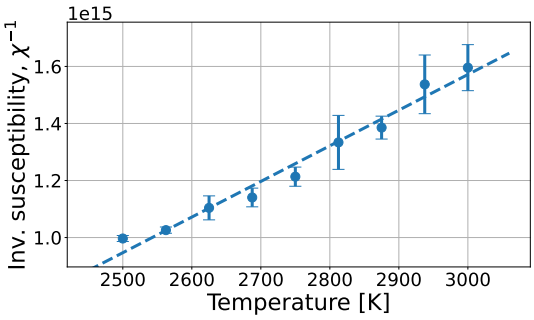

(c) Square

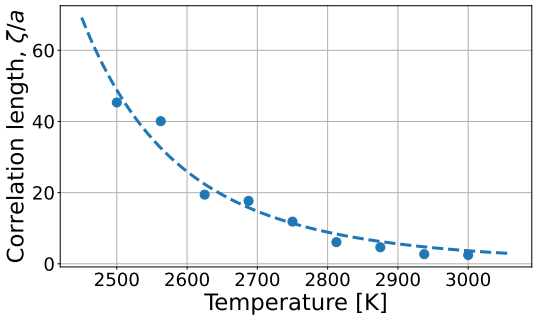

(d) Square

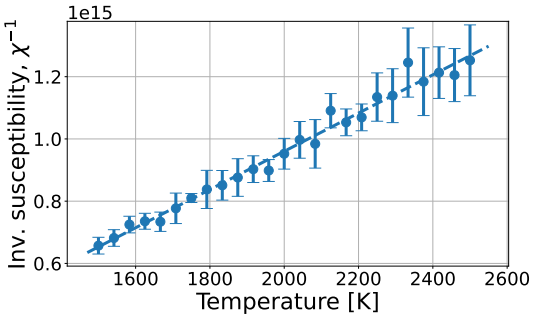

(e) DS

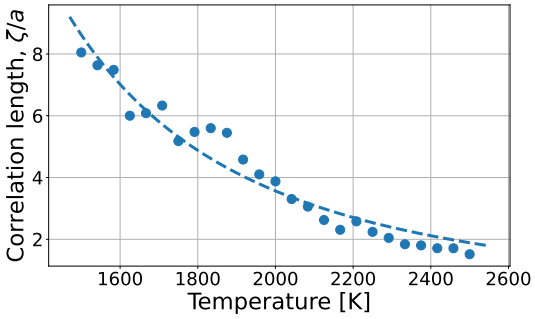

(f) DS

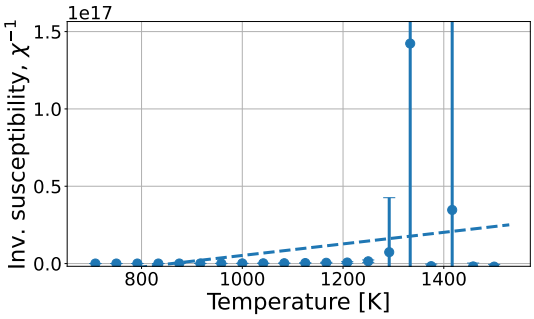

(g) Pinwheel

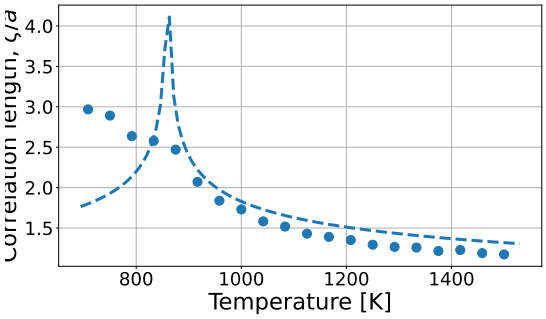

(h) Pinwheel

Figure 4.8: Left: inverse magnetic susceptibilities and curve fit with Curie-Weiss law. Right: Correlation lengths and power law curve fit. The curve fits are the dashed blue lines. The temperature ranges are those identified as the superparamagnetic temperature range for each ASI.

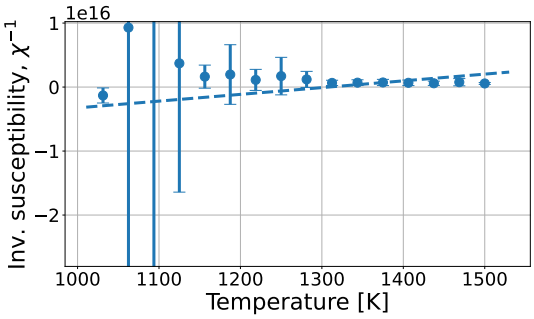

(a) $DI_{0.1,0}$

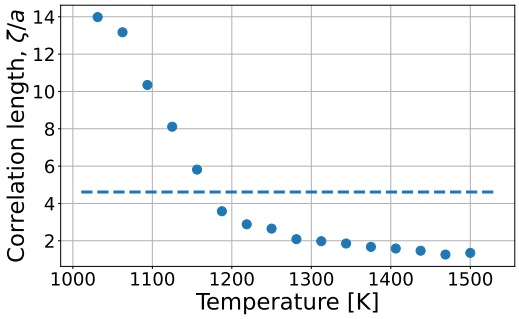

(b) $DI_{0.1,0}$

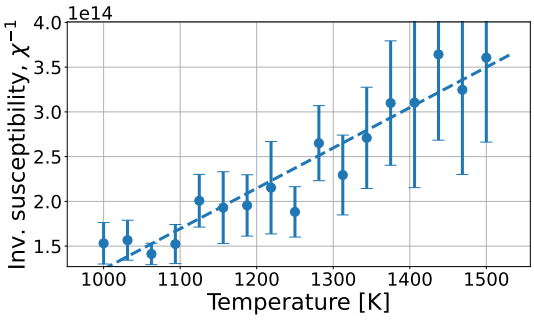

(c) $DI_{0,0.1}$

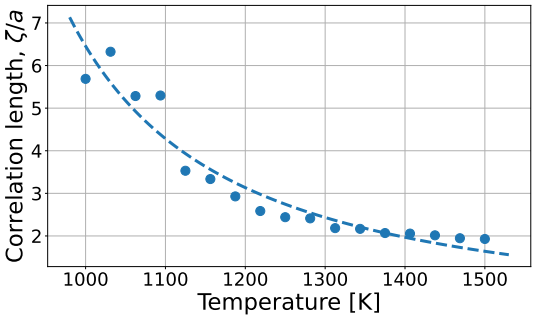

(d) $DI_{0,0.1}$

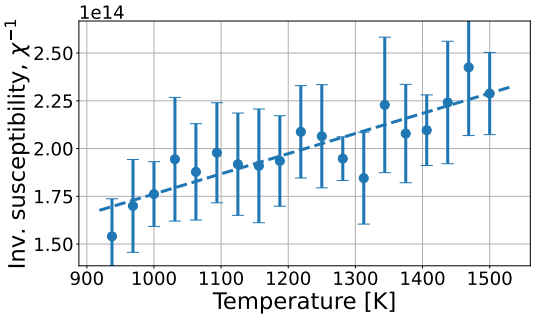

(e) $DI_{0.1,0.1}$

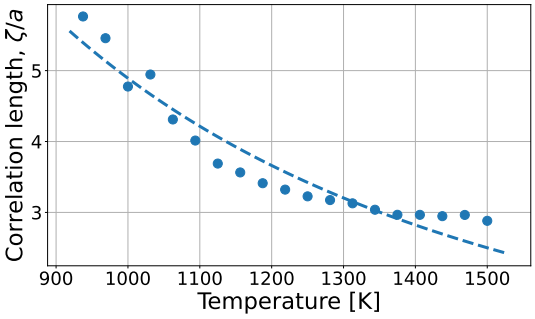

(f) $DI_{0.1,0.1}$

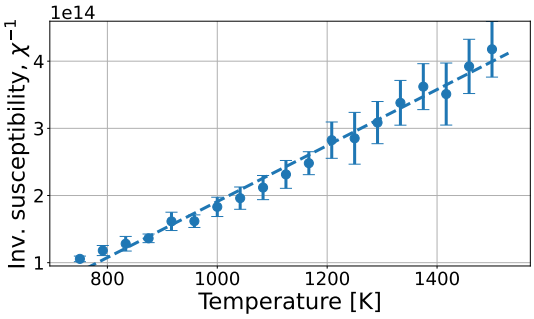

(g) $RDI^{30}_{0,0}$

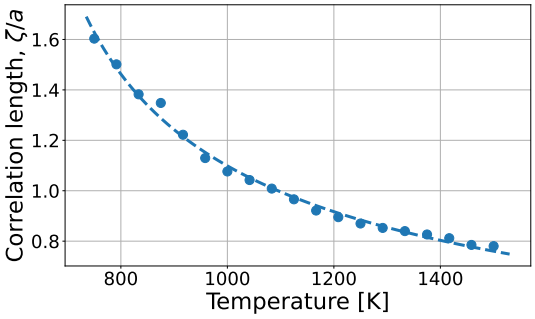

(h) $RDI^{30}_{0,0}$

Figure 4.9: Left: inverse magnetic susceptibilities and curve fit with Curie-Weiss law. Right: Correlation lengths and power law curve fit. The curve fits are the dashed blue lines. The temperature ranges are those identified as the superparamagnetic temperature range for each ASI.

4.2.3 Comparison with literature

Saccone *et al.* used a similar methodology as ours in order to determine the critical temperatures and exponents of experimentally realized ASIs [3]. Comparing their results with those presented in this chapter provide useful insights into both the configuration of the simulator and the methodology as a whole.

The correlation length associated with the experimentally realized Ising ASI after annealing and gradual cooling was $25L$, L being the largest dimension of the nanomagnets (Table I in the source). Expressing this value in terms of the lattice spacing, a, gives a correlation length of $19.7a$. Comparing with the correlation lengths in Figure 4.8b, we see good agreement with the correlation lengths around $\zeta(T = 1000\,\mathrm{K})$. First of all, this indicates that the PCF is able to capture order in the Ising ASI similar to the correlation function used by Saccone *et al.*. Furthermore, the dynamics simulated in flatspin when annealing and gradually cooling the Ising ASI seem to reflect the dynamics of the same procedure done in a laboratory. These are both important results, demonstrating that fundamental building blocks in our analysis agree with experiments and related work.

Saccone *et al.* did not estimate critical parameters for the Ising ASI, but used variations of ASIs referred to as DI and RDI in this work. Expressed in the ASI terminology used in this work, they presented results for $\mathrm{DI}_{0.56,0.79}$ and $\mathrm{RDI}^{180}_{0.56,0.79}$ ASIs (referred to as $\sigma = 100\,\%$, with and without rotation in the source). The critical temperatures obtained were estimated to be 298 K and 11.2 K, respectively, with corresponding critical exponents of $\nu = 1.38$ and $\nu = 1.82$. These results highlight significant differences from what we obtained in this work.

First of all, the temperature range over where the ASIs demonstrated long-range ordering and were thermally active is lower compared to the temperature ranges found in our analyses. This can probably be explained from misconfiguration of simulator parameters (e.g. nanomagnet `volume` or `alpha`), errors caused by the temperature implementation in flatspin, or a combination of the two. It is nevertheless expected, and was discussed in Section 3.2.1.

The correlation lengths obtained by Saccone *et al.* for this level of geometrically disordered ASIs were orders of magnitude larger than those we found. We suspect that this discrepancy can be eliminated, at least partly, by optimizing the flatspin simulator parameters. A higher value of `alpha` would for instance strengthen dipolar interactions and favor long-range ordering of magnetic moments.

4.3 ASIs generated using evolutionary algorithms

The evolutionary algorithms evolved through 20 generations, generating a total of 82 unique ASIs. Examples of four of these ASIs, from generation 0, 3, 9 and 20, are illustrated in Figure 4.10. They demonstrate how the evolutionary algorithms are able to generate ASIs vastly different from the more conventional ASIs in Figure 3.1.

The smallest value of Δ, defined in Eq. (3.10), is plotted for every generation in Figure 4.11. The fitness function tries to evolve towards ASIs such that Δ is minimized. However, we see no clear convergence of Δ towards zero, which would be a sign of successful evolution. The number of generations and unique individuals produced during the evolution process was small, searching through only a small part of possible ASI designs. Results from the previous section do however suggest that the primary challenge with the evolution is the calculation of T_C.

The critical temperatures were calculated using the same method as in Section 4.2.2. Figures 4.12a, 4.12c, 4.12e and 4.12g show results from these analyses for the same four ASIs as were illustrated in Figure 4.10. The plots of inverse magnetic susceptibilities once again demon-

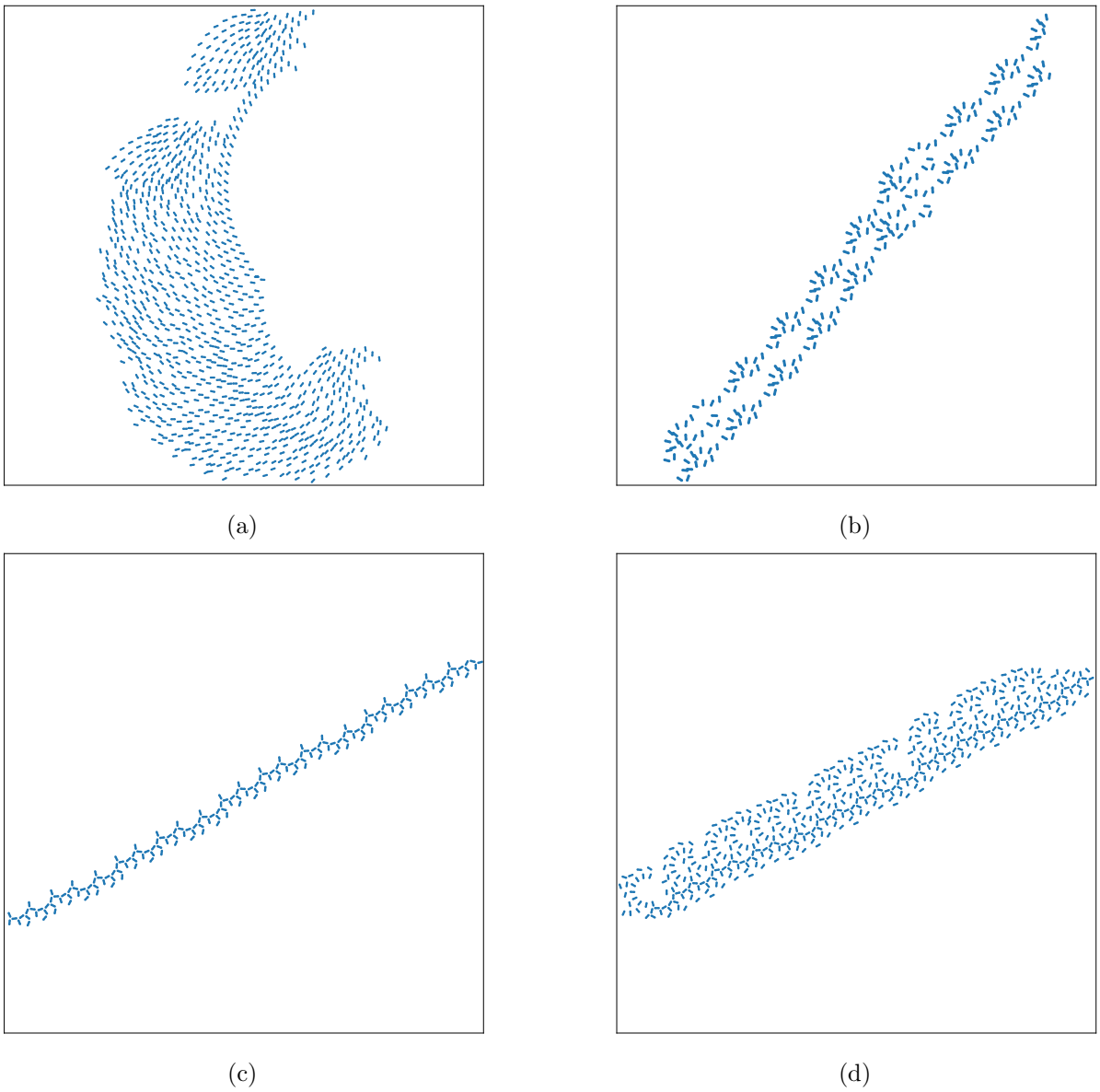

Figure 4.10: Snapshots of the generated ASIs. (a) Generation 0, randomly initialized "genes", (b) generation 3, worst performing, (c) generation 9, best performing ($T_C = 920\,K$), (d) generation 20, final ASI. Every ASI consists of exactly 1000 nanomagnets, but only a subset of them can be seen in the snapshots from the last three generations, allowing us to be able to see individual nanomagnets.

strate the large uncertainties related to these calculations. We must have a more reliable method to calculate T_C if we are to expect the evolutionary algorithms to find ASIs with a tailored critical temperature.

The temperature dependent correlation lengths are plotted in right column of Figure 4.12 (4.12b, 4.12d, 4.12f and 4.12h) for the same ASIs. They all have a trend of decreasing correlation lengths with increasing temperatures. This observation is a validation of the PCF as a generalized correlation function, as it demonstrates its ability to capture magnetic ordering in ASIs across vastly different geometric designs.

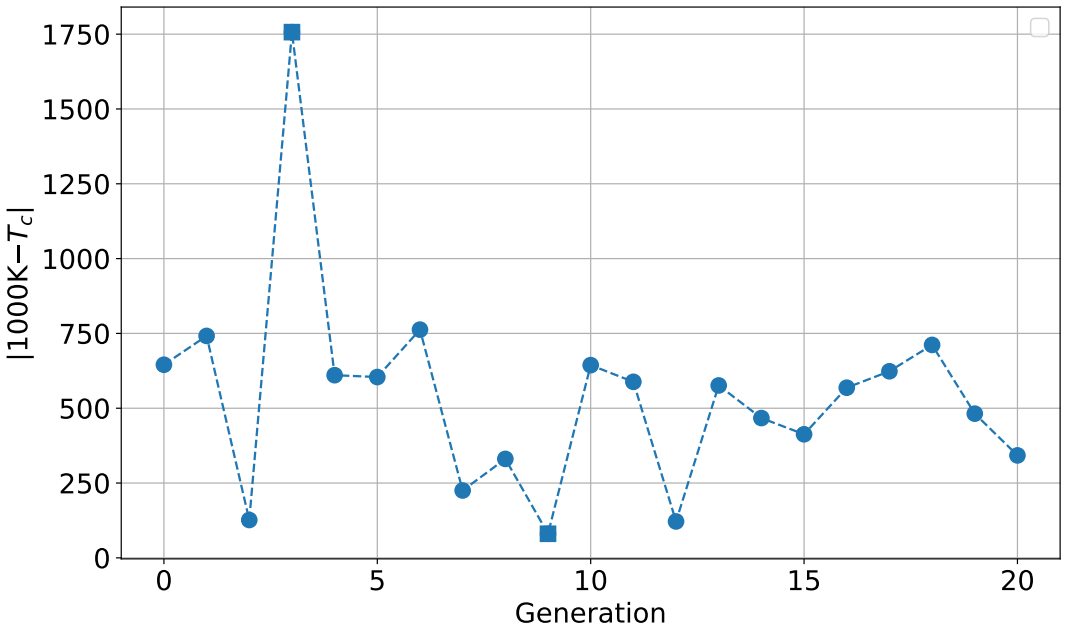

Figure 4.11: Evolution of the "best" ASI per generation, defined as the smallest value of $\Delta = |T_C - 1000\,\mathrm{K}|$. The evolution does not converge towards an ASI with the desired critical temperature during these 20 generations. The squares are the worst (gen 3) and best (gen 9) values of Δ.

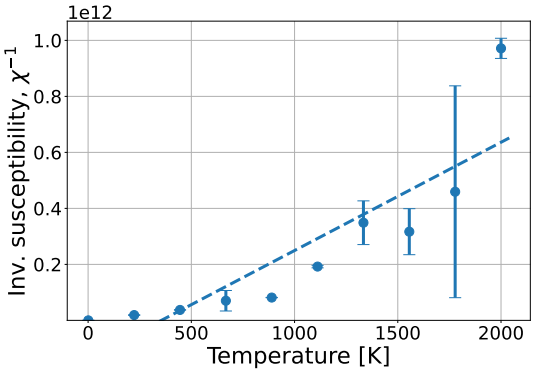

(a) Generation 0

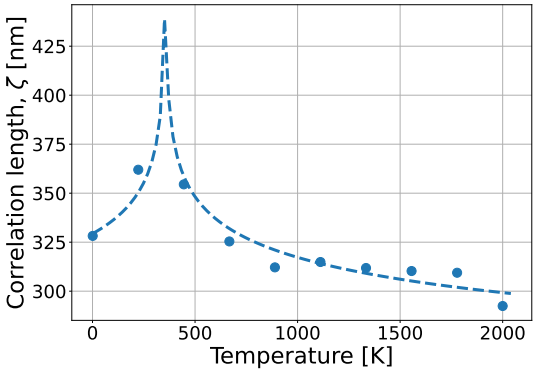

(b) Generation 0

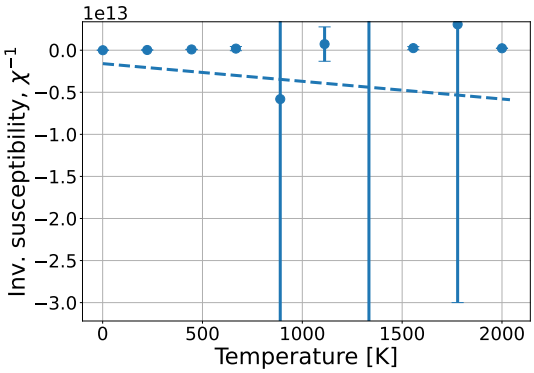

(c) Generation 3

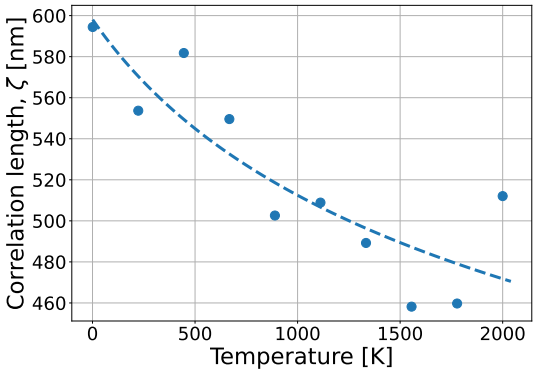

(d) Generation 3

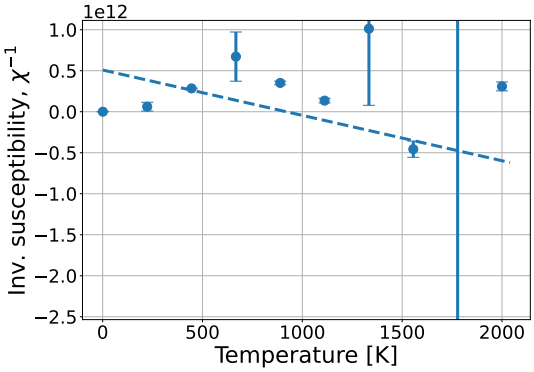

(e) Generation 9

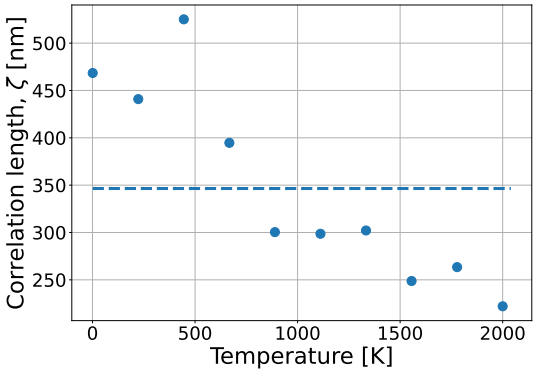

(f) Generation 9

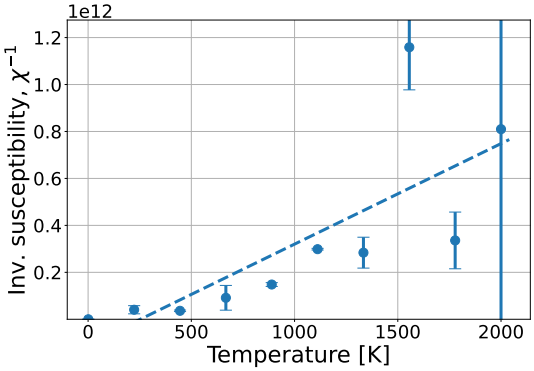

(g) Generation 20

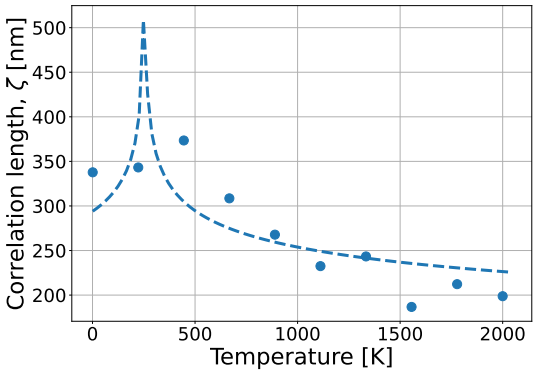

(h) Generation 20

Figure 4.12: Analysis of magnetic ordering, shown for 4 of the generations. Left: inverse magnetic susceptibilities and curve fit with Curie-Weiss law. Right: Correlation lengths and power law curve fit. The curve fits are the dashed blue lines.

Chapter 5

Summary and Conclusion

The results presented in the previous chapter demonstrate that we have successesfully quantified magnetic ordering for several ASI models over a range of different temperatures. We have shown in this thesis that by using a polar correlation function, we are able to capture order in ASIs that are vastly different from the Ising ASI. Using an unconventional technique for generating new and exotic ASI designs, we verified that our methodology is also valid for ASIs where the position of the macrospins are not restricted to lattice points and can have arbitrary element-wise rotations.

Temperature sweeps with no external magnetic fields in flatspin have proven to capture aspects from physically realized ASIs. In particular, we have shown that the correlation lengths computed on various ASIs have a strong temperature dependence and decay exponentially with increasing temperatures. This behavior was theoretically predicted, and does also resemble the results presented by Saccone *et al.* on fabricated ASIs [3].

There are however several elements in our methodology that have proven to be less stable. The inverse magnetic susceptibilities were calculated using the fluctuation-dissipation theorem in Eq. (2.26). Curie-Weiss law was then used to determine a value for the critical temperature of the ASIs. When performing a thermal average over several simulation runs, this method proved to produce large variations in magnetic susceptibility. This is a weakness in our methodology and have given unreliable values for the critical temperature. Steps to reduce this error is suggested in Section 5.1.

We used evolutionary algorithms to evolve new ASIs that were vastly different from the ASIs used in our initial analysis of magnetic ordering. The fitness function we provided did not succeed in guiding the evolution towards the desired critical temperature. Despite few generations and small populations, the most likely reason for failing to evolve towards this critical temperature is the unreliable calculation of magnetic susceptibility.

In Section 3.4.3 we defined a naive condition used to identify the temperature range for the superparamagnetic phase of an ASI. There are probably numerous other methods, for example based on curve fitting or simple machine learning techniques, that are more sophisticated than the naive condition we used.

In the next section we suggest steps that can be taken to increase robustness of the analysis of magnetic ordering. These are either based on the abovementioned findings or were ideas that fell outside of the scope of this thesis.

5.1 Further work

Any extensions of this work should study the theory behind Eq. (2.26), used to calculate the magnetic susceptibilities. Numerically, the variations in these calculations arise from the sum over the correlation function in Eq. (2.26). The effect of summing over a polar correlation function instead of one based on a rectangular grid has not been thoroughly investigated. It is a possibility that the polar discretization of the neighborhood space has introduced errors not accounted for in our analysis.

A useful next step could be to identify any dependence between the abovementioned sum and the particular ASI geometry and discretization of the macrospin neighborhood space. We did not investigate the behavior of $\sum_{ij} C(\mathbf{r}_{ij})$ when setting values for Δr and $\Delta\theta$. This might be a weakness in our methodology.

Factors affecting temperature in the flatspin simulations and their interdependence could also be studied more closely. Our results have shown dynamics that are similar to those seen in laboratory systems. The temperature scale where these dynamics take place are however not the same. Several simulator parameters affect temperature dependence in flatspin, such as those in Eq. (3.2), the standard deviation for the thermal fields in flatspin. A calibration of these parameters and the resulting temperature dependence in flatspin with ASIs realized in a laboratory would provide valuable insights.

In Section 3.3.2 we described the principle behind the PCF and highlighted that the "neighbor magnet" could have any rotation around its position without affecting the parameters r and θ. Introducing a third dimension in the neighborhood space could account for the relative orientation between two neighboring nanomagnets. That would give a more sparsely populated neighborhood space and could give artificially high correlation similar to what we saw with a too fine discretization of the neighborhood space.

It is also worth noting that we do not claim that the PCF is the best correlation function to use when analyzing the magnetic order in ASIs. As long as the correlation function is able to capture order in a system where the nanomagnets are not restricted to fixed lattice points and can have arbitrary element-wise rotations, which the PCF has demonstrated to do, it could be a good candidate to use with the methodology we have described.

5.2 Outlook

We have outlined a route towards exotic ASIs that can be developed with supermagnetic properties as desired by the engineer. Several building blocks required for this route have been established, although the results have shown that the methodology is not yet robust enough to find ASIs with a desired critical temperature in the large space of possible solutions.

ASI is a promising candidate for the realization of devices based on unconventional, material computation. This thesis have taken steps towards the realization of magnetic metamaterials for such computational devices. We believe that a method like the one we have outlined, combining an ASI simulator and evolutionary algorithms with a suitable fitness function, can be used to find ASIs with exotic properties.

Bibliography

[1] *Computation in artificial spin ice*, volume ALIFE 2018: The 2018 Conference on Artificial Life of *ALIFE 2020: The 2020 Conference on Artificial Life*, 07 2018.

[2] J H Jensen, Anders Strømberg, O R Lykkebø, Arthur J Penty, Magnus Sjalander, E Folven, and G Tufte. flatspin: A large-scale artificial spin ice simulator. *arXiv: Computational Physics*, 2020.

[3] Michael Saccone, Andreas Scholl, Sven Velten, Scott Dhuey, Kevin Hofhuis, Clemens Wuth, Yen-Lin Huang, Zuhuang Chen, Rajesh V Chopdekar, and Alan Farhan. Towards artificial ising spin glasses: Thermal ordering in randomized arrays of ising-type nanomagnets. *Physical Review B*, 99:224403, 6 2019.

[4] Carver Mead. How we created neuromorphic engineering, 2020.

[5] Carver Mead. Neuromorphic electronic systems. *Proceedings of the IEEE*, 78, 1990.

[6] Jacob Torrejon, Mathieu Riou, Flavio Abreu Araujo, Sumito Tsunegi, Guru Khalsa, Damien Querlioz, Paolo Bortolotti, Vincent Cros, Kay Yakushiji, Akio Fukushima, Hitoshi Kubota, Shinji Yuasa, Mark D. Stiles, and Julie Grollier. Neuromorphic computing with nanoscale spintronic oscillators. *Nature*, 547, 2017.

[7] Sandra H Skjærvø, Christopher H Marrows, Robert L Stamps, and Laura J Heyderman. Advances in artificial spin ice. *Nature Reviews Physics*, 2:13–28, 2020.

[8] A May, M Saccone, A van den Berg, J Askey, M Hunt, and S Ladak. Magnetic charge propagation upon a 3d artificial spin-ice. *Nature Communications*, 12:3217, 2021.

[9] G. Tufte, S. Nichele, E. Folven, I. Sandvig, and M. Själander. Socrates. `https://www.ntnu.edu/socrates`. Accessed: May 2021.

[10] Arthur Penty and Gunnar Tufte. A representation of artificial spin ice for evolutionary search. *Unpublished*.

[11] John David Jackson. *Classical Electrodynamics*. John Wiley & Sons, Inc, 1 edition, 1962.

[12] T.L. Chow. *Introduction to Electromagnetic Theory: A Modern Perspective*. Jones and Bartlett Publishers, 2006.

[13] J. C. Oersted. Experiments on the effect of a current of electricity on the magnetic needle. *Annals of Philosophy, Or, Magazine of Chemistry, Mineralogy, Mechanics, Natural History, Agriculture, and the Arts*, 1820.

[14] Nicola A. Spaldin. Atomic origins of magnetism, 2012.

[15] David J. Griffiths and Darrell F. Schroeter. *Introduction to Quantum Mechanics*. 2018.

[16] Allan G. Blackman. *Aylward and Findlay's SI chemical data*. John Wiley & Sons, Inc, 7 edition, 2014.

[17] Nicola A. Spaldin. Magnetization and magnetic materials, 2010.

[18] B. D. Cullity and C. D. Graham. Diamagnetism and paramagnetism, 2008.

[19] B. D. Cullity and C. D. Graham. Ferromagnetism, 2008.

[20] Nicola A. Spaldin. Antiferromagnetism, 2012.

[21] M. V. Berry and A. K. Geim. Of flying frogs and levitrons. *European Journal of Physics*, 18, 1997.

[22] Nicola A. Spaldin. Paramagnetism, 2010.

[23] Nicola A. Spaldin. Interactions in ferromagnetic materials, 2010.

[24] Nicola A. Spaldin. Ferromagnetic domains, 2012.

[25] Nicola A. Spaldin. Anisotropy, 2012.

[26] A. Imre, G. Csaba, L. Ji, A. Orlov, G. H. Bernstein, and W. Porod. Majority logic gate for magnetic quantum-dot cellular automata. *Science*, 311(5758):205–208, 2006.

[27] Hua Bai, Xiaofeng Zhou, Yongjian Zhou, Xianzhe Chen, Yunfeng You, Feng Pan, and Cheng Song. Functional antiferromagnets for potential applications on high-density storage and high frequency. *Journal of Applied Physics*, 128, 2020.

[28] R. F. Wang, C. Nisoli, R. S. Freitas, J. Li, W. McConville, B. J. Cooley, M. S. Lund, N. Samarth, C. Leighton, V. H. Crespi, and P. Schiffer. Artificial 'spin ice' in a geometrically frustrated lattice of nanoscale ferromagnetic islands. *Nature*, 439, 2006.

[29] Oles Sendetskyi, Valerio Scagnoli, Naëmi Leo, Luca Anghinolfi, Aurora Alberca, Jan Lüning, Urs Staub, Peter Michael Derlet, and Laura Jane Heyderman. Continuous magnetic phase transition in artificial square ice. *Physical Review B*, 99, 2019.

[30] Einar Digernes, Anders Strømberg, Carlos A. F. Vaz, Armin Kleibert, Jostein K. Grepstad, and Erik Folven. Anisotropy and domain formation in a dipolar magnetic metamaterial. *Applied Physics Letters*, 118:202404, 5 2021.

[31] S. Ladak, D. E. Read, G. K. Perkins, L. F. Cohen, and W. R. Branford. Direct observation of magnetic monopole defects in an artificial spin-ice system. *Nature Physics*, 6, 2010.

[32] Justin S. Woods, Xiaoqian M. Chen, Rajesh V. Chopdekar, Barry Farmer, Claudio Mazzoli, Roland Koch, Anton S. Tremsin, Wen Hu, Andreas Scholl, Steve Kevan, Stuart Wilkins, Wai-Kwong Kwok, Lance E. De Long, Sujoy Roy, and J. Todd Hastings. Switchable x-ray orbital angular momentum from an artificial spin ice. *Phys. Rev. Lett.*, 126:117201, Mar 2021.

[33] Sam D. Slöetjes, Einar Digernes, Christoph Klewe, Padraic Shafer, Q. Li, M. Yang, Z. Q. Qiu, Alpha T. N'Diaye, Elke Arenholz, Erik Folven, and Jostein K. Grepstad. Effects of lattice geometry on the dynamic properties of dipolar-coupled magnetic nanodisk arrays. *Physical Review B*, 99, 2019.

[34] Nicola A. Spaldin. Nanoparticles and thin films, 2012.

[35] Omer Sinwani, James W. Reiner, and Lior Klein. Monitoring superparamagnetic langevin behavior of individual srruo 3 nanostructures. *Physical Review B - Condensed Matter and Materials Physics*, 89, 2014.

[36] Scott A. Mathews, Alexander C. Ehrlich, and Nicholas A. Charipar. Hysteresis branch crossing and the stoner–wohlfarth model. *Scientific Reports*, 10, 2020.

[37] Sethna James. *Statistical Mechanics : Entropy, Order Parameters and Complexity.* Number Vol. 14 in Oxford Master Series in Physics. OUP Oxford, 2006.

[38] Sergey G. Abaimov. *Correlations, Susceptibility, and the Fluctuation–Dissipation Theorem*, pages 289–364. Springer International Publishing, Cham, 2015.

[39] Patrick Henry Winston. Learning by simulating evolution, 1993.

[40] Magnus Själander, Magnus Jahre, Gunnar Tufte, and Nico Reissmann. EPIC: An energy-efficient, high-performance GPGPU computing research infrastructure, 2019.

[41] Pauli Virtanen, Ralf Gommers, Travis E. Oliphant, Matt Haberland, Tyler Reddy, David Cournapeau, Evgeni Burovski, Pearu Peterson, Warren Weckesser, Jonathan Bright, Stéfan J. van der Walt, Matthew Brett, Joshua Wilson, K. Jarrod Millman, Nikolay Mayorov, Andrew R. J. Nelson, Eric Jones, Robert Kern, Eric Larson, C J Carey, İlhan Polat, Yu Feng, Eric W. Moore, Jake VanderPlas, Denis Laxalde, Josef Perktold, Robert Cimrman, Ian Henriksen, E. A. Quintero, Charles R. Harris, Anne M. Archibald, Antônio H. Ribeiro, Fabian Pedregosa, Paul van Mulbregt, and SciPy 1.0 Contributors. SciPy 1.0: Fundamental Algorithms for Scientific Computing in Python. *Nature Methods*, 17:261–272, 2020.

Appendix A

Simulator Commands

flatspin temperature sweep command

```
flatspin-run-sweep -o example_flatspin_sweep -m SquareSpinIceClosed -p 'size
  =(35, 35)' -p timesteps=10000 -p input=0 -p periods=1 -p spp=100 -p
  random_seed=None -p set_temp_method='set_temp' -p neighbor_distance=10 -p
  lattice_spacing=1 -p disorder=0.05 -p alpha=0.01868641975308642 -p
  use_opencl=True -p sw_b=0.41 -p sw_c=1.0 -p sw_beta=2.0 -p sw_gamma=4.0 -p
  hc=0.2 -p msat=860000.0 -p volume=5.8666666666666684e-24 -p 'init=random' -p
   temp_func='custom' -p 'T_anneal=3000' -p 'T_coeff=1.5' -p 'temp_decay_time
  =0.75' -s 'group_id=np.arange(10)' -p max_jobs=10 -s 'T_end=np.linspace
  (1,3000,25)' -s 'temp=[np.hstack((T_anneal*np.exp(np.log(T_end/T_anneal)*pow
  (np.linspace(0,1,round(timesteps*temp_decay_time)),T_coeff)),[T_end]*(
  timesteps-round(timesteps*temp_decay_time))))]' -r dist
```

Listing A.1: Command used to run temperature sweeps in flatspin. Square ASI, 25 temperature steps, 10 runs per temperature.

Evolutionary algorithms command

```
python tile_geno.py -p pop_size=10 -p generation_num=1000 -p inner=correlation
   -p mut_strength=5 -p minimize_fitness=True -p max_jobs=10 -p condition='
  fixed_size' -i pheno_size=1000 -i max_symbol=4 -i max_tiles=4 -p target=1000
   --group-by indv_id -p timesteps=1000 -p input=0 -p H0=0 -p H=0 -p periods=1
   -p spp=100 -p random_seed=None -p init=random -p set_temp_method='set_temp'
   -p neighbor_distance=np.inf -p lattice_spacing=1 -p disorder=0.05 -p alpha
  =68437 -p use_opencl=True -p sw_b=0.41 -p sw_c=1.0 -p sw_beta=2.0 -p
  sw_gamma=4.0 -p hc=0.2 -p msat=860000.0 -p volume=5.8666666666666684e-24 -s
  'group_id=np.arange(2)' -p temp_func='custom' -p 'T_anneal=3000' -p 'T_coeff
  =1.5' -p 'temp_decay_time=0.75' -s 'T_end=np.linspace(1,2000,10)' -s 'temp=[
  np.hstack((T_anneal*np.exp(np.log(T_end/T_anneal)*pow(np.linspace(0,1,round(
  timesteps*temp_decay_time)),T_coeff)),[T_end]*(timesteps-round(timesteps*
  temp_decay_time))))]' -p run=dist -o evoDesign
```

Listing A.2: Command used to run evolutionary algorithms.

flatspin commands for plotting domains

Ising: `flatspin-vectors -w 2 2 -t "-1"`

Square: `flatspin-vectors -w 3 2 -c 1 -t "-1"`

Appendix B

Scripts for Analysis of Magnetic Ordering

All code is written in Python and can be accessed via the project's Github repository: `https://github.com/haavardkatlefjon/ASI_simulation_analysis/`

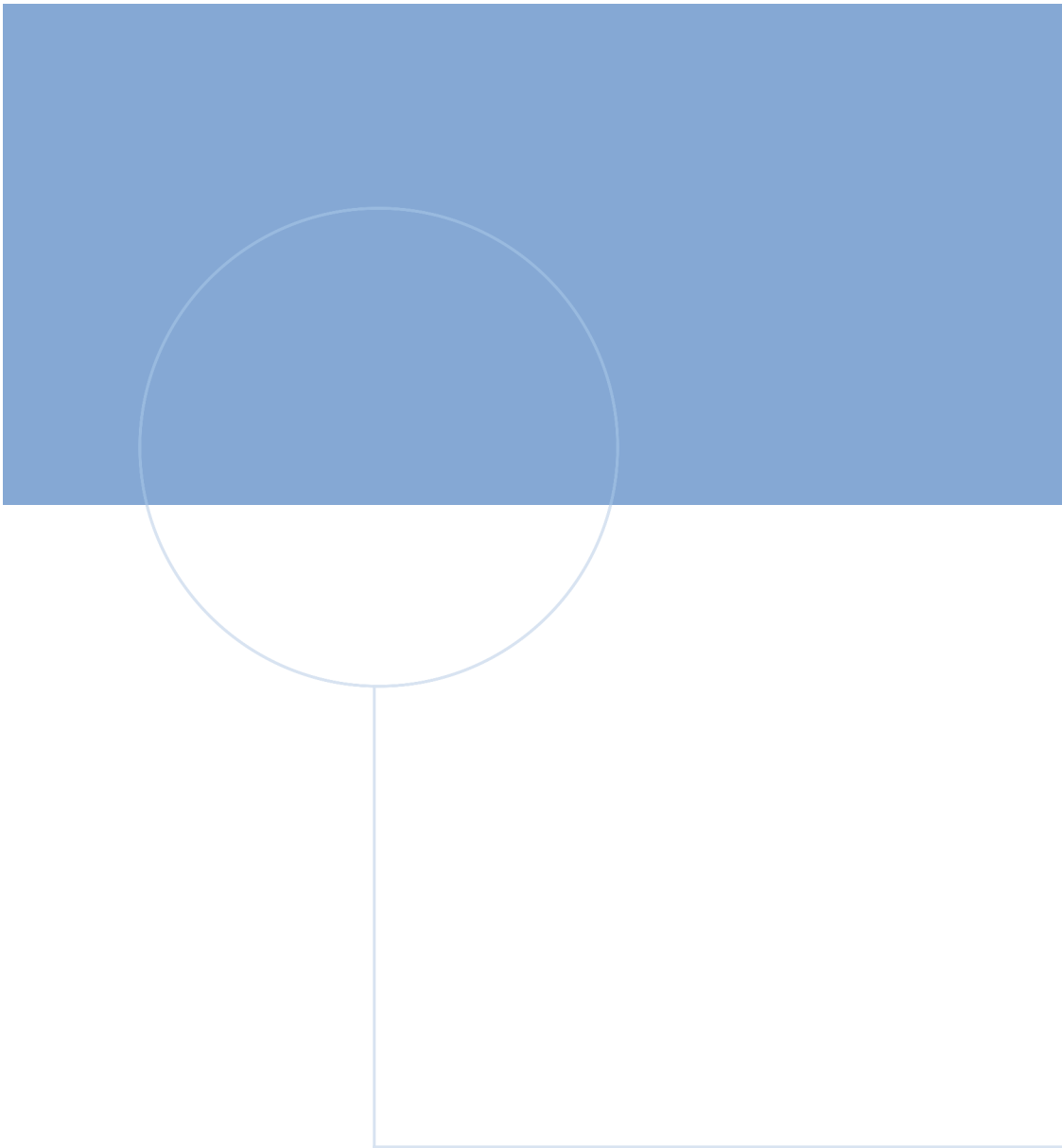

NTNU

Norwegian University of
Science and Technology